9-4-2019

Measuring Collagen Arrangement and Its Relationship with Preterm Birth using Mueller Matrix Polarimetry

Joseph James Chue-Sang
Florida International University, jchue001@fiu.edu

Recommended Citation

Chue-Sang, Joseph James, "Measuring Collagen Arrangement and Its Relationship with Preterm Birth using Mueller Matrix Polarimetry" (2019). *FIU Electronic Theses and Dissertations*. 4364.
https://digitalcommons.fiu.edu/etd/4364

FLORIDA INTERNATIONAL UNIVERSITY

Miami, Florida

MEASURING COLLAGEN ARRANGEMENT AND ITS RELATIONSHIP WITH PRETERM BIRTH USING MUELLER MATRIX POLARIMETRY

A dissertation submitted in partial fulfillment of
the requirements for the degree of
DOCTOR OF PHILOSOPHY
in
BIOMEDICAL ENGINEERING
by
Joseph James Chue-Sang
2019

To: Dean John L. Volakis
College of Engineering

This dissertation, written by Joseph James Chue-Sang, and entitled Measuring Collagen Arrangement and its Relationship with Preterm Birth using Mueller Matrix Polarimetry, having been approved in respect to style and intellectual content, is referred to you for judgment.

We have read this dissertation and recommend that it be approved.

Anuradha Godavarty

Shuliang Jiao

Wei-Chiang Lin

Malek Adjouadi

Jessica Ramella-Roman, Major Professor

Date of Defense: September 4, 2019

The dissertation of Joseph James Chue-Sang is approved.

Dean John L. Volakis
College of
Engineering

Andrés G. Gil
Vice President for Research and Economic
Development and Dean of the University Graduate
School

Florida International University, 2019

DEDICATION

This thesis is dedicated to my parents and siblings. This endeavor would not have been possible without their support and help throughout every step of my way during this process.

ACKNOWLEDGMENTS

I would like to thank my fellow student Mariacarla Gonzalez, who was invaluable in helping me acquire the clinical data in this dissertation, as well as our nurse practitioner, Dr. Nola Holness whose assistance and enthusiasm made this study possible. Last but not least, I would like to thank my advisor, Jessica, for giving me the opportunity, environment, and mentorship necessary to come this far after I first volunteered as a master's student in her laboratory. I did not originally plan on striving towards a PhD, but I do not regret the experience taken to get here in the slightest.

ABSTRACT OF THE DISSERTATION

MEASURING COLLAGEN ARRANGEMENT AND ITS RELATIONSHIP WITH PRETERM BIRTH USING MUELLER MATRIX POLARIMETRY

by

Joseph Chue-Sang

Florida International University, 2019

Miami, Florida

Professor Jessica Ramella-Roman, Major Professor

Preterm birth (PTB) is defined as delivery prior to 37 weeks of gestation. It is the leading cause of infant death worldwide, responsible for infant neurological disorders, long-term cognitive impairment, as well as chronic health issues involving the auditory, visual, digestive, and respiratory systems.

Current diagnosis methodologies of PTB include ultrasound imaging of cervical length and fetal fibronectin assay but have low positive predictive power. Compared to the markers targeted by current diagnosis methodologies, collagen content in the cervix changes more drastically throughout the course of gestation due to its link to changes in load bearing capacity that occur during the phases of pregnancy. Mueller matrix polarimetry is capable of characterizing changes in collagen without making contact with patients and may prove to be an improvement to current diagnosis methodologies. A commercial colposcope was modified to contain Mueller matrix polarimetric capabilities so that patients could be imaged in-vivo during a normal checkup procedure in a much more expedient process compared to work that has been done with optical coherence tomography and second harmonic generation microscopy. A clear difference is seen in collagen orientation between

nonpregnant and pregnant patients. This observation was made by comparing the alignment of collagen between the two populations. A statistically relevant loss of alignment for this small study was seen in the pregnant patients, more so for the patients with past pregnancies. Three of these patients had PTB.

The development of a new imaging modality aimed at assessing early changes in collagen arrangement in the cervix may improve risk determination of PTB and reduce the morbidity of the condition. Earlier prediction of PTB could improve outcomes by allowing longer intervention times to prolong gestation time for the infant in the womb. A more reliable quantitative predictor may also lead to development of more treatment options.

TABLE OF CONTENTS

CHAPTER PAGE

LIST OF TABLES

TABLE PAGE

LIST OF FIGURES

ABBREVIATIONS AND ACRONYMS

PTB	Preterm Birth
MMP	Muellar Matrix Polarimetry/Polarimeter
OCT	Optical Coherence Tomography
PSOCT	Polarization-sensitive Optical Coherence Tomography
SHG	Second Harmonic Generation
PRIM	Preterm Imaging System
DOCP	Degree of Circular Polarization
DOPU	Degree of Polarization Uniformity

CHAPTER 1

INTRODUCTION

1.1 Polarization

Polarization of light is characterized by the orientation of the electric field perpendicular to the direction of propagation of the light wave. Different states of polarized light can be considered as separate E_y and E_x components of the resultant electric field. When all components of the electric field present are in phase the light wave is considered to be linearly polarized and the resultant electric field vector is the orientation of that linear polarization. As the phases of different components of the electric field become out of sync, ellipticity of polarization is created. Typically, ellipticity is created when polarized light traverses through a birefringent structure. Birefringence is a material property describing a change in refractive index depending on the polarization and incidence angle of light passing through the material. This difference in refractive index results in a greater phase delay of certain electric field components compared to others creating elliptic polarization as seen in **Figure 1.1** where polarized light passes through a retarder and cause the E_y and E_x components of the electric field to become out of phase with each other.

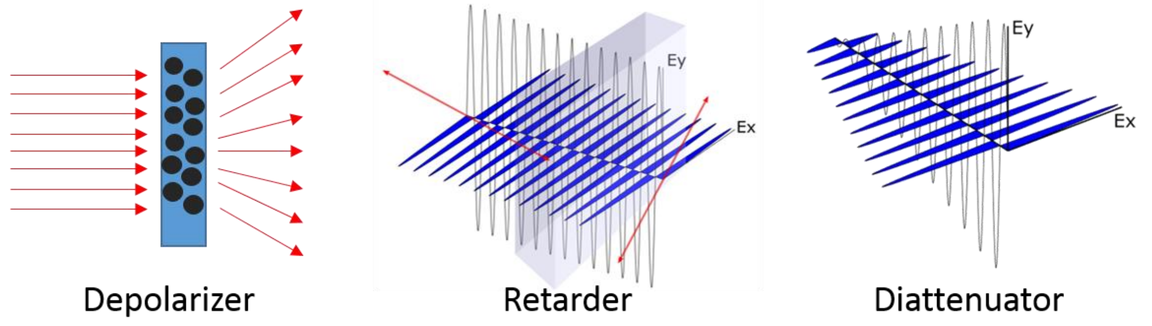

Figure 1.1 Depolarization, retardation, and diattenuation

Having equal $\boldsymbol{E_y}$ and $\boldsymbol{E_x}$ components with a phase difference of 45° between them creates a special state of elliptical polarization called circular polarization. Circular polarization has been used to investigate deeper into biological tissue compared to purely linear polarization due to its ability to generate a greater count of backscattered photons. [1] A graphical representation of depolarization and diattenuation can also be seen in **Figure 1.1**. Depolarization is the randomization of polarization most commonly caused by high scattering materials such as biological tissue. This results in a scrambling of the orientation of the electric field due to the random scattering of light in different directions. Diattenuation is a material's propensity to transmit certain orientation's of linearly polarized light over others. This property is often associated with measuring small molecules where changes are observable unlike in bulk tissue where the effects of diattenuation are negligible compared to depolarization and retardance.

Optical activity can be attributed to a myriad of species characteristics ranging from molecular composition and spatial arrangement to thickness, turbidity, as well as texture. Polarized light is especially sensitive to structural components and materials with strong birefringence; making its use particularly fitted for the investigation of the extracellular matrix of several biological environments, including the skin, the eye's cornea, connective tissue, and many more. The goal of optical equipment in clinical diagnostic tools is becoming increasingly focused on differentiating tissue microstructures and offering noninvasive imaging and in-depth assessment of biological tissues. Such progression is partly due to the advent of polarimetry in optical methods which can elucidate structural morphologies of underlying tissues and enable clear visualization of intermediate superficial tissue layers.

Polarized light imaging has been used in the biomedical field for many years [2]. It has been applied to reveal the border of skin cancer and improve image resolution via removal of multiply scattered light through a degree of polarization (DOP) imaging scheme [3-5] as well as removing multiply scattered light and surface reflection by combining co- and cross-polarized images [6]. Polarization imaging has been combined with spectroscopy in order to image tissue below the surface by discriminating the difference in penetration depth associated with different wavelengths of light. Similar principles have been used to enhance surface capillary contrast [7, 8]. Circularly polarized light has been used to investigate the concentration and size of scattering particles in a medium based off of the backscattered light that is retrieved and modeled in a Poincaré sphere using Stokes vectors [9]. Polarization sensitive Monte Carlo simulations have been developed to model polarized light travel through scattering and birefringent media [9-11].

Birefringent proteins such as collagen fibrils and muscle fibers are often found preferentially aligned in bundles when serving as load-bearing structures [12, 13]. In contrast, in the case of healthy epidermis, collagen is randomly aligned [14, 15, 17]. Significant changes in optical anisotropy and thus birefringence can point to damage or disorder of the normal structure of these tissues [18, 19]. It has been shown that the degree of circular polarization (DoCP) is particularly sensitive to the dominant orientation of birefringent bundles such as collagen [16]. In depth information on a material's effects on polarized light can also be inferred from the calculation of its Mueller matrix [20].

Applications of polarimetry can be observed in various disciplines, such as the chemical industry where unknown substances are identified using their known optical properties. In retinal imaging, the human eye is studied for information regarding its birefringent characteristics. The use of polarization illumination and filtering towards clinical and medical application starts with R. Anderson in 1991 [21] and others [22-24] to enhance surface contrast for dermatologic application.

Groner *et al*. [25] used cross-polarization to highlight superficial vascular contrast in intravital microscopy, and applied this technique in studies of brain perfusion, pancreatic and hepatic microcirculation among others [25-30] . DeHoog *et al*.[31] used Stokes vector polarimetry in a fundus ophthalmoscope. Ghassemi *et al*.[32] studied the rough surface of skin cancer through out of plane polarimetry. De Martino et al. used Mueller Matrix polarimeters to image colon and cervical cancer. [18, 19, 33-39] [34]. Precancerous cancer cells were studied through polarized light sensing[40-46]. Vitkin *et al.*, used Mueller Matrix polarimetry for determining the local structural disorders of the bladder[47] and myocardium[48] as well as other more fundamental studies with Ghosh *et al*.[20, 44, 49-52]

1.2 Polarimetry

Mathematically, the polarization state of light can be written as a Stokes vector ($\boldsymbol{S}$). Stokes vectors contain four elements describing four different characteristics of polarized light – $\boldsymbol{S_0}$ is the magnitude of the intensity of light, $\boldsymbol{S_1}$ is the state of linear of polarization (0/ ±90°), $\boldsymbol{S_2}$ is the state of diagonal polarization (±45°), and $\boldsymbol{S_3}$ is the state of circular polarization (right/left) shown in **Equation 1.1**. Stokes vectors are usually normalized by $\boldsymbol{S_0}$ so that 1.0 in any of the $\boldsymbol{S_1}$-$\boldsymbol{S_3}$ elements describes perfect polarization in that state. Because of this, calculating the magnitude of these three elements should equate to the normalized $\boldsymbol{S_0}$ for the Stokes vector to be feasible.

$$\boldsymbol{S} = \begin{pmatrix} \boldsymbol{S_0} \\ \boldsymbol{S_1} \\ \boldsymbol{S_2} \\ \boldsymbol{S_3} \end{pmatrix} = \begin{pmatrix} \boldsymbol{I_x + I_y} \\ \boldsymbol{I_x - I_y} \\ \boldsymbol{I_{45^\circ} - I_{-45^\circ}} \\ \boldsymbol{I_{rcp} - I_{lcp}} \end{pmatrix} \tag{1.1}$$

I_j represents the intensity of light, and ***rcp*** and ***lcp*** represent right circularly polarized and left circularly polarized, respectively. Because the elements of a Stokes vector cannot be measured directly it is necessary to take intensity measurements of a polarized light source through a polarization analyzer and solve backwards. This is due to different polarization states of light having similar measures of intensity unless an analyzer is used to differentiate between the states. In the case of the calibration method used in this thesis this is done using **Equation 1.2**:

$$\boldsymbol{S = W \cdot I} \tag{1.2}$$

Where ***I*** is the six intensity measurements taken through a polarization analyzer shown in **Equation 1.3**:

$$\boldsymbol{I = \left(I_x\, I_y\, I_{45^\circ}\, I_{-45^\circ}\, I_{rcp}\, I_{lcp}\right)^T} \tag{1.3}$$

and ***W*** is a data reduction matrix defined in **Equation 1.4** after optimization[53]:

$$\boldsymbol{W} = \begin{pmatrix} \boldsymbol{\frac{1}{3}} & \boldsymbol{\frac{1}{3}} & \boldsymbol{\frac{1}{3}} & \boldsymbol{\frac{1}{3}} & \boldsymbol{\frac{1}{3}} & \boldsymbol{\frac{1}{3}} \\ \mathbf{1} & \mathbf{-1} & \mathbf{0} & \mathbf{0} & \mathbf{0} & \mathbf{0} \\ \mathbf{0} & \mathbf{0} & \mathbf{1} & \mathbf{-1} & \mathbf{0} & \mathbf{0} \\ \mathbf{0} & \mathbf{0} & \mathbf{0} & \mathbf{0} & \mathbf{1} & \mathbf{-1} \end{pmatrix} \tag{1.4}$$

Equation 1.4 is an example of an ideal, optimized data reduction matrix as shown by Boulbry *et al.*[53] so that the matrix's condition number is reduced to a minimum value of square root of 3. The condition being a measure of a system's linear independence between columns and rows. The smaller the condition number the greater the system's linear independence and the less loss there is in precision measured by the ratio between the largest and smallest singular value decomposition of the matrix.[54]

Calibrating using this methodology requires that a data reduction matrix $\boldsymbol{W}$ is calculated with a condition close to the minimum so that the stokes vector $\boldsymbol{S}$ in **Equation 1.2** can be solved given that $\boldsymbol{I}$ is the measured experimental intensities. Because the input polarization states are known during calibration, $\boldsymbol{S}$ and $\boldsymbol{I}$ in **Equation 1.2** are accounted for and can be expanded as

$$[\boldsymbol{S_1}\ \boldsymbol{S_2} \ldots \boldsymbol{S_M}] = \boldsymbol{W} \cdot [\boldsymbol{I_1}\ \boldsymbol{I_2} \ldots \boldsymbol{I_M}] \tag{1.5}$$

where $\boldsymbol{S}$ is a 4 x $\boldsymbol{M}$ matrix, $\boldsymbol{M}$ is the number of different input polarization states; and $\boldsymbol{I}$ is a $\boldsymbol{N}$ x $\boldsymbol{M}$ matrix where $\boldsymbol{N}$ is the number of different analyzer configurations. Solving for **Equation 1.2** we get:

$$\boldsymbol{W} = \boldsymbol{S} \cdot \boldsymbol{I^{-1}} \tag{1.6}$$

The issue here lies in calculating the right pseudoinverse of $\boldsymbol{I}$ to solve for $\boldsymbol{W}$. Singular value decomposition (SVD) can be used to calculate the pseudoinverse of $\boldsymbol{I}$ and better optimize towards the ideal data reduction matrix. SVD decomposes the $\boldsymbol{N}$ x $\boldsymbol{M}$ matrix $\boldsymbol{I}$ into the product of three separate matrices – $\boldsymbol{U}$ ($\boldsymbol{N}$ x $\boldsymbol{N}$), $\boldsymbol{V}$ ($\boldsymbol{M}$ x $\boldsymbol{M}$), and $\boldsymbol{D}$ ($\boldsymbol{N}$ x $\boldsymbol{M}$), where $\boldsymbol{U}$ and $\boldsymbol{V}$ are real orthogonal matrices and $\boldsymbol{D}$ is a real diagonal matrix (seen in **Equation 1.7**).

$$\boldsymbol{I} = \boldsymbol{U} \cdot \boldsymbol{D} \cdot \boldsymbol{V^T} \tag{1.7}$$

Further manipulation of the pseudoinverse of $\boldsymbol{I}$ can be carried out to simplify the SVD process by setting small singular nonzero values to zero to help mitigate the noise from the intensity measurements before solving for $\boldsymbol{W}$ as shown by Boulbry *et al.*[53]

In the case of the calibration used for the work in this thesis, the number of different analyzer configurations $\boldsymbol{N}$ was equal to six, and the number of different reference polarization states, ***M*** was 38 split between two different configurations. The two configurations differ in the order that the linear polarizer and quarter wave plate are placed in between the light source and polarization analyzer (see **Figure 1.2**).

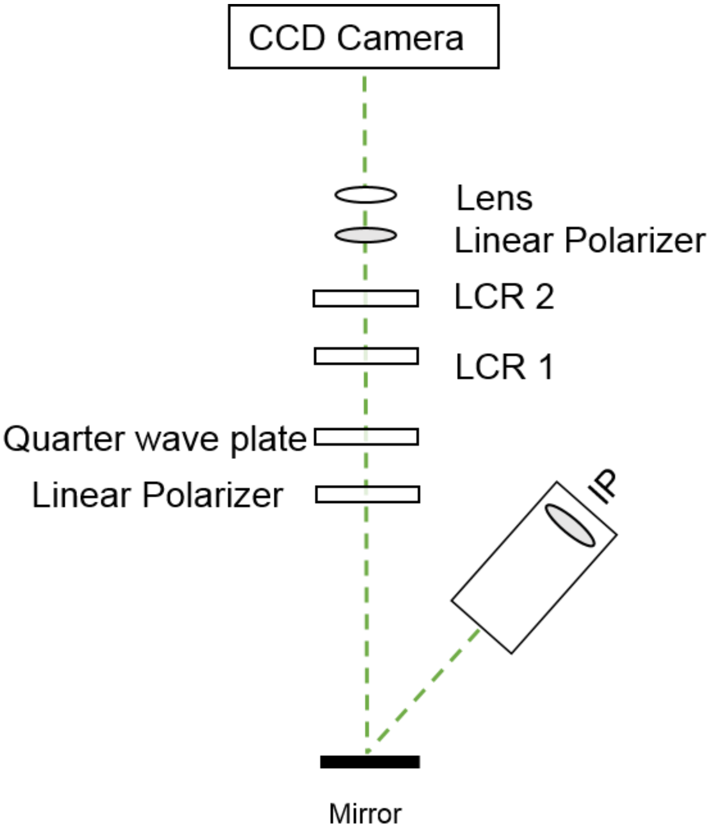

Figure 1.2 Imaging polarimeter calibration setup: The Quarter wave plate and linear polarizer in between liquid crystal retarder (LCR) 1 and the illumination port (IP) change position with each other for the two different calibration configurations.

The linear polarizer and quarter wave plate optical axes are aligned to be both horizontal or vertical (0° or 90°) at the starting reference point for the calibration procedure. The "before" and "after" configurations for the calibration refer to the position of the polarizer being before or after the quarter wave plate. There were 19 reference polarization states used for each configuration which were generated by rotating the linear polarizer using an electronically-controlled rotational mount. The references states created by this process are shown in **Equation 1.8** where θ = 0°-180° with a step size = 10°.

$$\begin{aligned} \boldsymbol{S}^{\boldsymbol{before}}(\boldsymbol{\theta}) &= [\mathbf{1}\ \ \boldsymbol{cos2\theta}\ \ \mathbf{0}\ \ \boldsymbol{sin2\theta}]^{\boldsymbol{T}} \\ \boldsymbol{S}^{\boldsymbol{after}}(\boldsymbol{\theta}) &= [\mathbf{1}\ \ \boldsymbol{cos2\theta}\ \ \boldsymbol{sin2\theta}\ \ \mathbf{0}]^{\boldsymbol{T}} \end{aligned} \tag{1.8}$$

Because both configurations contain the same number of interfaces for the incident light to travel through it is assumed that the loss of light due to reflection is equal, and the maximum intensity should be constant. LCR 1 and 2 are electronically-controlled liquid crystal retarders which are used to reproduce the six analyzer configurations (***N***) for every input reference polarization state (***M***) determined by the polarizer angle and “Before” and “After” setup. An example of raw calibration data is shown in **Figure 1.3** where there are separate intensity curves for each of the six analyzer configurations.

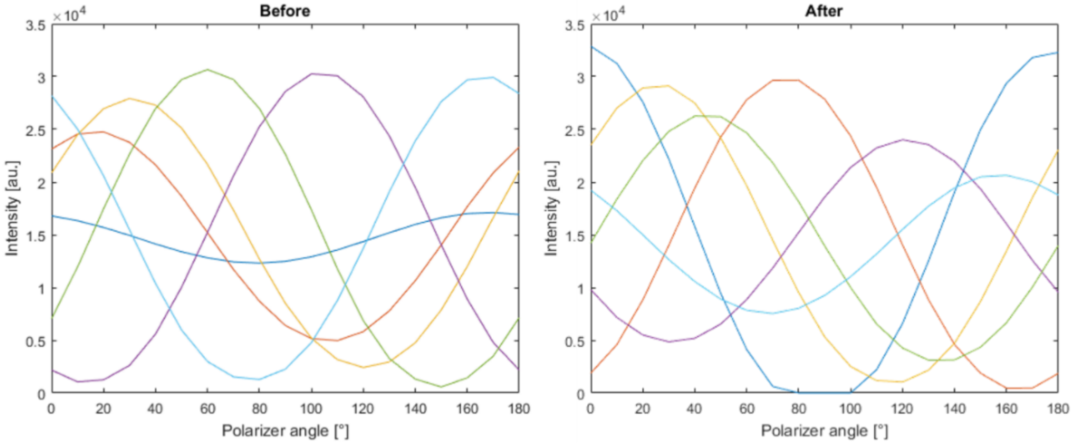

Figure 1.3 Raw calibration data in the “Before” and “After” configurations based on the order of the polarizer relative to the quarter wave plate. The different line colors refer to the six different analyzer states (***N***) created by the two LCRs in front of the camera. As the linear polarizer rotates, the intensity recorded by each analyzer state should return to its starting point since 0°=180°.

After a calibration matrix ***W*** is successfully created with a low condition number, the ***W*** matrix can be used to calculate Stokes vectors from the data collected. An example of these results is shown in **Figure 1.4**, where separate calibrations were performed for different light source wavelengths for the same polarimeter. The four Stokes parameters are plotted between both calibration configurations as the polarizer rotated. Note that in the "After" plots the $\boldsymbol{S_3}$ parameter is constant at 0 as there should be no elliptical/circular polarization state when a linear polarizer is the last polarization element in the calibration setup. Similarly, there can be no horizontal or vertical linear state in the "Before" setup where the polarization is being rotated by a quarter wave plate as the last polarization element in the setup. Because Stokes vectors are usually normalized to the intensity of the light, $\boldsymbol{S_0}$ is constant at 1.

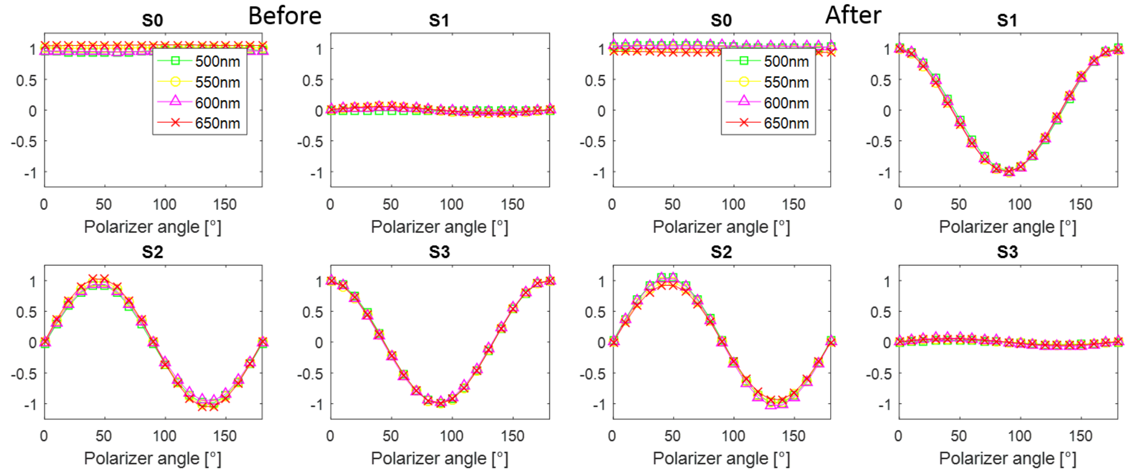

Figure 1.4 Stokes vectors calculated from successful calibration ($\boldsymbol{W}$) using same calibration data. Calibrations for four different LED wavelengths are shown. All wavelength Stokes vectors are below 4% error of each other.[55]

1.3 Mueller matrix

Mueller matrix imaging is the most informative of all polarimetry techniques as the 4 x 4 Mueller Matrix completely characterizes the polarimetric properties of a sample [19 56]. MM decomposition is used to extract constituent polarization properties of an unknown complex system. The decomposition of the Mueller matrix $\boldsymbol{M}$, whose terms are shown in **Equation 1.9** (as proposed by Lu-Chipman [57]) can be experimentally calculated as shown in **Equation 1.10**. Where the first letter indicates the PSG polarization state and the second letter indicates the PSA polarization state of a polarimeter. After decomposition, a Mueller matrix can yield three canonical matrices of **Equation 1.11**, a diattenuator matrix $\boldsymbol{MD}$ includes the effects of linear and circular diattenuation, $\boldsymbol{M_\Delta}$ accounting for the depolarizing effects of the material, a retarder matrix $\boldsymbol{MR}$ for the effects of the material linear birefringence and optical activity. By decomposing $\boldsymbol{M}$ we are able to isolate different light/tissue interaction mechanism, such scattering, absorption, chirality, cumulative retardance and so on. Furthermore, the resulting matrices can be analyzed to yield quantitative medium properties that have a demonstrated [7, 34, 37] useful diagnostic power and will be used in this study. These parameters are: depolarization, linear retardance (birefringence), optical Rotation, slow axis orientation θ (the direction of polarization with the larger optical index) and diattenuation D. Depolarization is caused by multiple scattering events and is prominent in biological tissue[58]. It results in the randomization of the polarization of light that travels through scattering media.

$$\boldsymbol{M} = \begin{bmatrix} \boldsymbol{m_{11}} & \boldsymbol{m_{12}} & \boldsymbol{m_{13}} & \boldsymbol{m_{14}} \\ \boldsymbol{m_{21}} & \boldsymbol{m_{22}} & \boldsymbol{m_{23}} & \boldsymbol{m_{24}} \\ \boldsymbol{m_{31}} & \boldsymbol{m_{23}} & \boldsymbol{m_{33}} & \boldsymbol{m_{34}} \\ \boldsymbol{m_{41}} & \boldsymbol{m_{24}} & \boldsymbol{m_{43}} & \boldsymbol{m_{44}} \end{bmatrix} \tag{1.9}$$

$$\boldsymbol{M} = \frac{\boldsymbol{1}}{\boldsymbol{2}} \begin{bmatrix} HH + HV + VH + VV & HH + HV - VH - VV & PH + PV - MP - MM & RH + RV - LH - LV \\ HH - HV + VH - VV & HH - HV - VH + VV & PH - PV - MH - MV & RH - RV - LH + LV \\ HP - HM + VP - VM & HP - HM - VP + VM & PP - PM - MP + MM & RP - RM - LP + LM \\ VR + HR - LL - RL & VL + HR - HL - VR & ML + PR - PL - MR & RR + LL - LR - RL \end{bmatrix} \tag{1.10}$$

$$\boldsymbol{M = M_\Delta M_R M_D} \tag{1.11}$$

These parameters can be used to identify tissue changes due to injury or disease [59]. **Equation 1.11** is one of six possible decompositions and the most commonly used in biomedical applications. In the case of Lu-Chipman’s decomposition which is used in this dissertation, $\mathbf{M}_{\mathbf{D}}$ is calculated directly from the experimental Mueller matrix **M**. The other two matrices are solved for afterwards. Despite these many applications and some interesting computational work polarized light imaging has had limited commercial success in the Biomedical field due to a number of factors: light polarization is quickly lost in heavy-scattering media such as biological tissue, analyzing and extracting meaning from heterogeneous tissue is complicated, and there are still limited amounts of data describing polarization properties of tissues. [2, 20, 60, 61]

1.4 Preterm Birth

Preterm birth (PTB) is the leading cause of infant death worldwide, having an incidence of over 11% in the United States and 15% [62] in developing countries. PTB rates are greater at 18.1% in Miami-Dade County, FL, possibly due to inadequate prenatal care and nutrition [63]. PTB is defined as labor prior to 37 weeks of gestation and is responsible for infant neurological disorders [64], long-term cognitive impairment [65], as well as chronic health issues involving the auditory, visual, digestive, and respiratory systems [66]. In expectant mothers, causes for PTB can include infection, inflammation [67], vascular disease, [68] short intervals between pregnancies [69], multiple gestations [70] and genetic factors [71].

The early identification of at-risk pregnancies allows the employment of tocolytics, antenatal corticosteroids, and hormones such as terbutaline**,** betamethasone and progesterone and the performance of cervical cerclage to delay the start of labor contractions and increase the development time in utero. Cerclage can also be performed to mechanically seal the cervix to delay birth. Current diagnosis of PTB is based on tactile and visual inspection of the cervix to determine dilation, ultrasound of cervical thickness [72], and fetal fibronectin (fFN) immunoassay [73], which all have low positive predictive power. The lack of positive predictive power of the current PTB diagnosis modalities means that it is difficult for physicians to decide on whether any intervention should be performed. A more reliable diagnosis method could allow physicians to work on delaying birth earlier to give the fetus more development time. This issue also increases the difficulty of developing and testing new treatments. Thus, the development of diagnostic modalities that can identify risk of PTB holds great potential in reducing the morbidity of the condition.

Preterm labor has many causes but irrespective of its etiology[68] mechanical cervical failure or change in the cervix extracellular matrix is a common endpoint. Recent work has highlighted the role of collagen in PTB [74-76]. The collagen of the cervix provides the structure necessary to hold the baby within the uterus during gestation. Numerous researchers have studied the collagen of the cervix to determine how this structure maintains its integrity during pregnancy. [77-84] Aspden *et al*. found the structure of collagen is oriented in three unique areas surrounding the cervical canal, the anisotropic alignment of the collagen differing within each area. The cervical fibrils are aligned both around and along the canal for increased strength. [12, 85-88] Fibrillar collagen is the major structural protein in the cervix that determines its load bearing capabilities. With progression of pregnancy, the cervix undergoes changes in the collagen structure and corresponding mechanical strength. Structural defects in the cervix result in preterm birth as exemplified in women with cervical insufficiency. Several human and animal studies have suggested that atypical changes in the extracellular matrix of the cervix precede SPB [74-76, 88, 89]. Thus, the development of diagnostic modalities that could identify premature abnormal cervical remodeling holds great potential as a tool for early and accurate assessment of cervical disease.

Optical measurement of cervical remodeling throughout pregnancy via changes in collagen arrangement and density may be able to predict the occurrence of pre-term labor. Polarization sensitive techniques can be used to target the fibrous ultrastructure of the cervix. Studies have shown the ability of Mueller matrix polarimetry to identify colorectal and cervical cancer. [19, 38, 90]

We developed a **PReterm IMaging System (PRIM)** based on a standard colposcope, with high sensitivity to cervical ultrastructure using Mueller matrix polarimetry. This methodology was used to measure differences in collagen structure between nonpregnant and pregnant cervixes in order to determine if changes in collagen could be linked to progression of pregnancy and preterm birth. It was first tested using excised porcine cervixes and validated using images produced by optical coherence tomography (OCT) before being used to image nonpregnant and pregnant human cervixes *in-vivo*. [91]

1.5 Cervix Physiology

A cartoon representation of the cervix is shown in **Figure 1.5**. The cervix is an extension of the lower part of the uterus comprising a portion of the female reproductive system. It is cylinder shaped, approximately 3 to 4 centimeters long and 2.5 centimeters in diameter, with a central canal through its entirety. The cervical canal serves as the entrance canal, via the vagina, for sperm for reproduction and the exit canal, via the uterus, for childbirth. The two ends of the canal are termed the internal and external orifice (os) depending on whether they are present in the uterus or vagina, respectively. The portion of the cervix visible from the vagina canal can be further divided into two regions due to their cellular differences - the ectocervix and endocervix. The ectocervix is the stiff structure protruding from the anterior vaginal wall and is comprised of a stratified squamous epithelium, containing several cell layers of differing morphological characteristics as well as collagen and smooth muscle. [92] The cell layers of the epithelium are subdivided into classes relating to their maturation and include one layer of basal cells, two layers of parabasal cells and numerous layers of both intermediate cells and superficial cells. The thickness of the epithelial layer is between 200 and 500 microns. [93, 94] The endocervix is made of a single layer of mucus secreting columnar (glandular) epithelial cells lining the cervical canal. Where the ectocervix and endocervix meet at the center of the external OS is called the transformation zone and is the location where glandular epithelium is replaced by squamous epithelial cells.[95] Any changes in cervical structure, morphology, and color may be indicative of disease[96-99]. Non-invasive imaging techniques may provide important diagnostic information with less discomfort for the patient. Recent work in cervical imaging has shown great promise[96, 100-104].

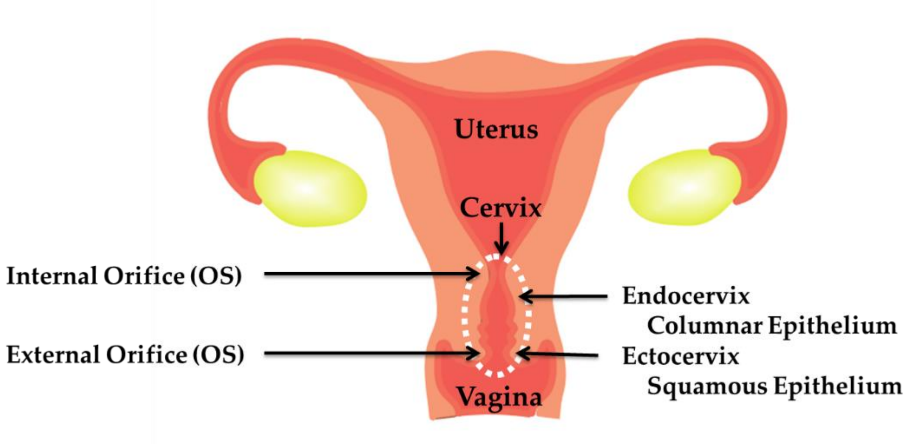

Figure 1.5 The cervix

For example, De Martino *et al*. used Mueller Matrix Polarimetry to differentiate between cancerous and non-cancerous cervical samples by measuring depolarization and retardation of excised human cervixes.[105, 106] Richards-Kortum *et al*. used confocal microscopy to identify differences between normal, pre-cancerous and cancerous cervical tissues. [107-110] Ramanujam *et al*. engineered means for cervical imaging for low-resource settings [111], as did Levitz *et al*.[112] Recently, Hendon *et al*. [102, 113-115] used optical coherence tomography to identify collagen orientation of human ex-vivo cervixes to investigate differences in collagen angular distribution between pregnant and non-pregnant cervixes. Finally, Second Harmonic Generation imagery has been used to observe changing collagen architecture in the cervix to provide detailed images of fibrous collagen structure. [79, 101, 116-120]

1.6 Collagen in the cervix

Collagen is one of the most abundant types of molecules in vertebrate species. It is an important part in creating the scaffolding which gives tissues and organs their structure as well as establishing the necessary environment required for cell-extracellular matrix (ECM) interactions which are important for signaling various cellular functions. There are 29 different types of collagen known currently. These different types of collagen are assembled into supramolecular structures to provide different functions within the ECM. [121] Collagen type numbers are designated based on chronological order of discovery; Type I being the most abundant form of collagen by far at 90%. Type I collagen makes up striated collagen fibrils and is the main component in providing mechanical strength and structure for most tissues in the body.

The deciding factor in differing between collagen types is the difference in genes that code for a collagen polypeptide, otherwise known as alpha chains. There are currently 45 distinct alpha chains known. All collagen molecules are trimers consisting of three alpha chains wound around each other. Most known collagen types are made of three of the same alpha chain. Depending on how many collagen molecules are wound together the structure can go from being a procollagen (one trimer with the alpha chains loosely wound together) to a collagen fibril where multiple collagen molecules are wound together and finally a collagen fiber consisting of multiple fibrils wound together. All types of collagen must contain at least one triple helix domain and noncollagenous domain. The triple helix is a peptide structure unique to collagen trimers which creates the stiffness necessary loading bearing structures in the body. The noncollagenous domain is much more loosely wound than the triple helix and are sites of binding and activity for noncollagenous molecules such as endothelial cells. There can be any number of suprastructures that make up the ECM and ultimately the tissue structures; its function is ultimately determined by the composition of different collagen types as well as the noncollagenous macromolecules present. Because minor molecules which only make up a small fraction of a polymer can give it unique functionality, collagen suprastructures are often responsible for giving different tissues their specific structure and functional properties according to Birk-Bruckner.[121]

Collagens I-III are majorly responsible for the creation of the collagen fibers that will studied in this thesis using polarimetry. Collagen that is destined to form fibrils is first synthesized as procollagens which are trimers containing three alpha chains wound together. The amino acid composition of the alpha chains depends on the type of collagen.

Procollagen contains two distinct propeptide domains known as a C-terminal and a N-terminal. Propeptides are precursors to proteins that are inactive in function. Post-translational modification is required to activate the protein. This is most commonly achieved through removal of a section of amino acids, or addition of molecules in order to achieve proper protein folding and activation of its function. Propeptides are important for proteins that can be potentially harmful if left freely active. Collagen is such a protein in that freely synthesized and activated fibrillar collagen will create scar tissue and would be dangerous if it was not properly targeted in areas such as wounds or when building the scaffolding ECM for tissue. The C-terminal is completely noncollagenous, while the N-terminal contains several noncollagenous domains around a short collagenous domain. C-propeptides are post-processed by BMP-1 and tolloid proteinases as well as furin while N-propeptides are post-processed using ADAMTS 2,3, and 14 and BMP-1 enzymes. In the case of the fibrillar collagens I and II, there is a central triple helical domain surrounded by short noncollagenous terminals named telopeptides. The triple helix provides the mechanical strength needed for the collagen fibril and the telopeptides create the functionality needed to adhere to other collagen or molecules. After the propeptides that make up the collagen I-III molecules have been processed they self-assemble and fold to become striated fibrils with a 67 nm periodicity.[121] Collagen molecules are arranged longitudinally in a staggered pattern so that the end of each molecule does not overlap with the adjacent molecules. It is this structure that creates the striated appearance of fibrillar collagen and provides resistance against torsion and tension. Collagens V/XI act as regulators of collagen fibril organization that result in tissue-specific differences in collagen fibril and are present in minor amounts wherever collagen I-III assembles.

Like most proteins, collagen molecules undergo a similar production cycle. Fibril collagen is synthesized, processed, assembled from three polypeptides [alpha chains], and folded into its functional state within the endoplasmic reticulum. The finished product is then transported in vesicles from the Golgi through the cell before being excreted from the cell membrane. This process allows for intracellular regulation of what collagens and noncollagenous molecules are assembled together and packaged for secretion to create different kinds of ECM for tissues of varying functions. Examples of noncollangenous molecules that can be secreted to affect ECM function include procollagen processing enzymes, fibril-binding molecules, adhesive glycoproteins, and fibronectin.[121] ECM assembly begins in compartments made within the developing matrix. Protofibrils are assembled from procollagen inside the cytoplasm of fibroblasts but near to the cell membrane before they are secreted by into the aforementioned compartments. From these compartments the protofibrils are deposited into much larger nearby spaces in the developing matrix where the fibrils combine to create collagen fibers. This assembly is promoted and stabilized by interaction with regulatory molecules such as the small leucine-rich proteoglycan (SLRPs) and fibril-associated collagens with interrupted triple helices (FACITs) that are similarly secreted into this space by other compartments in the developing matrix. As more and more fibers aggregate adjacently in the space, the fiber bundle increases in diameter from ~20 nm in protofibrils to upwards of 500 nm in mature tissues in the case of fibrous tissue like tendon.[122] The promotion of what forms of collagenous tissue is assembled in the compartments is regulated by which enzymes and other molecules are secreted and stored inside the compartments to interact with the collagen during the maturation process and is tissue specific. Paramount to this collagen fiber maturation process in the activity of lysyl oxidase which creates covalent crosslinking between fibrils, increasing the collagen length, diameter, stability, and ultimately the mechanical strength of the connective tissue it is developing. Depending on what molecules are present during ECM formation, connective tissues formed from collagen can be categorized into different categories such as cartilage and tendon.

An ECM lies under the epithelium of the cervix, separated by the thin basal lamina layer of collagen type IV fibers [93], and consists mainly of collagen, approximately 10-15% smooth muscle cells [123-125] and a mixture of biomolecules. The ECM of the cervix is mainly comprised of two types of collagen - approximately 70 % is collagen type I and 30 % collagen type III. [126, 127] In addition, the ground substance of the ECM contains glycoprotiens elastin and fibronectin, glycosaminoglycan (GAGS) decorin, buglycan, chondroitin sulfate, keratan sulfate, and dermatan sulfate, hyaluronic acid and water. [123, 125, 128-130]

The role of the cervix is to serve as a barrier in order to maintain the fetus *in utero* until gestation is complete and to preserve the fragile environment of the uterus required for proper development. The abundance of collagen in the cervix and its organization provides the necessary mechanical strength to keep the fetus inside this environment.[86] As the pregnancy moves towards labor, the cervix loses stiffness allowing the external os to expand so that the baby can exit the uterus. Numerous researchers have studied the collagen of the uterus to determine how this structure maintains its integrity during pregnancy. [77-84] Aspden *et al*. found that the anisotropic alignment of collagen has a preferred orientation in three regions surrounding the cervical canal. The most inner and outer regions of the ectocervix contain collagen fibrils aligned in the direction of the cervical canal, while the region between these two has collagen oriented circumferentially around the cervical canal. These alignments are shown as in **Figure 1.2**. [12, 85-87] A MRI study has shown that the circumferential alignment of collagen is preserved throughout the entire cervix between the external and internal OS.[131] This is important since full field imaging polarimetry does not have depth resolution but instead gives a summary of polarization information from its probing photons. The alignment of collagen being preserved throughout the cervix helps this depth limitation.

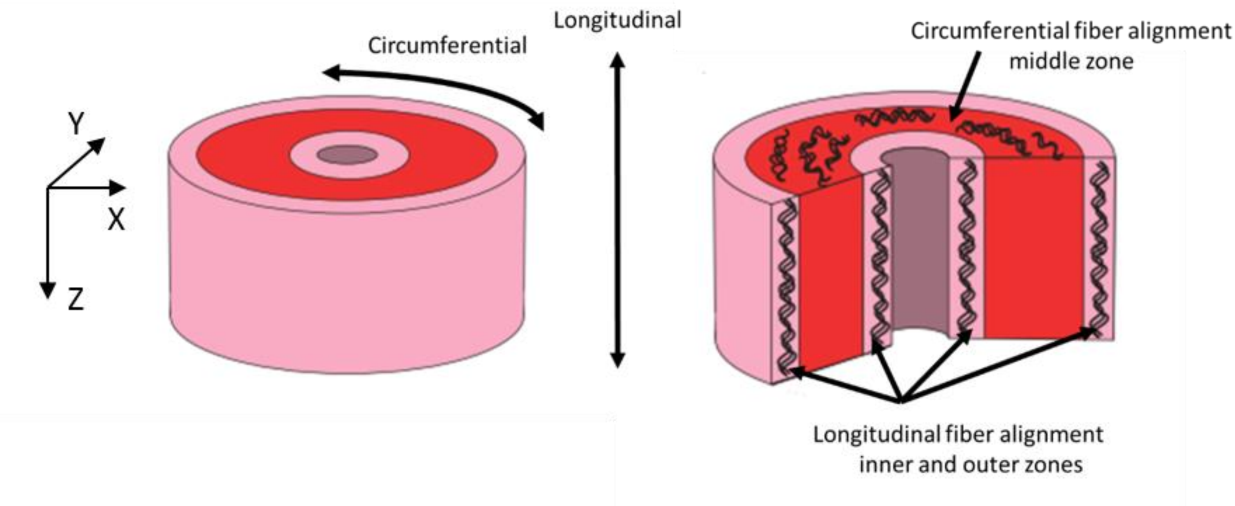

Figure 1.6 Alignment of collagen fibers in human cervix in three anisotropic zones

The cervix undergoes dramatic changes between the initial pregnant state and delivery of a baby. In both women and animal models the phases of cervical remodeling can be described as cervical softening, ripening, dilation and postpartum repair. Research by Myers and others [12, 89, 132-135] has shown how these phases relate strongly to changes in the cervical collagen and fibrous tissue directionality and dispersion. In early pregnancy collagen remains in an organized fibrous structure, as gestational age advances, the woman’s cervix becomes softer [135, 136] which translates into structural reorganization of collagen in the cervix [137-139]. In pre-term-labor these phases do not change but their duration is shortened [140, 141] so that the cascades of events leading to parturition is dramatically accelerated. Many of these changes are not yet well understood, nor the physiological factors which cause these changes.

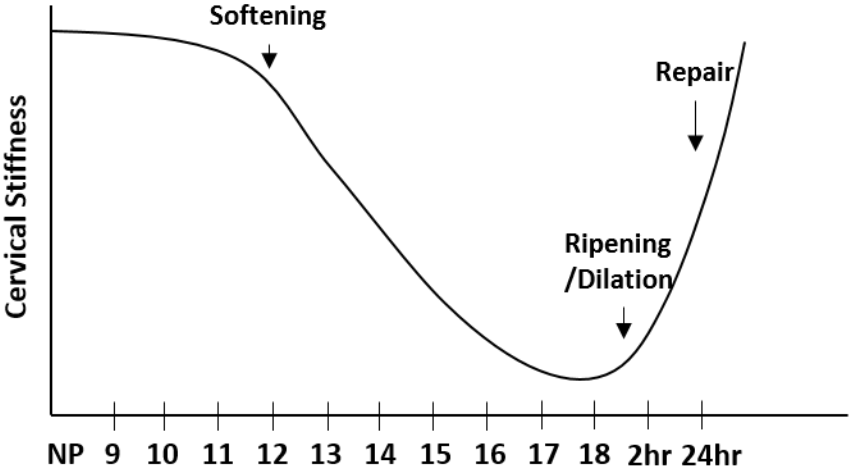

Figure 1.7 Cervical stiffness throughout phases of pregnancy.[142] Cervical collagen remodeling causes the cervix to lose its structural integrity when nonpregnant in preparation for dilation during child birth. Time scale depicted is for mice, however a similar model can be applied for most mammals.

The physiological properties of the cervix are altered by a cascade of micro-environmental events in each of these phases. Cervical softening begins within one month of the initiation of pregnancy and the cervix undergoes increased vascularity and edema. [81] Softening is a longer, steadier phase than the others, progressing through the 33rd week of pregnancy. The collagen of the stroma becomes less organized and the cervix becomes pliable and begins shortening. Timmons *et al*. states this as a maintenance of tissue competence occurring while increasing tissue compliance. [143] The ripening phase begins, after softening, and as House *et al*. points out, this predominantly deals with the cervix changing roles from a load-bearing function to a birthing canal. [124] By the end of cervical ripening, when dilation begins, some researchers have found there is a 30-70% decrease of collagen [128, 130, 136] since the onset of pregnancy, although Myers *et al*. believe there is a decrease in crosslinking but not in actual collagen content. This is purported to be due to increased solubility in weak acids rather than change in collagen content. [12] In addition, there is also a decrease in specific glycosaminoglycans (chondroitin sulfate and dermatan sulfate) [144], and an increase in the hydrophilic glycosaminoglycan [145], hyaluronic acid [139] and thus, an increase in water (5 – 10%).[124 146 147] Researchers have also found there occurs a shift from insoluble to soluble collagen [128, 148] with as much as 90% soluble collagen by the third trimester[124]. Dilation follows ripening and involves an influx of leukocytes, [124] similar to an inflammatory response, which may serve to cause an increase in the matrix metalloproteinase, collagenase. [81 149 150] Collagenase causes the breakdown of collagen cross links and allows the cervix to weaken [12, 79, 151] and open thereby radically changing shape by shortening and effacing in preparation for delivery of the baby.

Polarization imaging has been used to study collagen as a method of identifying different diseases such as skin cancer[3], colon cancer[18], and atherosclerosis[152] by measuring changes or disruptions in the healthy arrangement of collagen in these different tissues. It may also prove useful in measuring the changes in collagen during pregnancy.

Current diagnostic of PTB is based on tactile and visual inspection of the cervix to determine dilation, ultrasound of cervical thickness [72], and fetal fibronectin (fFN) immunoassay [73]. The strengths of ultrasound and fFN immunoassay lie in their high negative predicting power for PTB within the next 7 days after measurement. However, their positive prediction power for PTB is low. [73 89]. The role of collagen has been emphasized in PTB [74-76]. The strength of the cross-linked cervical collagen fiber network is integral to maintaining gestation. Forceful contractions in a rigid, closed cervix will not result in delivery, while a weakly structured cervix is susceptible to preterm birth without contractions[88]. Optical measurement of cervical remodeling throughout pregnancy via changes in collagen arrangement and density may be able to predict the occurrence of preterm labor. Polarization sensitive techniques can be used to target the fibrous ultrastructure of the cervix due to collagen's strong birefringence. Birefringence describes a sample's change in refractive index depending on the incident angle of polarized light with the sample's anisotropic axis. Polarized imaging modalities can detect change in a birefringent material by measuring its response to incident polarized light. Several experiments were designed to test the feasibility of detecting the orientation of collagen fibers of human cervixes in vivo.

1.7 Experimental Timeline

The experiments within this thesis can be broken down into three major milestones. Initially, it was important to establish that full field imaging Mueller matrix polarimetry can successfully capture changes in birefringent tissue. This was done by first designing and constructing a benchtop Mueller matrix polarimeter combined with a polarization sensitive optical coherence tomographer (PS-OCT). The instrument was tested by measuring the density of collagen in baboon heart valve leaflets via use of collagenase activity and was corroborated using the PS-OCT. This work was published in the Journal of Biomedical Optics (JBO) in 2016. [153]

After deciding to pursue a more specialized parameter that can be measured from collagen using Mueller matrices, it was decided to focus on collagen [retarder axis] orientation. This was in response to pursuing research in the domain of PTB where full field imaging of the cervix had not been done. Until then, images had been tiled together from second harmonic generation (SHG) microscopy[79, 87, 142] and OCT[102, 115]. A Mueller matrix polarimeter integrated with a colposcope would allow images of the entire cervix to be taken from outside the vagina and without making contact with the patient. To accomplish this, the previously used benchtop Mueller matrix polarimeter was used to examine the collagen structure in *ex-vivo* porcine nonpregnant cervixes in comparison to OCT images acquired via a methodology used by Gan *et al*. [102] The comparison was done to show the efficacy of MMP in this setting and was published in JBO in 2017.[91]

After showcasing the benchtop system's ability to capture the collagen organization of collagen in excised cervixes in was decided to move on to imaging *in-vivo* human cervixes. To accomplish this a colposcope was heavily modified to incorporate a Mueller matrix polarimeter of the same design as the benchtop system. The Mueller matrix colposcope was used to image nonpregnant volunteers at the Nicole Wertheim College of Nursing under the supervision of Dr. Nola Holness before the eventual imaging of pregnant women at Jackson Memorial Hospital. The preliminary comparison between nonpregnant and pregnant patients was published in JBO in 2018.[154]

A study on a smaller scale than the previous three was conducted to look at the effect of light source wavelength on the quality of results acquired using MMP. To accomplish this the benchtop MMP system was reconstructed with the light source being replaced with a white light lamp that could be filtered to produce 4 different wavelengths with 10 nm bandwidths. It was observed that the lower wavelengths produced less noisy orientation images. This was reported in a proceeding for SPIE Photonics West BIOS 2018.[55]

The emphasis of this dissertation lies in translating Mueller matrix polarimetry technology to a clinical setting in a manner that allows patients to be imaged non-invasively and without contact, and so that the healthcare provider is minimally affecting during their routine work. These design inputs were paramount in creating the colposcope used in Chapter 4. A Preliminary analysis was also done for this this small study.

CHAPTER 2

[1]Use of combined polarization-sensitive optical coherence tomography and Mueller matrix imaging for the polarimetric characterization of excised biological tissue.

Joseph Chue-Sang,(1) Yuqiang Bai,[1] Susan Stoff[1], David Straton[1], Sharan Ramaswamy[1], Jessica C. Ramella-Roman[1,2a]

[1]Department of Biomedical Engineering, Florida International University, Miami, FL, USA, 33178
[2]Herbert Wertheim College of Medicine, Florida International University, Miami, FL, USA 33178
(a) Author to whom correspondence should be addressed. Electronic mail: jramella@fiu.edu

Abstract:

Mueller matrix polarimetry and Polarization Sensitive Optical Coherence Tomography (PS-OCT) are two emerging techniques utilized in the assessment of tissue anisotropy. While PS-OCT can provide cross-sectional images of local tissue birefringence through its polarimetric sensitivity, Mueller Matrix polarimetry can be used to measure bulk polarimetric properties such as depolarization, diattenuation, and retardance. To this day true quantification of PS-OCT data can be elusive, partly due to the reliance on inverse models for the characterization of tissue birefringence and the influence of instrumentation noise. Similarly for Mueller Matrix polarimetry calculation of retardance or depolarization may be influenced by tissue heterogeneities that could be monitored with PS-OCT. Here we propose a novel instrument that combines Mueller Matrix polarimetry and Polarization Sensitive Optical Coherence Tomography. Through the co-registration of the two systems we aim at achieving a better understanding of both modalities.

---

[1] This chapter was accepted for publication by the Journal of Biomedical Optics Special Issue on Polarized Light (July 2016). 10.1117/1.JBO.21.7.071109

Keywords: Mueller matrix, PS-OCT, polarization, birefringence, collagen.

2.1 Introduction

Polarized light imaging has been used in the biomedical field for many years [2]. It has been applied to reveal the border of skin cancer and improve image resolution via removal of multiply scattered light through a degree of polarization (DOP) imaging scheme [3-5] as well as removing multiply scattered light and surface reflection by combining co- and cross-polarized images [6]. Polarization imaging has been combined with spectroscopy in order to image tissue below the surface by discriminating the difference in penetration depth associated with different wavelengths of light. Similar principles have been used to enhance surface capillary contrast [7, 8]. Circularly polarized light has been used to investigate the concentration and size of scattering particles in a medium based off of the backscattered light that is retrieved and modeled in a Poincaré sphere using Stokes vectors [9]. Polarization sensitive Monte Carlo simulations have been developed to model polarized light travel through scattering and birefringent media [9-11].

Birefringent proteins such as collagen fibrils and muscle fibers are often found preferentially aligned in bundles when serving as load-bearing structures [12, 13].

In contrast, in the case of healthy epidermis, collagen is randomly aligned [14, 15, 17]. Significant changes in optical anisotropy and thus birefringence can point to damage or disorder of the normal structure of these tissues [18, 19]. We have shown that the degree of circular polarization (DoCP) is particularly sensitive to the dominant orientation of birefringent bundles such as collagen [16]. In depth information on a material's effects on polarized light can also be inferred from the calculation of its Mueller matrix [20]. Mueller matrix imaging is possibly the most useful of all polarimetry techniques as the 4 x 4 Mueller

Matrix completely characterizes the polarimetric properties of a sample [19] including its cellular size distribution and refractive index [56]. MM decomposition is used to extract constituent polarization properties of an unknown complex system. The decomposition of the Mueller matrix M, whose terms are shown in **Equation 2.1** (as proposed by Lu-Chipman [57]) yields three canonical matrices of **Equation 2.2**, a diattenuator matrix MΔ includes the effects of linear and circular diattenuation, M_Δ accounting for the depolarizing effects of the material, a retarder matrix MR for the effects of the material linear birefringence and optical activity, and a depolarizer matrix MD includes the effects of linear and circular diattenuation. By decomposing M we are able to isolate different light/tissue interaction mechanism, such scattering, absorption, chirality, cumulative retardance and so on. Furthermore, the resulting matrices can be analyzed to yield quantitative medium properties that have a demonstrated [7, 34, 37] useful diagnostic power and will be used in this study. These parameters are: depolarization, linear retardance (birefringence), optical Rotation, slow axis orientation θ (the direction of polarization with the larger optical index) and diattenuation D. Depolarization is caused by multiple scattering events and is prominent in biological tissue[58]. It results in the randomization of the polarization of light that travels through scattering media.

$$M = \begin{bmatrix} m_{11} & m_{12} & m_{13} & m_{14} \\ m_{21} & m_{22} & m_{23} & m_{24} \\ m_{31} & m_{32} & m_{33} & m_{34} \\ m_{41} & m_{42} & m_{43} & m_{44} \end{bmatrix} \tag{2.1}$$

$$M = M_\Delta M_R M_D \tag{2.2}$$

These parameters can be used to identify tissue changes due to injury or disease [59]. **Equation 2.2** is one of six possible decompositions and the most commonly used in biomedical application. Despite these many applications and some interesting computational work polarized light imaging has had limited commercial success in the Biomedical field due to a number of factors: light polarization is quickly lost in heavy-scattering media such as biological tissue, analyzing and extracting meaning from heterogeneous tissue is complicated, and there is still limited amounts of data describing polarization properties of tissues [2, 20, 60, 61]

Optical coherence tomography (OCT) is a noncontact, noninvasive interferometric technique allowing cross-sectional imaging of tissues at the micron level. OCT has been explored in many applications over the past decade, including ophthalmology, cardiovascular, oncology, and dermatology [155-158] as well as embryogenesis, angiogenesis, tissue engineering [159-163]. Polarization sensitive OCT (PS–OCT) [164-167], as a functional extension of OCT, uses the information encoded in the polarization state of the recorded interference fringe intensity to provide additional contrast. In birefringent materials a phase delay between the two orthogonally polarized wave components is caused by the difference of the refractive indices n_o and n_e of the ordinary and extraordinary wave $\Delta n = n_o - n_e$, resulting in different phase velocities of both wave components [168-170]. In general, the delay causes an elliptical polarization state, a measure of the internal birefringence. The ellipticity of the signal is recorded by the two detectors measuring the horizontally and vertically polarized interference signal. The double-pass phase retardance between the two components can be calculated through the amplitude ratio of both detected signals

$$\phi(x,z) = arctan\frac{|a_2(x,z)|}{|a_1(x,z)|} \tag{2.3}$$

a_1 and a_2 denote the intensity of the horizontal and vertical components of the interference signal respectively. ϕ denotes the wrapped phase retardance and could be exploited to generate a retardance image. PS–OCT provides high resolution of spatial information pertaining to imaged tissues otherwise not discernible using existing diagnostic optical methods. Nevertheless PS-OCT results are highly susceptible to low signal to noise ratio [171-174], and values of birefringence obtained with these systems still rely on ad-hoc models [168, 175].

To study the effect of polarized light transfer in heterogeneous biological media we have developed a system integrating Mueller Matrix Polarimetry (MMP) and PS-OCT. The multimodal combination of MMP with PS-OCT will provide comprehensive information about optical properties of tissue. Correlation of bulk properties obtained from MMP and detailed structure information from PS-OCT will enhance our interpretation and analysis of imaging data from the targeted tissues, and will refine our understanding of polarized light propagation through turbid media.

2.2 Materials and Methods

A schematic of the combined PS-OCT and MMP system is shown in **Figure 2.1**. The experimental setup of the high resolution PS-OCT system is based on a free-space Michelson interferometer and is detailed with the red light path. The system has a resolution of 3.3 µm in air and 2.5 µm in tissue. The laser light source is a broadband Superluminescent Diode (Bayspec, San Jose, CA) with 840-nm central wavelength and 50-nm full width half maximum (FWHM). Light from the source is split into the sample arm and the reference arm by a 50/50 cube beam splitter. Along the sample path the light then passes through a quarter-wavelength plate (QWP) @ 45° and a telecentric scan lens (LSM03-BB, Thorlabs, Newton, NJ) focuses signal light onto the sample and collects the backscattered light. A galvanometer-mounted mirror on the sample arm enables transverse beam scanning on the sample. After the beam splitter the beam passes through a QWP @ 22.5 and a scan lens and is then reflected by a reference mirror. A variable attenuator is placed in front of the reference mirror to attenuate light returning from the reference arm. The attenuator is adjusted to optimize the modulation depth of the raw OCT interference term.

Subsequently, both the probe and the reference beams enter a polarization beam splitter (PBS), which spatially separates the horizontal and vertical polarization components of these two beams. The spectrum of these two components is simultaneously detected by two custom-made spectrometers consisting of a collimating lens with a focal length of 75 mm (Edmund Optics, Barrington, NJ), a 1800 lines/mm volume holography transmission grating (Wasatch Photonics Logan, UT), an assembly of triple lenses with an effective focal length of 150 mm, and a line array CCD camera (spL4096-140k, Basler, Highland, IL). The acquired interference spectrum data is transferred to a computer system using a National Instrument image acquisition card (PCI 1433). Data processing algorithm, control and display software are developed using LabView (National Instruments, Austin, TX). During lateral scanning of the illumination beam on the sample, multiple A-scans are acquired and processed. At the end of the scanning cycle, an intensity-based cross-sectional image (B-scan) of the sample is reconstructed and displayed on the computer screen.

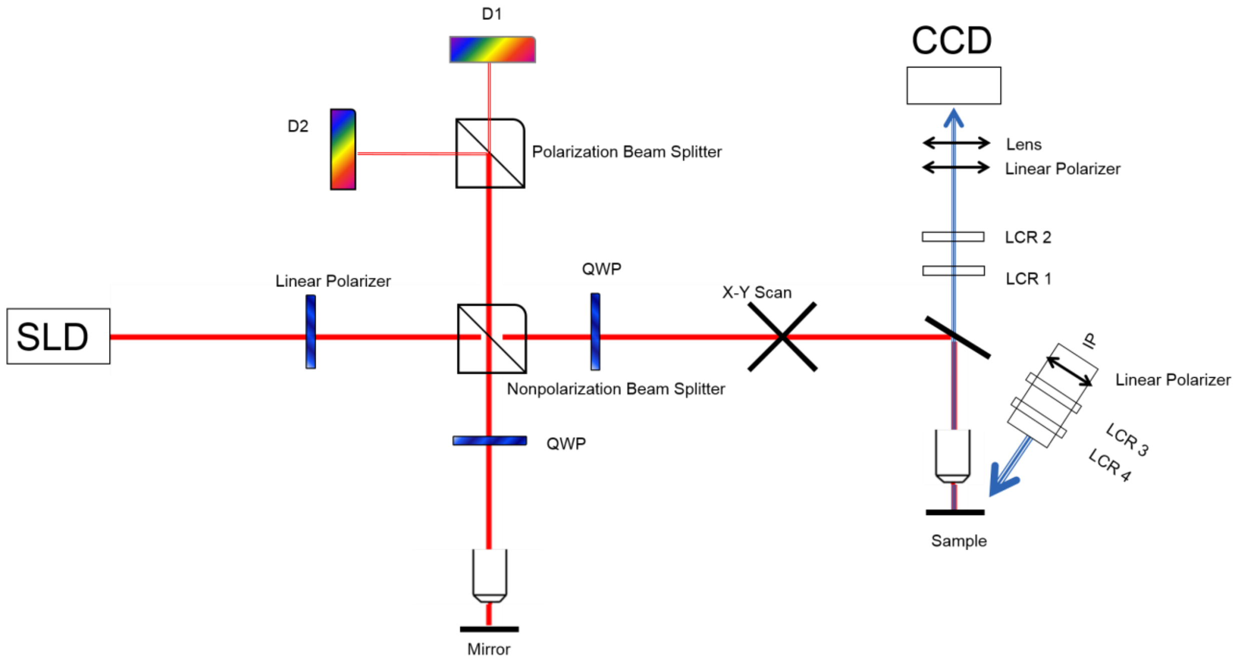

Figure 3.1 Combined PS-OCT and Mueller Matrix polarimeter schematic

In **Figure 2.1**, the Mueller Matrix system is detailed with the blue light path. A CCD camera (Evolve Delta, Photometrics, Tucson, AZ) with a 0.60X microscope lens (HRD060-NIK, Diagnostic Instruments) attached, was secured above the sample objective to allow focusing on the height adjustable stage. A linear polarizer (Prinz, Northbrook, IL) and two liquid crystal retarders (LCR) (Meadowlark Optics, Frederick, CO) between the lens and sample objective form the PSA of the polarimeter. Employing the same sample objective for the two imaging systems ensures they are imaging the same region of interest. IP in **Figure 2.1** indicates the light source arm for the MMP. A 530 nm LED (M530L, Thorlabs, Newton, NJ) was oriented to illuminate the sample at an incident angle of 45° and collimated with a 30 mm diameter tube and a 25 mm diameter plano-convex lens (Newport, Irvine, CA). The incident light was linearly polarized (LPVIS100, Thorlabs, Newton, NJ) and then retarded using two LCRs before reaching the sample to create four different polarization states. These four different states were then used to calculate the Mueller matrix of the sample. Matlab (Mathworks, Natick, MA) was used to control the devices and analyze the data acquired by the MMP which had a field of view of 3 mm and a resolution of 5.8 µm using the shared sample objective.

2.2.1 Calibration of PS-OCT-Mueller Matrix and co-registration of images

The calibration of the MMP system follows a standard methodology utilized by our group in several applications [176, 177]. An Ag-coated mirror was tilted beneath the sample objective on the stage and adjusted so that the maximum intensity of light was reflected from the source into the analyzer above the objective. For calibration, the IP was adjusted to contain a motor-controlled linear polarizer and a QWP in series after the LED light source. Six images were taken with the polarimeter using six different retardances programmed into the LCRs as the linear polarizer's optic axis was rotated between 0° and 180° with a step size of 10°. Four images with different retardances are the minimum required to generate a 4-element Stokes vector, however, six images were used in order to increase the accuracy of the calibration matrix generated after the imaging process. The order of the linear polarizer and the QWP was then reversed before repeating the same imaging process. The imaging process and the algorithm for calibrating the MMP using the images taken are discussed in detail in a previous publication [53].

In order to validate the Mueller matrix function of the MMP, air was used as the standard. The same imaging process used previously for the MMP calibration was again used before constructing a Mueller matrix. Similar to constructing Stokes vectors, four Stokes vectors are the minimum amount of data required to construct a 16-element Mueller matrix. Having more information as the imaging process used did allow for more accurate results. The

Mueller matrix of air calculated from images taken from the MMP system are shown below. The error is 0.40% from the ideal Mueller matrix of air.

$$\begin{bmatrix} 0.997 & -0.000 & 0.001 & -0.005 \\ 0.004 & 1.000 & 0.010 & -0.001 \\ -0.001 & 0.004 & 0.991 & 0.002 \\ 0.001 & -0.002 & 0.009 & 0.999 \end{bmatrix}$$

To evaluate our PS-OCT system and to test its effect on the polarization of light returning to the spectrometers, we placed a QWP in front of a mirror onto a rotational stage. The optic axis of the QWP was varied from 0° to 180° in steps of 10°. Its phase retardance was calculated at each position**. Figure 2.2** shows the plot of phase retardance as the optic axis of the QWP was rotated. The standard deviation of the measured phase retardances was 0.89° which demonstrates the system's insensitivity to sample axis rotation in the plane perpendicular to ranging of the laser light.

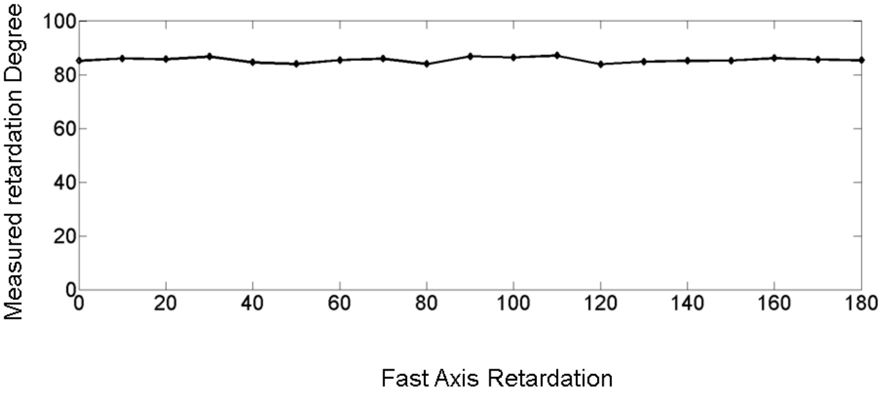

Figure 3.2 Plot of measured retardance as a function of fast Axis orientation.

The shared objective lens ensures that the PS-OCT and MMP systems are imaging the same region of interest. The co-registration of the systems was validated by constructing OCT en-face images and comparing them to the MMP system. C-scans of 4×4×1.5 mm

(256×256×520 pixels) were generated by ImageJ (National Institutes of Health, Bethesda, MD) using a stack of B-scan OCT images collected at different lateral positions from the sample. En face images were then generated by extracting and summing signals within a constant depth (2mm) of the three-dimensional data. Orientation of CCD camera for MMP and scanning voltage for PS-OCT is finely adjusted for the purpose of co-registration. **Figure 2.3** shows the images from PS-OCT (a) and MMP (b). In this example the number 3 from a ruler was displayed at the same position in both images, demonstrating the spatially co-registration of two systems in a single platform. All images were smoothed with a 3x3 Gaussian Filter.

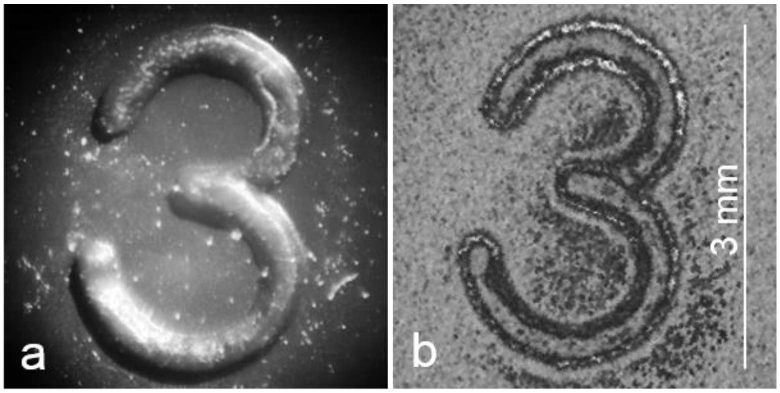

Figure 3.3 Co-registration image of engraved industrial plastic: a) MMP, b) PS-OCT.

2.2.2 Biological Samples

Heart leaflets were excised from baboon hearts donated from the Mannheimer Foundation which had previously euthanized the animals for reasons unrelated to our study. The hearts were stored in a -80°C freezer as tissue awaiting disposal before being acquired. Heart valve leaflets are highly birefringent due to their abundance of collagen fibrils. Changes in the concentration, or orientation of collagen fibrils within the leaflets, may cause alteration of the birefringence signature. Collagenase was selected in order to cause structural damage to the tissue. Chemical damage was induced by incubating a portion of the leaflet (2 mm × 2 mm × 0.5 mm) for 20 min in a solution of 0.14g collagenase powder dissolved in 2.8 mL phosphate-buffered saline (PBS), 0.3 mL fetal bovine serum (FBS), and 0.3 mL anti-microbial solution at 37^{o} C. The experiment was used to demonstrate the sensitivity of PS-OCT-MMP to varying birefringence resulting from collagen contained in the leaflet. Birefringence maps were generated from the PS-OCT images, while Mueller matrix decomposition was performed on images taken by the MMP.

In a second set of experiments, freshly excised bovine tendons, obtained from the local abattoir, were extracted from the posterior side of the hind limbs. Tendon pieces were cut into strips measuring approximately 4 mm × 4 mm × 2 mm. Ultimately, change in the tendon structure was induced through thermal damage. A metal rod was heated at 260^{o}C and then put in-contact with a tendon sample for a period of 2 seconds and for less than 0.5 sec to achieve lower damage. The tendon samples were imaged to allow both the burned and the healthy sections to be visible simultaneously. Finally tendon from the same animal was arranged on a rotational stage so that the axis of the sample could be rotated. Images were taken at -20 and +60 degrees from the principal axis of our system, measured retardation was then compared within both systems.

2.3 Results and Discussion

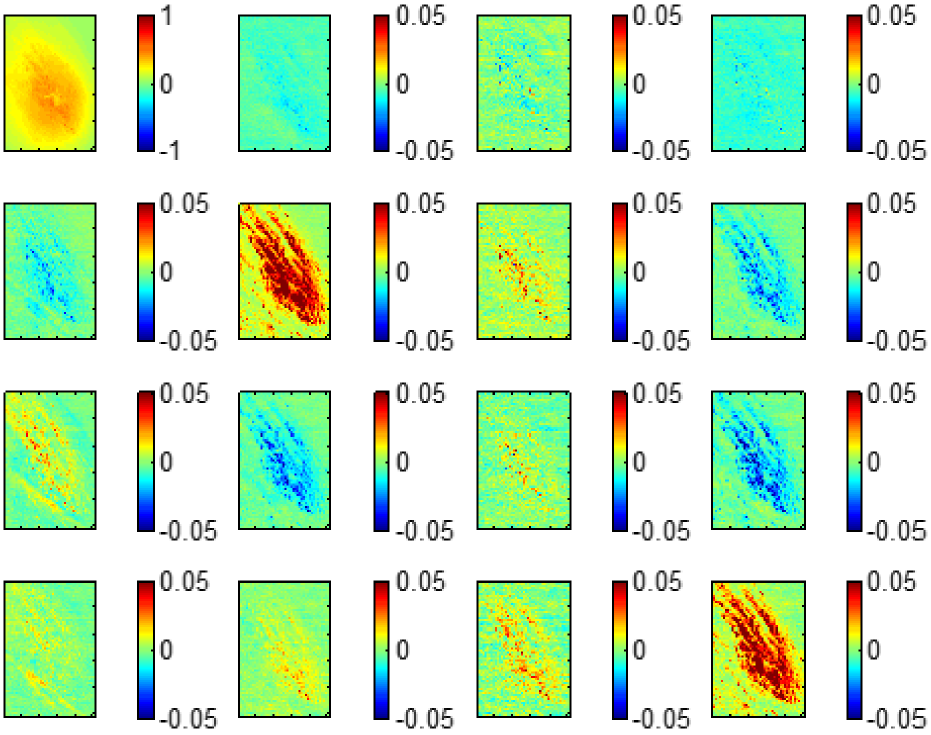

Figure 3.4 Mueller matrix of chicken tendon

An example of a Mueller matrix image generated by our system is shown in **Figure 2.4** from imaging chicken tendon and shows similar patterns in Mueller matrix elements as presented by recent Mueller matrix polarimetry of birefringent tissues. This can be seen as a symmetric pattern around the diagonal of the Mueller matrix with certain elements having reverse signs as discussed by He *et al.* and Sun *et al.* [100, 178].

2.3.1 Heart valve leaflet

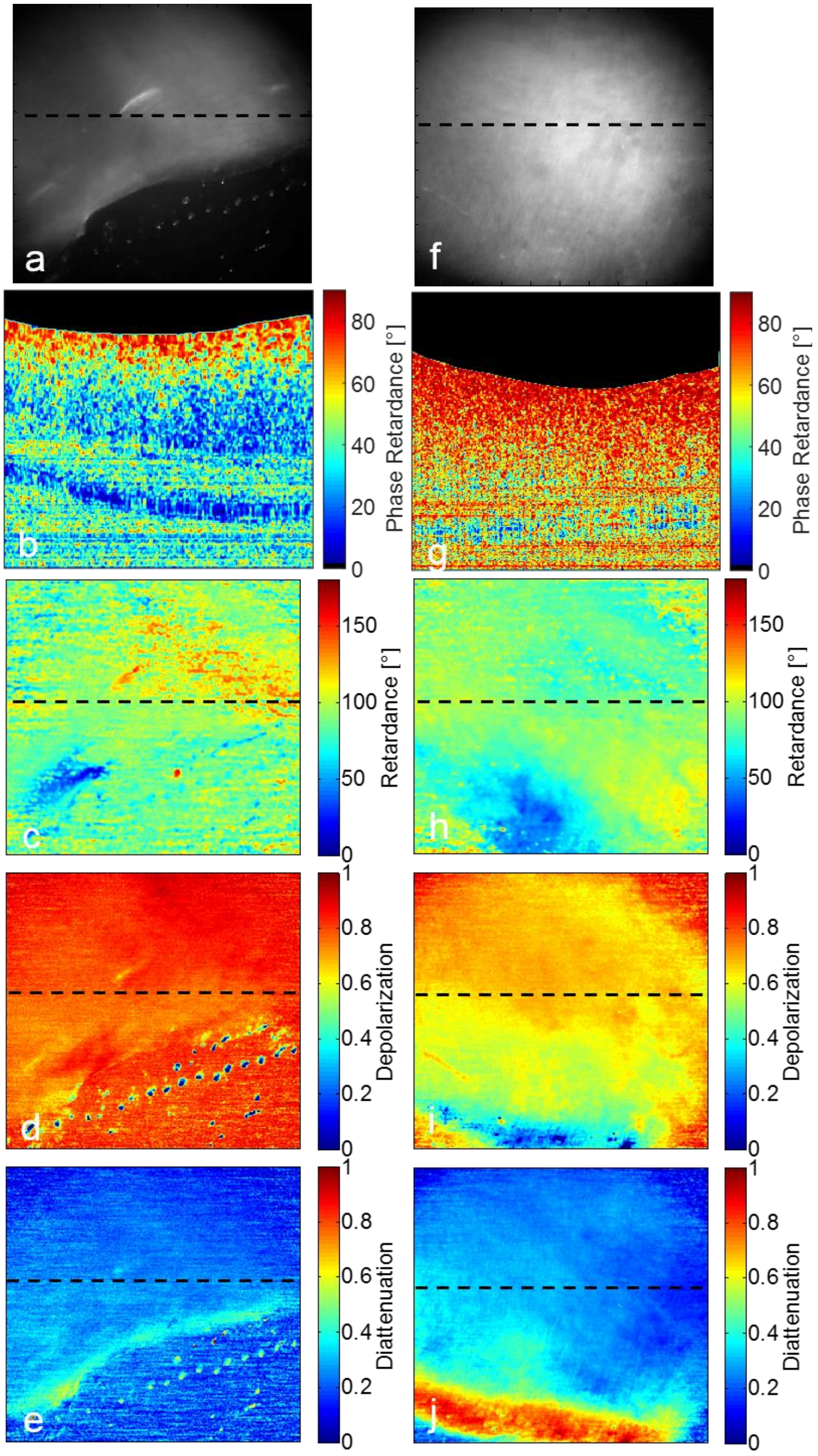

Figure 3.5 Fresh leaflet: a) CCD image, b) PS-OCT B-scan phase retardance, c) MM Retardance, d) Depolarization, e) Diattenuation. Deteriorated leaflet: f) CCD image, g) PS-OCT B-scan, h) MM Retardance, i) Depolarization, j) Diattenuation.

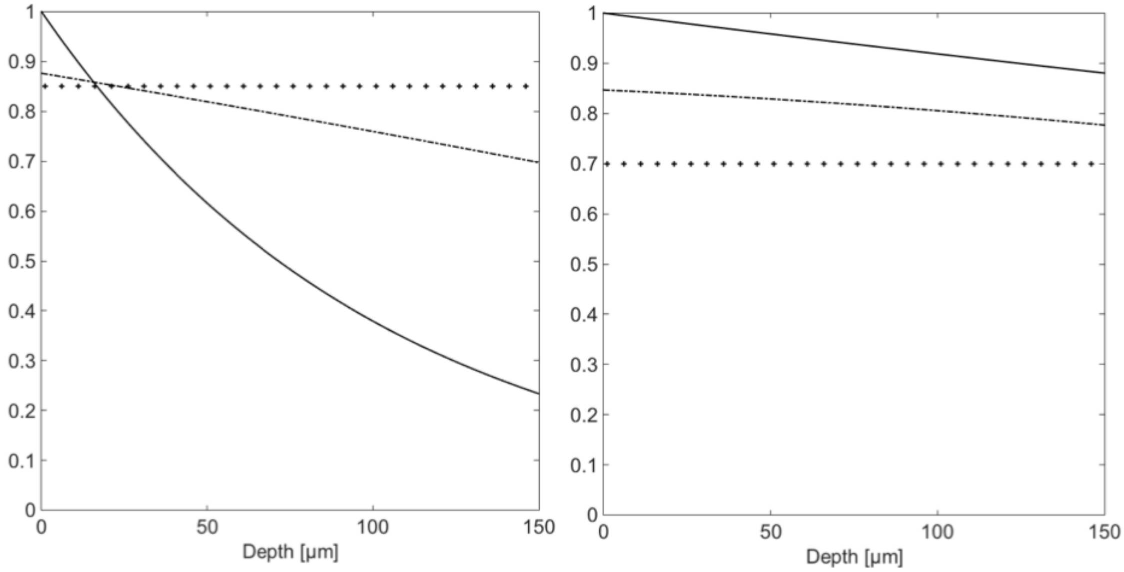

Figure 3.6 Total attenuation (solid), DOPU (dot dashed line), Total Depolarization (crosses): a) Fresh leaflet, b) Damaged leaflet

Results of the Mueller Matrix decomposition and PS-OCT imaging of heart valve leaflets are shown in **Figure 2.5**. The black-dotted line indicates the location of the PS-OCT B-scans, and the dark spots oriented diagonally in **Figure 2.5e** are water droplets located on the stage as seen in **Figure 2.5a**. Clear differences in the birefringence of the leaflet was observed between the fresh and collagenase deteriorated samples shown in **Figure 2.5**. The depolarization values of the fresh leaflet is greater when compared with that of the deteriorated leaflet as shown on a scale of 0-1.0 in **Figures 2.5d** and **2.5i**, 1.0 indicating a complete depolarization of the incident polarized light. The decrease in depolarization can be correlated with **Figures 2.5b** and **2.5g** which show PS-OCT b-scan images of the fresh leaflet and deteriorated leaflet, respectively. The PS-OCT image in **Figure 2.5b** shows a half oscillation (i.e, the full oscillation is shown by a color change from red to blue and again to red), indicating a phase shift of ≈90° this is in contrast with **Figure 2.5g** in the collagenase treated sample, where the retardance is highly uniform throughout the deteriorated leaflet. This may be attributed to the loss of anisotropy and birefringence due to the randomization and destruction of collagen fibrils via collagenase activity. The destruction of the oscillatory pattern in phase retardance caused by loss of birefringence may explain the decrease in the depolarization effect of the tissue and can also be correlated with a loss of collagen content due to collagenase activity [179-181]. There is negligible difference between the Mueller matrix decomposed diattenuation between leaflet samples while in the retardance images some heterogeneous changes can be noticed particularly in the top portion of the figure. Calculation of the total depolarization obtained with Mueller Matrix polarimetry are finally related to the Degree of Polarization Uniformity (DOPU) introduced by Götzinger *et al.* [182]. DOPU is expressed mathematically as resembling the expression for the Degree of Polarization (DOP) often used in optics[2]. Since PS-OCT is based on coherent light detection the DOP is always equal to unity. The DOPU expression instead yields values <=1, the main hypothesis being that by spatial averaging the local Stokes vectors of a sample concomitant speckles are also averaged.

$$DOPU = \sqrt{Q_{mean}^2 + U_{mean}^2 + V_{mean}^2}$$

The calculation of the DOPU is achieved with a two-dimensional sliding average window in (x , z) directions. In our case the window was 10 pixels x 10 pixels, similarly to what used by others [183]. The total depolarization of the treated and untreated sample relate positively to the DOPU, as both metrics are higher in the untreated sample. While the total depolarization is cumulative the DOPU can be studied over depth as shown in **Figure 2.6**. Similarly we may calculate the attenuation coefficient for the samples. This is done utilizing the intensity image and then calculating the loss of intensity over depth, 50 pixels in the x directions were averaged to increase the signal to noise ratio (SNR). The data was ultimately fit with an exponential function of the form $I \approx \sqrt{(e^{-2\mu_{tot}L})}$ where μ_{tot} is the total attenuation coefficient and L is the depth of the sample, 2 is added to account for the round-trip travel [184]. In the figure only the fitted data is shown (solid lines). In **Figure 2.6** we summarize the results of our quantitative analysis. Higher attenuation is expected to influence the total depolarization calculated through Mueller Matrix polarimetry. For the samples shown the total attenuation coefficient was μ_{tot}= 9.6 mm^{-1} for untreated leaflet and μ_{tot}= 0.6 mm^{-1-} for the treated leaflets. DOPU is lost at a higher rate in the untreated sample than the treated ones, indicating a higher depolarization ability of this sample, this is ultimately reflected in the Mueller Matrix assessment of Total Depolarization (crosses in **Figures 2.6a**, and **2.5d**) which is higher for untreated than treated samples.

2.3.2 Tendon

Fresh tendon is highly birefringent due to its collagen structure, its birefringence can be decreased through thermal damage. When the collagen in the tendon denatures due to heating, or other injuries, a decrease in birefringence can be observed.

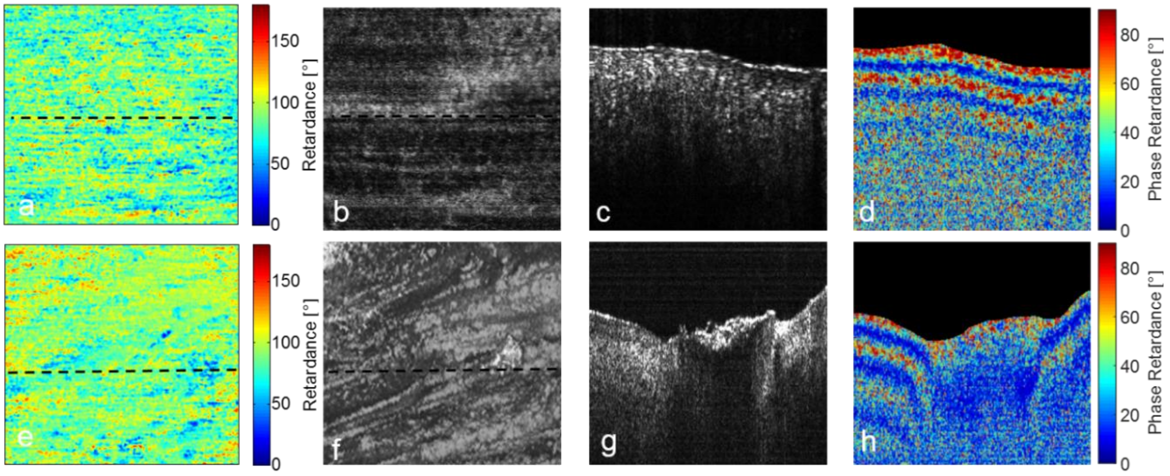

Figure 3.7 Fresh bovine tendon: a) MM Retardance, b) OCT en face, c) OCT B-scan, d) PS-OCT B-scan. Superficially burned bovine tendon: e) MM Retardance, f) OCT en face, g) OCT B-scan, h) PS-OCT B-scan.

In PS-OCT of fresh tendon seen in **Figure 2.7d**, the banded structure, indicative of birefringence, is clearly visible to a depth of 750 microns and making full oscillations between 90° and 0° as polarized light travels deeper into the tissue. This is expected in tendon, which has high optical anisotropy. **Figure 2.7a** is a retardance image taken of fresh tendon by the MMP and shows some areas of greater retardance in an image with retardance mostly between 60°-100°. **Figure 2.7b** is an en face image of the surface of the fresh tendon. The black-dotted line indicates the location of the PS-OCT b-scan in the MMP and OCT en face images. A strong and uniform pattern of phase retardance consistent with undamaged tendon can be seen around the burn site in **Figure 2.7h**. The image clearly shows a disappearance in the birefringence at the center of the burned zone. For comparison, **Figure 2.7g** shows OCT image of the total backscattered intensity of the burned tendon. Less backscattered light from the burned area is observed. The colored bands changing around the burned area in **Figure 2.7h** reveal important structural information not evident in the OCT B-scans of either tendon sample.

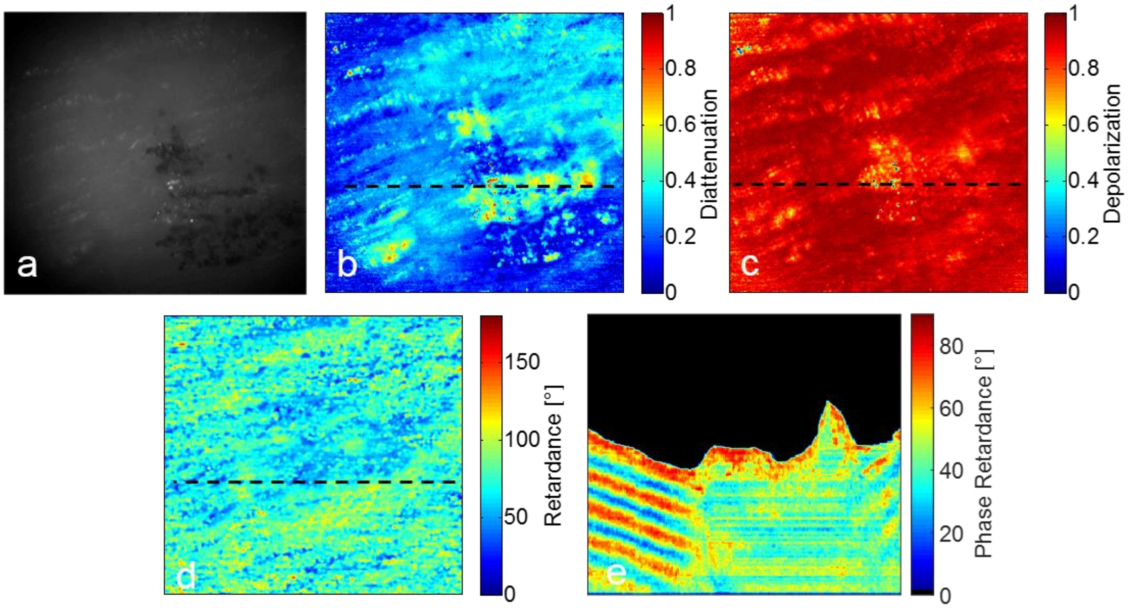

Figure 3.8 Burned bovine tendon: a) CCD image, b) Diattenuation, c), Depolarization, d) MM Retardance, e) PS-OCT B-scan.

Figure 2.8 shows the tendon that was burned for 2 seconds while the superficially burned tendon is seen in **Figure 2.7**. There is a clear difference between the samples. Seen in **Figure 2.8a**, the darkened area at the center of the image and the area towards the bottom right of that section represent the locations where heat was applied. There is substantial increase in the diattenuation of the tendon in **Figure 2.8b** where the darkened burn marks are present in the raw image. The actual burns themselves show a decrease in diattenuation compared to the rest of the image in focus and illuminated. Note that diattenuation relates to a material's favorable absorption of linearly polarized light in a specific orientation. The constriction of collagen fibers between the burns may factor in the area of heightened diattenuation. In the PS-OCT image of **Figure 2.8e**, a section of uniform phase retardance can be seen towards the right of the oscillating pattern typically exhibited by tendon. This section indicates the burned tissue similar to how the burned tendon in **Figure 2.7**. **Figure 2.8c** shows that there is a decrease in depolarization at the center of the burns.

Finally, Fig. 9 shows the results obtained with a chicken tendon sample oriented at two different orientations. The dotted-line on the PS-OCT B-scans indicates where the data for the local phase retardation calculations were taken.

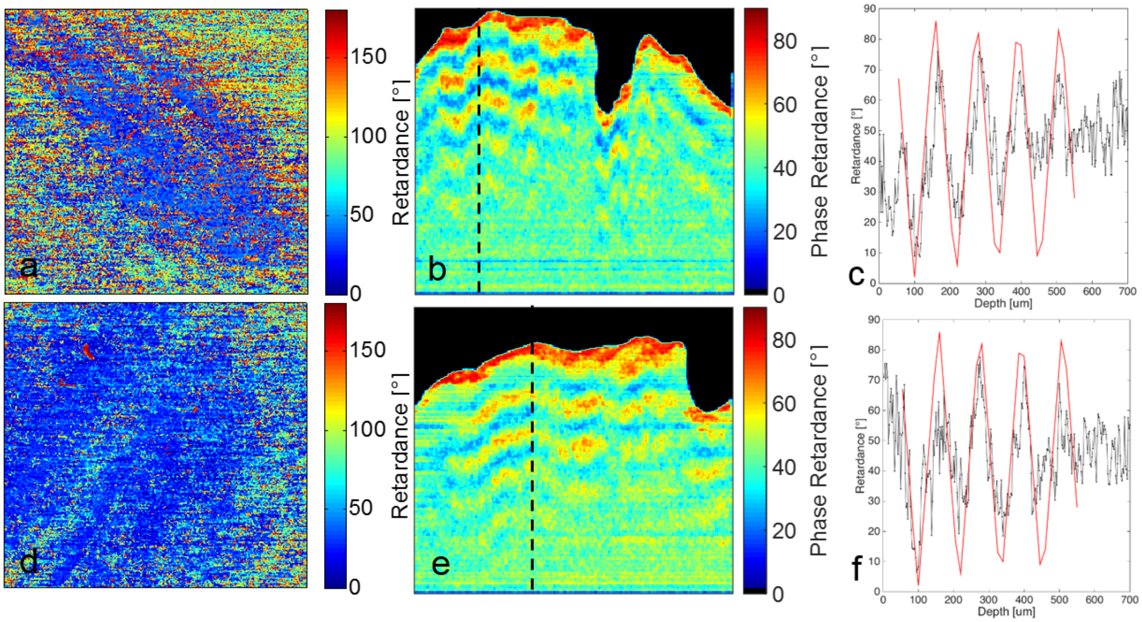

Figure 3.9 a) Chicken Tendon MM Retardance orientation 60^0, b) Cumulative phase retardation c) Local phase retardation data and model d) Chicken Tendon MM Retardance orientation -20^0, e) Cumulative phase retardation f) Local phase retardation data and model. The model fitted to the data is plotted in red.

The chicken tendon showed in **Figure 2.9** reveals little change in the Mueller matrix decomposed retardance as the tendons orientation is changed beneath the sample objective shown in **Figures 2.9a** and **2.9c**. This is also shown in the PS-OCT and corroborated in other work involving axis orientation and retardance [185]. The PS-OCT images of retardation show the typical oscillatory pattern, as the other bovine tendon samples. Local retardation was ultimately calculated with the algorithm by Jiao *et al.* [167] and proposed by others [168].

The results of the fit to the cumulative data are shown in **Figure 2.9**. Using this approach the sample is modeled as a stack of retarders within the imaging apparatus. The determination of the modeling retarder retardation and spacing is critical to this approach. In our calculation the local retardation for the sample was calculated as 25 degrees with each retarder being ~ 30 µm in thickness. In comparison the cumulative retardation obtained with the Mueller Matrix is in the range of 25 to 35 degrees. Further work remains to be done to truly understand how the two measurements relate to each other.

2.4 Conclusion

We have introduced a combined PSOCT-MMP and illustrate how this multimodal imaging technique can provide structural information of tissues using heart valve leaflets and tendon. Damage of leaflet structure with collagenase was identified by decomposing the depolarization parameter of the Mueller matrix, showing that the tissue had less of a randomizing (lower attenuation coefficient) effect on polarized light backscattered from the leaflet. Several authors are using the Degree of Polarization Uniformity for automatic segmentation of the Retinal Pigmented Epithelium (RPE) [182, 183] and other depolarizing structures. This seems counter-intuitive, as the Jones calculus does not account for depolarization yet these authors consider the random polarization state of the resulting speckle as causing the DOP to be lower than 1. With our approach the true depolarizing property of a sample, calculated through the decomposition of the Mueller Matrix was related to the PS-OCT DOP. Not only the DOP and DOPU were consistent for the samples under study, but their behavior seems to relate to the attenuation coefficient and the scattering property of the material that can be extrapolated through PS-OCT. We acknowledge the fact that on layered structures such as the retina the localization of the depolarization is not feasible without a robust inverse model nevertheless this is a first attempt at relating the DOPU and DOP directly.

Areas of thermal damage to tendon were also observed by decomposing the diattenuation and depolarization components of the Mueller matrix in the deeper burned sample. Changes in the normal retardance pattern of tendon were identified where large changes in depolarization and diattenuation were seen in the more severely burned tendon. It was expected that significant damage to birefringent tissue would change its effect on polarized light as normal structure and scattering profile is lost. This experiment shows how PS-OCT could be used to corroborate Mueller Matrix results as they could show changes in material properties at different depth that are not visible through wide field imaging. Finally, the last example in **Figure 2.8** shows another potential application of this approach. Both Mueller Matrix polarimetry (in back reflectance) and PS-OCT can provide measurement of cumulative retardation of a sample and birefringence. In PS-OCT models have been proposed to convert the cumulative retardation into local retardation [166] yet true quantification of this parameter seems elusive. The combined approach could be utilized to refine models of local retardation, particularly as many models rely on the measurement of the surface retardation as a starting point for the model [168]. Naturally this would require a clear understanding of the Mueller Matrix sampling depth, as well as uniform and well-calibrated samples ultimately combined with a computational approach. In conclusion we believe that this combined approach is a starting point in obtaining more quantifiable PS-OCT measurement and at the same time we believe that PS-OCT could be used in this combined system to better understand Mueller Matrix decomposition results. Further work is needed to achieve both goals.

2.5 Acknowledgements

This study was supported by the Herbert Wertheim College of Medicine, Florida International University. We would like to thank the Mannheimer Foundation for their donation of heart samples that would have otherwise gone to waste. Finally we want to thank Dr. Shuliang Jiao for his help and suggestions in the implementation of the PS-OCT system.

CHAPTER 3

[2]Use of Mueller matrix Polarimetry and Optical Coherence Tomography in the characterization of cervical collagen anisotropy

Joseph Chue-Sang[1], Yuqiang Bai[1], Susan Stoff[1], Mariacarla Gonzalez[1], Nola Holness[3], Jefferson Gomes[1], Ranu Jung[1], Amir Gandjbakhche[4], Viktor V. Chernomordik[4], Jessica C. Ramella-Roman[1,2a)]

[1]Department of Biomedical Engineering, Florida International University (FIU), Miami, FL, USA, 33174
[2]Herbert Wertheim College of Medicine, FIU, Miami, FL, USA 33199
[3]Nicole Wertheim College of Nursing and Health Sciences, FIU, Miami, FL, USA 33199
[4]Eunice Kennedy Shriver National Institute of Child Health and Human Development, Bethesda, MD, USA
a) Author to whom correspondence should be addressed. Electronic mail: jramella@fiu.edu

Abstract:

Preterm birth (PTB) presents a serious medical heath concern throughout the world. There is a high incidence of PTB in both developed and developing countries ranging from 11%-15%, respectively. Studies have shown there may be numerous precursors to PTB including infections, genetic predisposition, nutrition and various other morbidities which all lead to a premature disorganization in the cervical collagen resulting in the weakening of the structure designed to keep the fetus in utero. The changes in cervical collagen orientation and distribution may prove to be a predictor of PTB. Polarization imaging is an effective means to measure optical anisotropy in birefringent materials such as those rich in collagen as the cervix is. Non-invasive, full-field Mueller Matrix polarimetry (MMP) imaging methodologies and optical coherence tomography (OCT) imaging were used to

---

[2] This chapter was accepted for publication by the Journal of Biomedical Optics (August 2017). 10.1117/1.JBO.22.8.086010

assess cervical collagen content and structure in non-pregnant porcine cervixes. The OCT imaging was used to verify the efficacy of the MMP in assessing changes in collagen orientation.

Keywords: anisotropy, birefringence, collagen, polarized light imaging, Mueller matrix, OCT

3.1 Introduction

The cervix is an extension of the lower part of the uterus comprising a portion of the female reproductive system. It is cylinder shaped, approximately three to four centimeters long and three centimeters in diameter and has a central canal through its entirety. Changes in cervical structure, morphology, and color may be indicative of disease[96-99]. Non-invasive imaging techniques may provide important diagnostic information non-invasively and for this reason, and recent work in cervical imaging has shown great promise[96, 100-104].

For example, De Martino *et al*. used Mueller Matrix Polarimetry to differentiate between cancerous and non-cancerous cervical samples by measuring depolarization and retardation of excised human cervixes.[105, 106] Richards-Kortum *et al*. used confocal microscopy to identify differences between normal, pre-cancerous and cancerous cervical tissues. [107-110] Ramanujam *et al*. engineered means for cervical imaging for low-resource settings [111], and so did Levitz *et al*.[112] Recently, Hendon *et al*. [102, 113-115] used optical coherence tomography to identify collagen orientation of human ex-vivo cervixes to investigate differences in collagen angular distribution between pregnant and non-pregnant cervixes. Finally, Second Harmonic Generation imagery has been used to observe changing collagen architecture in the cervix providing exquisite images of fibrous and fibrillary collagen structure. [79, 101, 116-120]

In this paper, we focus on collagen arrangement in the cervix. We propose a combined OCT Mueller Matrix approach to image the cervix. Our intent is to highlight the ordered structure of the cervix through MM decomposition focusing particularly on the orientation of the collagen bundle fast axis and compare them to OCT imaging which has been shown to be able to measure the ultrastructure of the cervix. This imaging modality can potentially be done non-invasively in the clinic through the modification of existing colposcopes to function as MM polarimeters.

3.1.1 The Cervix

A cartoon representation of the cervix is shown in **Figure 3.1**. The cervical canal serves as the entrance, via the vagina, for sperm in reproduction and as an exit canal, via the uterus, for childbirth. The two ends of the canal are termed internal orifice (os) connecting to the uterus and external OS at the vagina. The cervix is divided into two regions due to their cellular differences, the ectocervix, and the endocervix. The ectocervix, the lower area, is visible through the vaginal opening and is comprised of a stratified squamous epithelium, having several cell layers of differing morphological characteristics. [92] The cell layers of the epithelium are subdivided into classes relating to their maturation and include one layer of basal cells, two layers of parabasal cells and numerous layers of both intermediate cells and superficial cells. The thickness of the epithelial layer is between 200 and 500 microns. [93] [94] The endocervix is lined with a single layer of mucus secreting columnar (glandular) epithelial cells. The area of intersection of the ectocervix and endocervix is called the transformation zone and in this location, glandular epithelium is being replaced by squamous epithelial cells.[95]

3.1.2 Collagen in the cervix

An extracellular matrix (ECM) lies under the epithelium of the cervix, separated by the thin basal lamina layer of collagen type IV fibers [93], and consists mainly of collagen, approximately 10-15% smooth muscle cells [123, 124 125] and a ground mixture of biomolecules.

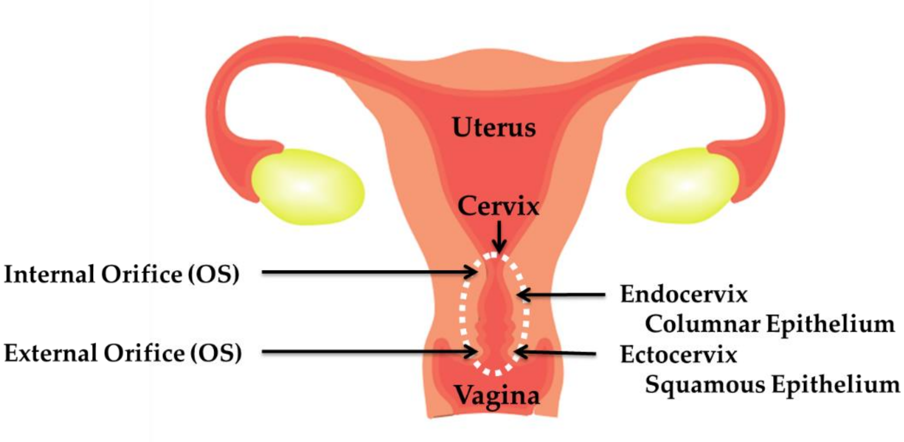

Figure 5.1 The cervix

Two types of collagen comprise the cervical ECM, approximately 70 % is collagen type I and 30 % collagen type III. [126, 127] In addition, the ground substance of the ECM contains glycoprotiens elastin and fibronectin, glycosaminoglycan (GAGS) decorin, buglycan, chondroitin sulfate, keratan sulfate, and dermatan sulfate, hyaluronic acid and water. [123, 125, 128-130]

The role of the cervix is to serve as a barrier, to maintain the baby *in utero* until gestation is complete and to preserve the fragile environment of the uterus. When childbirth is near, the cervix softens and opens to allow the baby to exit the uterus. During pregnancy, the epithelial layer of the cervix may thicken. [186] Mechanically, the cervix must be strong to hold the fetus throughout gestation. The collagen of the cervix provides this necessary strength.[86]

Numerous researchers have studied the collagen of the uterus to determine how this structure maintains its integrity during pregnancy. [77-84] Aspden *et al*. found the structure of collagen is oriented in three unique areas surrounding the cervical canal, the anisotropic alignment of the collagen differing within each area. The cervical fibrils are aligned both around and along the canal for increased strength as shown in **Figure 3.2**. [12, 85-87]

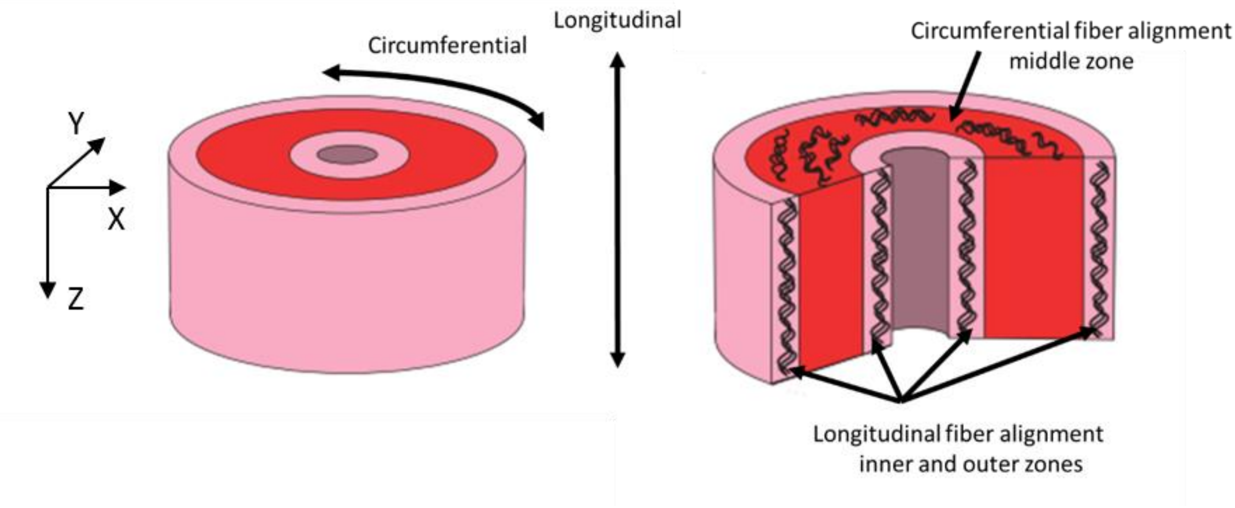

Figure 5.2 Alignment of collagen fibers in human cervix in three anisotropic zones

The cervix undergoes dramatic changes between the initial pregnant state and delivery of a baby. Many of these changes are not yet well understood, nor are all the factors which cause these changes. The cervix's state during a post pregnancy has been categorized into four phases: cervical softening, ripening, dilation and repair (postpartum). [130,81, 143]

The physiological properties of the cervix are altered by a cascade of micro-environmental events in each of these phases. Cervical softening begins within one month of the initiation of pregnancy and the cervix undergoes increased vascularity and edema. [81] Softening is a longer, more steady phase than the others, progressing through the 33rd week of pregnancy. The collagen of the stroma becomes less organized and the cervix becomes pliable and begins shortening. Timmons *et al*. states this as a maintenance of tissue competence occurring while increasing tissue compliance. [143] The ripening phase begins, after softening, and as House *et al*. points out, this predominantly deals with the cervix changing roles from a load-bearing function to a birthing canal. [124] By the end of cervical ripening, when dilation begins, some researchers have found there is a 30-70% decrease of collagen [128, 130, 136] since the onset of pregnancy, although Myers *et al*. believe there is a decrease in crosslinking but not in actual collagen content. This is purported to be due to increased solubility in weak acids rather than change in collagen content. [12] In addition, there is also a decrease in specific glycosaminoglycans (chondroitin sulfate and dermatan sulfate) [144], and an increase in the hydrophilic glycosaminoglycan [145], hyaluronic acid [139] and thus, an increase in water (5 – 10%).[124] [146] [147] Researchers have also found there occurs a shift from insoluble to soluble collagen [128, 148] with as much as 90% soluble collagen by the third trimester[124]. Dilation follows ripening and involves an influx of leukocytes, [124] similar to an inflammatory response, which may serve to cause an increase in the matrix metalloproteinase, collagenase. [81] [149] [150] Collagenase causes the breakdown of collagen cross links and allows the cervix to weaken [12] [79] [151] and open thereby radically changing shape by shortening and effacing in preparation for delivery of the baby.

3.2 Materials and Methods

A combined optical coherence tomography and Mueller matrix polarimetry (OCT-MMP) system introduced in previous work[153] was modified to a fiber based OCT shown in **Figure 3.3**. The system is based on a Michelson interferometer. The laser light source is a broadband superluminescent diode (Bayspec, San Jose, CA) with 840 nm central wavelength and 50 nm full width at the half-maximum (FWHM) bandwidth. A telecentric scan lens (LSM03-BB, Thorlabs, Newton, NJ) focuses the light onto the sample and collects the backscattered light. Galvanometer-mounted mirrors (GVS012, Thorlabs, Newton, NJ) on the sample arm enable transverse beam scanning on the sample. A custom-made spectrometer detects and measures the interference signal between reference arm and sample. The spectrometer consists of a collimating lens with a focal length of 75 mm (Edmund Optics, Barrington, NJ), an 1800 lines/mm volume holography transmission grating (Wasatch Photonics Logan, UT), an assembly of triple lenses with an effective focal length of 150 mm, and a line array CCD camera (spL4096-140k, Basler, Highland, IL). Data processing algorithm, control and display software are developed using MATLAB (Mathworks, Natick, MA). The images produced by the system have a theoretical resolution in depth of 5 µm per pixel, and an axial resolution of 20 µm per pixel.

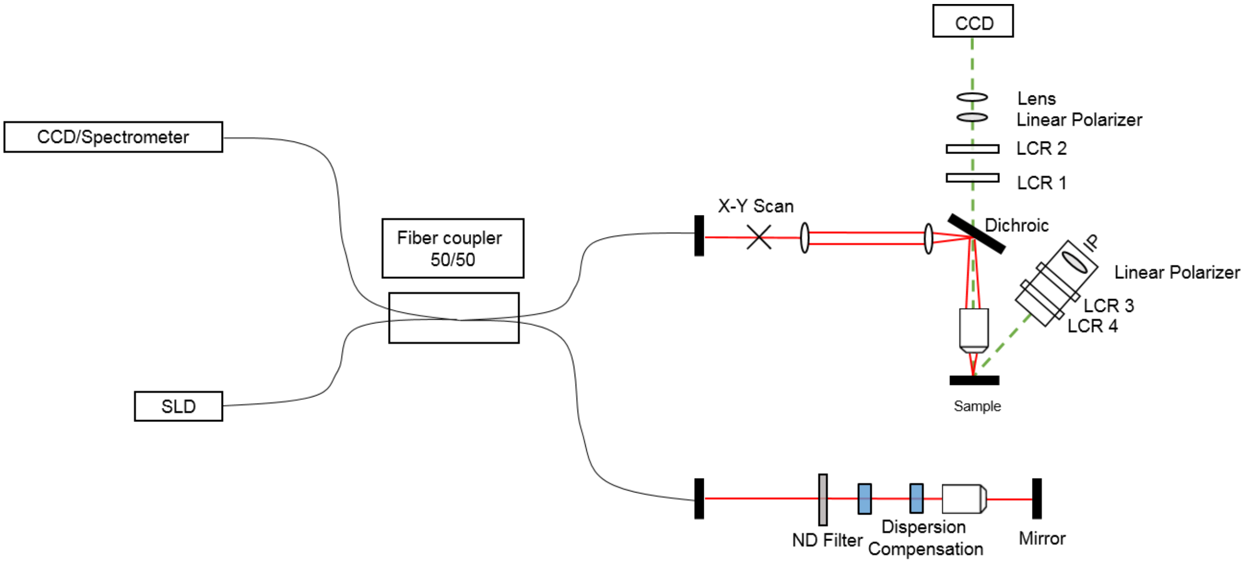

Figure 5.3 Combined OCT and Mueller matrix system schematic (Red light-OCT, Green-dashed-MMP). The OCT's components are traced by the red light

The co-registered Mueller matrix system shown in **Figure 3.3** is traced by the dashed green line and consists of a CCD camera (Lu175, Lumenera, Ottawa, ON) with a Computar

MLH-10X 1/2-inch 13-130mm f5.6 10X Macro Zoom lens. The camera was secured above the sample objective to allow focusing on the height adjustable stage. A linear polarizer (Prinz, Northbrook, IL) and two liquid crystal retarders (LCR) (Meadowlark Optics, Frederick, CO) between the lens and sample objective form the polarization state analyzer (PSA) of the polarimeter. Employing the same sample objective for the two imaging systems ensures they are imaging the same region of interest. The illumination port (IP) in **Figure 3.3** indicates the light source for the MMP. A 530 nm LED (M530L, Thorlabs, Newton, NJ) was oriented to illuminate the sample at an incident angle of 45° and collimated with a 30 mm diameter tube and a 75 mm focal length plano-convex lens (Newport, Irvine, CA). Two LCRs were mounted after the light source and a linear polarizer using a cage system to form the polarization state generator (PSG). The calibration of the MMP system follows a standard methodology utilized by our group in several applications [176, 187] and resulted in a condition number of 2. A Mueller matrix of Air was also acquired and showed an error well below 1%.

3.2.1 Mueller matrix Decomposition

Mueller matrix imaging is a useful polarimetry technique as the 4 x 4 Mueller matrix completely characterizes the polarimetric properties of a sample [19 56]. Mueller matrix decomposition is often used to extract constituent polarization properties from a Mueller matrix of any unknown complex system. The decomposition of the Mueller matrix (M) (as proposed by Lu-Chipman[57]) yields three canonical matrices $M = M_\Delta M_R M_D$: a M_Δ accounting for the depolarizing effects of the material, a retarder matrix M_R for the effects of the material linear birefringence and optical activity, and a diattenuator matrix M_D includes the effects of linear and circular diattenuation. By decomposing the Mueller matrix, we are hence able to isolate different light-tissue interaction mechanism. [20, 57, 179, 188] Furthermore, the resulting matrices can be analyzed to yield quantitative medium properties that have a demonstrated [7] useful diagnostic power and they are used in this study. We have identified two such parameters as relevant to this study – these are linear retardance δ, birefringence which relates to the abundance of collagen in the cervix, and slow axis orientation θ, which is directly related to the orientation of the collagenous structures in the tissue. The orientation calculation used was derived by Ma *et al* [178]. Another parameter that may be of interest is depolarization, with which we can observe changes in the extracellular matrix such as shortening and thickening of collagen. Because the information decomposed from a Mueller matrix is contained in each pixel of the image, no processing is required afterwards to generate parameters of interest. As an example, retardation axis orientation is directly calculated from the Mueller matrix at each pixel to generate the orientation images. The MMP images show a resolution of 12.0 µm/pixel.

Circular statistics [189, 190] is a subset of statistics for data that can be shown on a unit circle such as directions where the sign of values is determined by the direction of rotation. The periodicity of such data requires a departure from normal arithmetic statistics, which would give a faulty representation of the mean of the data set. Circular statistics was applied to the orientation data decomposed from the Mueller matrix in order to calculate directional parameters. This method requires that the data first be transformed into unit vectors with two-dimensional data as shown in **Equation 3.1**. **Equation 3.2** is the mean resultant vector $\bar{r}$ of the data set. The mean angular direction $\bar{\alpha}$ can be calculated using the four quadrants inverse tangent of $\bar{r}$.

$$r_i = \begin{pmatrix} \cos \alpha_i \\ \sin \alpha_i \end{pmatrix} \tag{3.1}$$

$$\bar{r} = \frac{1}{N} \sum_i r_i \tag{3.2}$$

Kurtosis and mean angle were calculated in our study. Circular kurtosis is the measurement of outliers in a distribution, the distribution's propensity to produce outliers, and is associated with the weight of the tails in a data set [191]. It is useful as a measurement of how uniform a distribution of angles is in a data set, which can be confounded in mean calculations where a wide array of values can equal a certain mean angle depending on their frequency. An equal distribution of angles will give a kurtosis of 0, while a narrow distribution of angles will move towards 1.

3.2.2 OCT image processing

In previous work Gan *et al*.[102] utilized unpolarized spectral domain OCT to determine the distribution of collagen in the cervix. Their algorithm uses pre-processing of images to first promote edge detection of fibers in different depth planes of the OCT acquired 3D stack, before determining the orientation of sub-sections in the planes. This is done over selected regions in the sample. The orientation information across different regions can then be stitched together to create a more complete orientation map of the entire region that was imaged. We aim to mimic their approach to measuring the orientation of birefringent tissue using OCT, and to compare it with Mueller matrix polarimetry (MMP), which should generate orientation information inherently summed across all depths in the sample for the entire field of view.

Our approach pre-processed and averaged the *en face* data in a similar manner suggested by Gan *et al*. The determination of orientation, however, was calculated using our own method, which applies the Radon transform and calculation of the projection angle SNR as shown in **Figure 3.4**. The radon transform projects the sum of image intensities along the different orientation angles inputted into the transformation. It is useful for calculating which angles are represented in an image.[192]

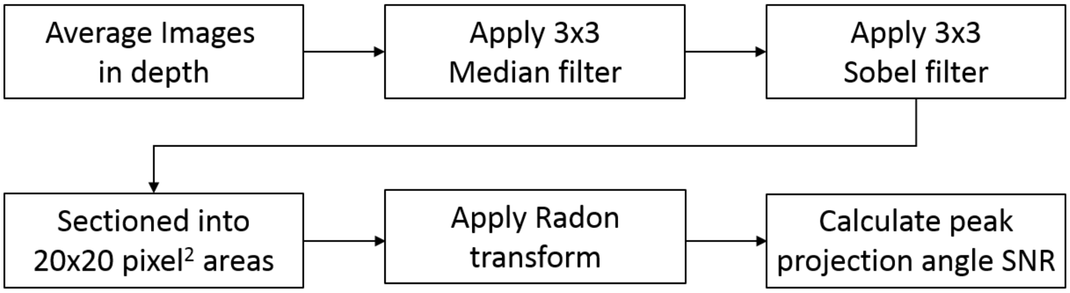

Figure 5.4 OCT processing pipeline.

Five X-Y images (c-scans) were first averaged in the Z-direction to improve the orientation measurements. The c-scans were then smoothed with a 3x3 median filter to remove speckle noise. The resultant matrix was then convolved with a 3x3 Sobel filter to generate an image with emphasized edges in order to detect contours in the sample. This matrix was sectioned into 20x20 pixel areas and Radon transformed. The SNR of all projection angles was calculated for the Radon transformed section using Equation 3 to produce a graph such as in **Figure 3.5**. SNR is defined here as the quotient of the standard deviation of a projected angle with the standard deviation of the entire image section. The peak projection angle SNR is denoted by a triangle and selected to be overlaid over the section of the enface image of the sample as a line. This peak corresponds to the orientation of the sample as is calculated for sections throughout an enface image of the sample [192].

$$SNR = \frac{\sigma_R(\theta)}{\sigma_1} \tag{3.3}$$

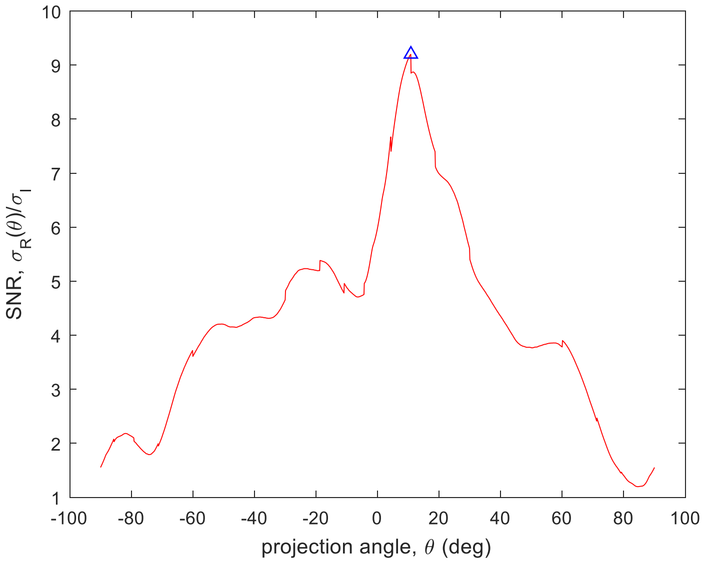

Figure 5.5 Radon transform of section of silicon phantom

The orientations measured by both imaging techniques were superimposed over the images they were calculated from as oriented lines. OCT was used as a standard for testing the effectiveness of MMP in this application.

3.2.3 Anisotropic Test Samples

Two test samples were used to verify the efficacy of the OCT-MMP's orientation measurements. The first sample is an extruded silicon phantom. The extrusion process creates striations oriented in a single direction, which are easily observed by eye and measured by protractor creating a highly anisotropic sample with a known retardation axis. Its low scattering and absorbing properties as a mostly transparent material ensured that there would be minimum loss of polarization in the light returning to the MMP. It produced the best measure of orientation out of all the samples used. Porcine tendon was another test sample with high anisotropy that was investigated. Highly ordered collagen in tendon has a strong and uniform birefringence, which is the basis for the MMP's calculation of retardance and orientation. Both orientation samples were rotated on the OCT-MMP sample stage and then imaged.

3.2.4 Cervical Samples

Fresh porcine cervixes were obtained from the abattoir ranging from 1 cm to 2 cm in diameter. They were then fixed in 4% paraformaldehyde (PFA) and embedded in paraffin for preservation. Tissue fixation with paraformaldehyde and paraffin embedding has been shown to cause small increases in depolarization and retardation [193-195], however there is no significant effect on sample birefringence. The embedding process first began with dehydrating the tissue with successive washes of ethanol (EtOH) from 50-100% concentration in steps of 10% for 10 minutes each wash. The washing was repeated with solutions of EtOH:Citrisolve in concentrations of 2:1, 1:1, 1:2, and then three washes of 100% Citrisolve. Lastly, Citrisolve was exchanged for paraffin in vacuum oven set between 54-58°C. First washes of 2:1, 1:1, and 1:2 Citrisolve:paraffin were done for 30 minutes each before using 100% paraffin for 1-2 hours and then leaving it overnight in 100% paraffin. The cervixes were then put in place before the paraffin was set to harden. 10 cervixes in total were imaged; the images reported are representative of the samples.

3.3 Results and Discussion

3.3.1 Test samples - Silicon Phantom and Tendon

All images shown are of the Y-X plane of the cervix denoted in **Figure 3.2**. Orientation of 0° is parallel to the X axis and a positive $\Delta\theta$ is considered counterclockwise from horizontal. The silicon phantom was measured first. Its weak attenuation can be seen in the low depolarization value of the phantom seen in **Figure 3.6b**, the uniform value of retardation in **Figure 3.6c**. The dashed line box in **Figure 3.6a** is the region where orientation was compared between OCT and MMP in **Figure 3.7**.

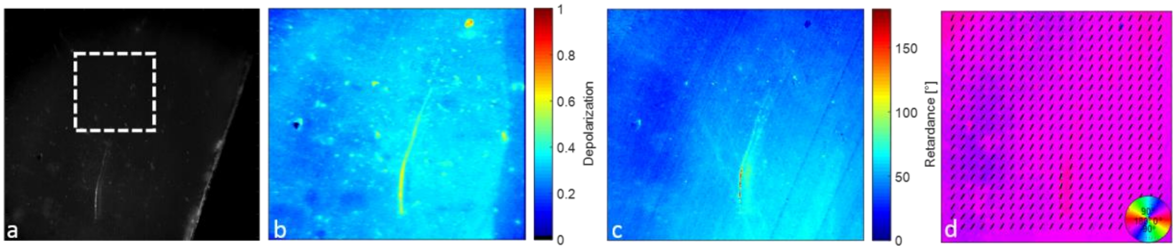

Figure 5.6 Silicon phantom Mueller matrix decomposition: a) CCD image, b) Mueller matrix decomposed depolarization, c) Mueller matrix decomposed retardation, d) Mueller matrix decomposed orientation.

The circular statistics shown in **Figures 3.7b** and **3.7d** were calculated from the regions encased by the dashed line squares in **Figures 3.7a** and **3.7c**. It is important to note that unlike the MMP images which are taken at the surface of the sample, the OCT images are taken below the surface of the sample as they are c-scans averaged in depth. This is why striations can be seen by both imaging modalities in the silicon phantom which was completely uniform in structure throughout the sample but not in the tissue samples. Both imaging modalities had kurtosis values in the 90-percentile range indicating a tight distribution of angles around a mean angle of 68° and 65° for the OCT and MMP, respectively. After the orientation measurements were confirmed to properly change as the phantom was rotated on the sample stage, we moved to tendon as a biological sample which would attenuate light due to scattering and absorbing more than the silicon phantom but still have high anisotropy which would be seen in the orientation measurements.

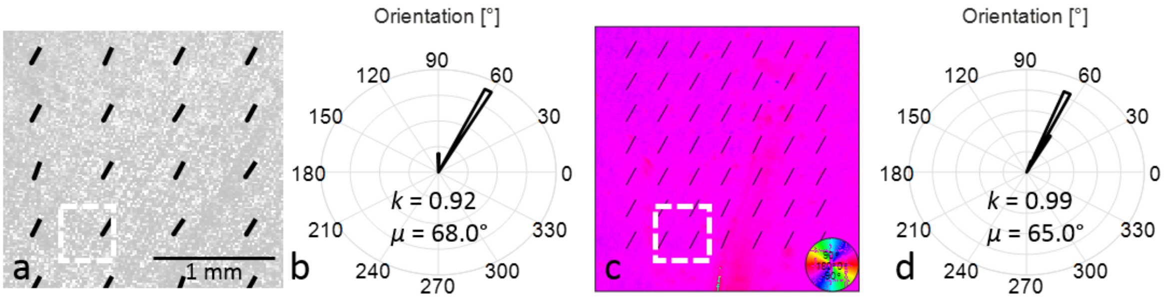

Figure 5.7 Silicon phantom OCT-MMP orientation comparison: a) OCT c-scan, c) Mueller matrix decomposed orientation, b/d) Orientation histogram circular statistics (*k* = kurtosis, μ= mean angle).

The greater attenuation of the tendon is evidenced the much greater depolarization value in **Figure 3.8b** as compared to the silicon phantom. Despite its high anisotropy, tendon does not exhibit retardation as uniform as the silicon phantom. The changes in morphology and roughness of the tendon's superficial layers compared to the silicon phantom can be seen as deviations in the orientations calculated by OCT and MMP in **Figures 3.9a** and **3.9c**.

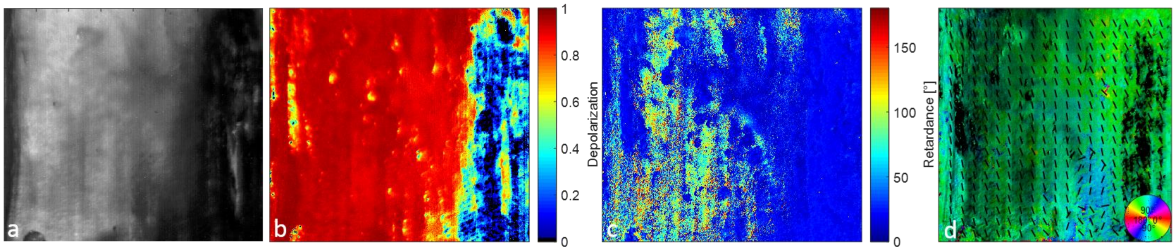

Figure 5.8 Tendon Mueller matrix decomposition: a) CCD image, b) Mueller matrix decomposed depolarization, c) Mueller matrix decomposed retardation, d) Mueller matrix decomposed orientation.

A breakdown in the Mueller matrix orientation is highlighted by a phase wrapping of orientation angle from +70° to -70°. Regardless, the tendon produced high kurtosis values with both imaging modalities around a mean angle of -74° in the selected area.

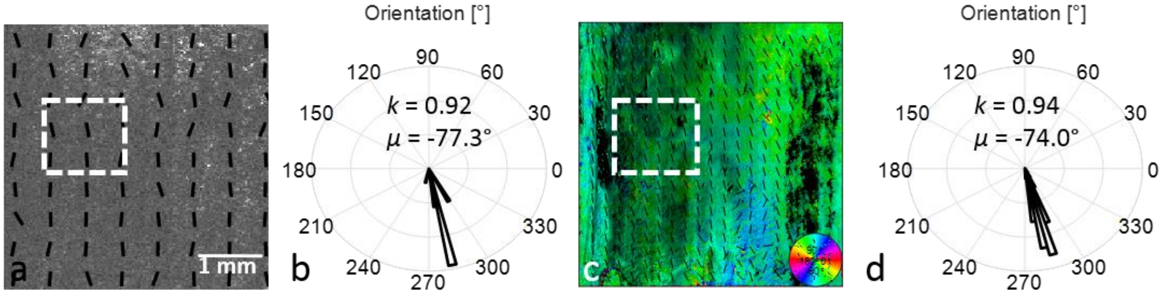

Figure 5.9 Tendon OCT-MMP orientation comparison: a) OCT c-scan, c) Mueller matrix decomposed orientation, b/d) Orientation histogram circular statistics (*k* = kurtosis, μ= mean angle).

3.3.2 *Ex-vivo* porcine cervix

Once both imaging techniques had been tested on the anisotropic test samples, we imaged the paraffin embedded cervixes in order to see whether the circumferential alignment of cervical collagen [birefringent material] could be resolved by the techniques. The inner and outer regions of the cervix contain collagen oriented in the z-direction which cannot be resolved with polarimetry of the sample’s surface. Because of this we are interested in the region between the os and the outer edges of the cervix because it contains collagen circumferentially aligned around the os which can be resolved noninvasively with polarimetry of the surface. Two different cervixes are shown using OCT in **Figures 3.11a** and **3.13a**.[102] Similarly, the orientations calculated by MMP also rotate around the os of the cervixes shown in **Figures 3.11c** and **3.13c**.

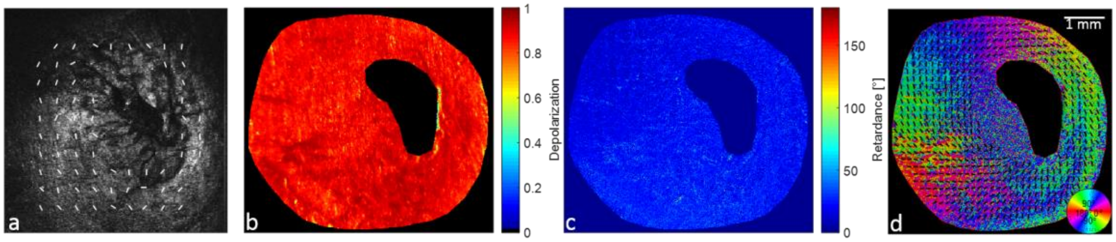

Figure 5.10 Paraffin embedded cervix 1 Mueller matrix decomposition: a) CCD image, b) Mueller matrix decomposed depolarization, c) Mueller matrix decomposed retardation, d) Mueller matrix decomposed orientation.

The dashed line box in **Figure 3.12a** designates the region that was used to measure the orientation shown in **Figure 3.13** for both imaging modalities. Circular statistics were applied to the OCT orientation and Mueller matrix decomposed orientation in the same subsections. The selected subsections of the cervixes are denoted by the dashed line square boxes in **Figures 3.11** and **3.13**.

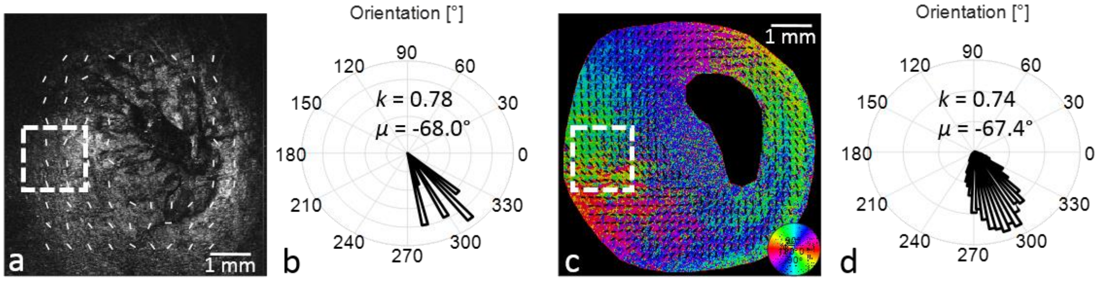

Figure 5.11 Paraffin embedded cervix 1 OCT-MMP orientation comparison: a) OCT c-scan, c) Mueller matrix decomposed orientation, b/d) Orientation histogram circular statistics (*k* = kurtosis, μ= mean angle).

The kurtosis values calculated from the selected cervix region are between 0.74 and 0.78 in comparison to the more ideal values of 0.92 and 0.99 in the non-depolarizing silicon phantom. This is expected due to the strong depolarization effect of biological tissue[3, 105, 153] because of its many constituents and the more complex arrangement of collagen in the cervix as opposed to tendon. Another cervix is shown in **Figure 3.12**; as this sample was large only a section was imaged with OCT, whose field of view is about ~5 mm while the Mueller Matrix system can measure the full cervix.

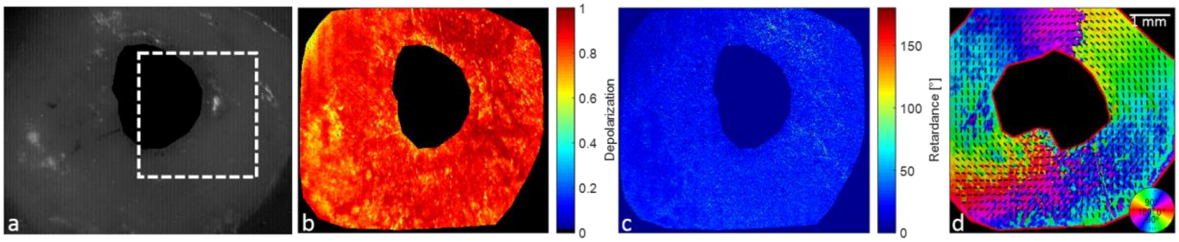

Figure 5.12 Paraffin embedded cervix 2 Mueller matrix decomposition: a) CCD image, b) Mueller matrix decomposed depolarization, c) Mueller matrix decomposed retardation, d) Mueller matrix decomposed orientation.

The dashed line box in **Figures 3.13a** and **3.13c** are the regions selected for the circular statistics calculated in **Figures 3.13b** and **3.13d**, respectively.

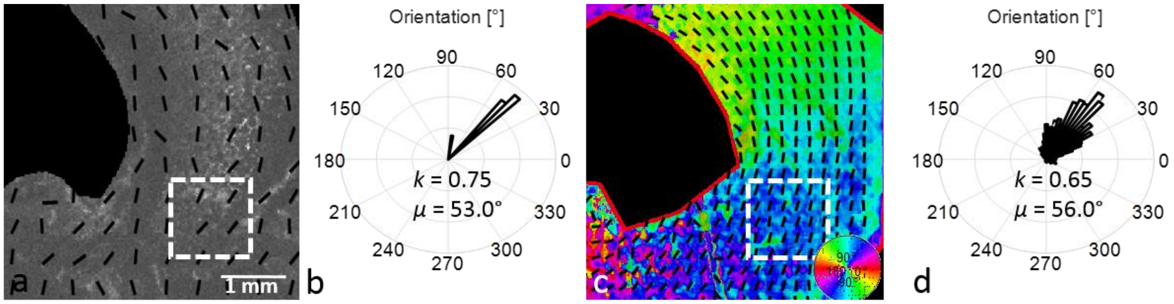

Figure 5.13 Paraffin embedded cervix 2 OCT-MMP orientation comparison: a) OCT c-scan, c) Mueller matrix decomposed orientation, b/d) Orientation histogram circular statistics (*k* = kurtosis, μ= mean angle).

A summary of the circumferential fiber alignment of collagen in the middle of the cervix samples is shown in **Figure 3.14**. Eight regions around the os of the cervix were selected from both the Mueller matrix and OCT data. The mean orientation and percentage error between the two modalities is plotted for comparison. The mean orientation rotates fully around the cervix and flips sign in the vertical axis [north position]. We propose that in-vivo measurements of collagen orientation could be used to identify these areas of disruption and lead to diagnosis of abnormal or early collagen disruption in the pregnant cervix.

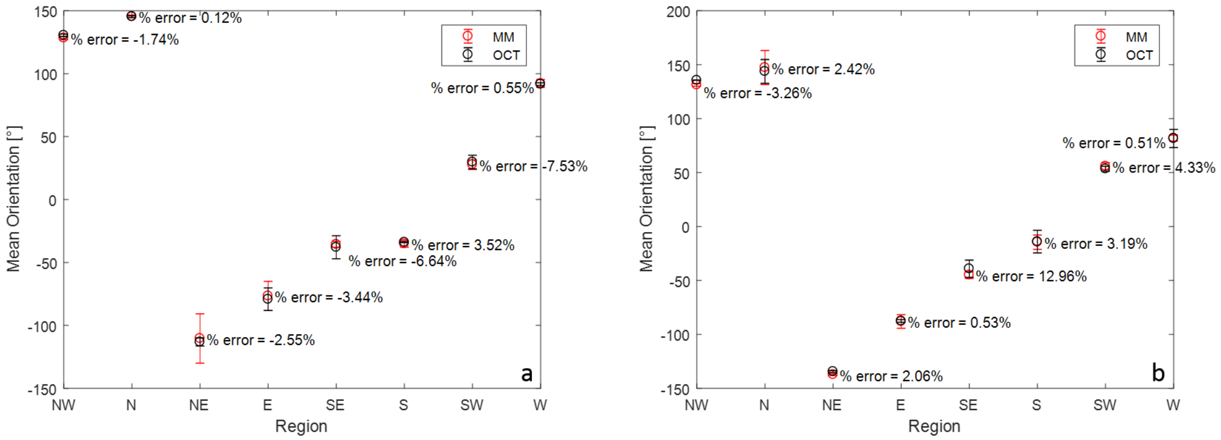

Figure 5.14 Summary statistics of cervix orientation between MMP and OCT.

3.4 Conclusion

Orientation of the optical axis of birefringent material is important in the diagnosis of abnormal conditions in tissues with large amounts of ECM. Tissues that rely on collagen and other common ECM components for mechanical strength align the proteins in various orientations depending on the application.[196] The circumferential orientation of collagen in the cervix is important in maintaining the fetus in the uterus by not allowing passage through the os and can be measured quickly within one set of images using Mueller matrix polarimetry. To our knowledge this is the first report that focuses uniquely on polarization derived collagen orientation in the mammal cervix. Gan *et al* as well as Zhang *et al* have shown that cervical collagen alignment can be measured using OCT and second harmonic generation (SHG) microscopy, respectively[102, 119]. Yet Mueller Matrix polarimetry is more adaptable to cervical imaging studies than those modalities due to its ability to capture the entire cervix at a distance outside the vagina compared to the much greater difficulties in performing OCT imaging or SHG microscopy *in-vivo* and without contact with the sample. Current modalities for diagnosing pre-term labor involve direct contact with the cervix during a pelvic ultrasound[72] or fibronectin discharge collection[73].

Depolarization and retardation were also decomposed from the Mueller matrices and showed little variation throughout the different samples measured due to their structural uniformities that make them ideal test samples and the use of healthy collagenous tissue. Mueller matrix decomposed orientation was compared to and found to be in agreeable with measurements made using optical coherence tomography for the region samples using circular statistics to calculate kurtosis and mean orientation angle. Further studies of collagen orientation in cervixes under different conditions are needed to understand if Mueller matrix polarimetry can effectively measure the changes in collagen orientation that should occur when the normal ECM alignment is disrupted by pregnancy or disease. An in-vivo study of pregnant human cervixes is currently underway using a colposcope outfitted with a MM polarimeter of the same design as reported here and will be useful in establishing the diagnostic power of this technique in the determination of risk for preterm labor.

3.5 Acknowledgements

We gratefully acknowledge the support of the Herbert Wertheim College of Medicine, Florida International University.

CHAPTER 4

[3]Use of Mueller matrix colposcopy in the characterization of cervical collagen anisotropy

Joseph Chue-Sang[1], Nola Holness[3], Mariacarla Gonzalez[1], Joan Greaves[6], Ilyas Sayatashev[2], Susan Stoff[1], Amir Gandjbakhche[4], Viktor V. Chernomordik[4], Gene Burkett MD[5], Jessica C. Ramella-Roman[1,2a)]

[1]Department of Biomedical Engineering, Florida International University (FIU), Miami, FL, USA, 33174
[2]Herbert Wertheim College of Medicine, FIU, Miami, FL, USA, 33199
[3]Nicole Wertheim College of Nursing and Health Sciences, FIU, Miami, FL, USA, 33199
[4]Eunice Kennedy Shriver National Institute of Child Health and Human Development, USA, 20892
[5]Department of Obstetrics & Gynecology, Leonard Miller School of Medicine, University of Miami, Miami, FL, USA, 33136
[6]Holtz Children's Hospital, Jackson Memorial Hospital, Miami, FL, USA, 33136
[a)] Corresponding author Electronic mail: jramella@fiu.edu

Abstract:

Annually, about 15 million preterm infants are born in the world. Of these, due to complications resulting from their premature birth, about 1 million would die before the age of five. Since the high incidence of preterm birth is partially due to the lack of effective diagnostic modalities, novel methodologies are needed to determine risk of preterm birth. In the present study, we propose a noninvasive tool based on polarized light imaging aimed at measuring the organization of collagen in the cervix. Cervical collagen has been shown to remodel with the approach of parturition. In this study, we used a novel full-field Mueller Matrix polarimeter (MMP) to assess and compare cervical collagen content and structure

---

[3] This chapter was accepted for publication by the Journal of Biomedical Optics Special Issue honoring Dr. Steven Jacques (August 2018). 10.1117/1.JBO.23.12.121605

in non-pregnant and pregnant women *in vivo*. Local collagen directional azimuth was used and a total of eight cervixes were imaged.

Keywords: anisotropy, birefringence, collagen, Mueller matrix, cervix, colposcopy.

4.1 Introduction

With the incidence rate exceeding 11% in the United States and 15%[62] in the developing countries, preterm birth (PTB), defined as labor prior to 37 weeks of gestation, is the leading cause of infant death worldwide. PTB is reported to be responsible for infant neurological disorders,[64] long-term cognitive impairment,[65] as well as chronic health issues involving the auditory, visual, digestive, and respiratory systems.[66] In expectant mothers, causes for PTB can include infection, inflammation,[67] vascular disease,[68] short intervals between pregnancies,[69] multiple gestations,[70] and genetic factors. [71]

For an early identification of at-risk pregnancies, as well as to delay the start of labor contractions and thus increase the development time inside the mother, tocolytics, antenatal corticosteroids, and hormones, such as terbutaline**,** betamethasone, and progesterone, are used. A mechanical approach to delay birth is cerclage, which is used to seal the cervix. Among the current approaches to diagnose PTB are tactile and visual inspection of the cervix to determine dilation, ultrasound examination of cervical thickness,[72] and fetal fibronectin (fFN) immunoassay.[73] However, all these approaches have a low positive predictive power, making it difficult for physicians to decide whether or not any intervention should be performed and complicating the development and testing of new treatments. In this context, a more reliable PTB diagnostic method could allow physicians to earlier start intervention to delay birth, so that to give the fetus more development time. Thus, the development of new diagnostic modalities to identify risk of PTB has a great potential in reducing the morbidity of the condition.

Regarding PTB, recent research has highlighted the important role of the collagen of the cervix[74-76] which provides the structure necessary to hold the baby within the uterus during gestation. Numerous studies have investigated the collagen of the cervix to determine how this structure maintains its integrity during pregnancy.[77-84] For instance, Aspden *et al*. found that the structure of collagen is oriented in three unique areas surrounding the internal cervical os, with the anisotropic alignment of the collagen varying within each of the areas. The cervical fibrils are aligned both around and along the cervix os for increased strength.[12, 85-88] While the cervix os and outer regions of the cervix are made of collagen aligned in the direction of the cervical canal, the area in-between these regions contains collagen oriented circumferentially around the canal. In the present study, this angular measurement of collagen orthogonal to the light path was defined as the collagen azimuth.

Optical measurement of cervical remodeling throughout pregnancy based on the observation of the changes in collagen arrangement and density in the cervix os can help predict the occurrence of pre-term labor. To target the fibrous ultrastructure of the cervix, polarization sensitive techniques, such as Mueller matrix polarimetry, can be used. Relevant research has demonstrated the ability of Mueller matrix polarimetry to identify colorectal and cervical cancer.[19, 38, 90] In a previous study, we developed a **PReterm IMaging System (PRIM)** based on a standard colposcope, with a high sensitivity to cervical ultrastructure (see **Figure 4.1**). This methodology was tested on excised porcine cervixes, and the results were compared to images produced by optical coherence tomography (OCT) before being used to image human cervixes *in vivo*.[91] Ex-vivo porcine cervixes were imaged using OCT and MMP. The OCT was used as a comparison due to its use in cervix by another group[102] which we replicated as a standard. The results were compared, and both modalities (OCT and MMP) were found to show similar circularly aligned collagen around the internal cervical os.

In the present study, we targeted the change in collagen alignment around the os for three different reasons. Firstly, the Mueller matrix polarimetry modality takes images of the surface of the cervix and thus provides a summation of the birefringence media beneath that surface. It has been shown that the circumferential alignment of collagen present at the vaginal end of the cervix is preserved going towards the uterus end of the structure using MRI.[131] It is this direction of collagen orientation that our system is capable of characterizing. Secondly, the majority of the cervix's volume consists of collagen oriented circumferentially around the os rather than the inner and outer boundaries which contain collagen aligned along the os. The PRIM will be able to characterize the collagen in the largest amount of surface area available to be imaged. Lastly, the exposed portion of the cervix that can be imaged in pregnant and nonpregnant patients does not have present changes sufficient enough in their depth or curvature so as to cause PRIM to lose focus between different areas of the cervix. The small outer region of the cervix which is not part of the stiffer structure around the os in non-pregnant patients is not considered in the images. This stiff structure flattens as pregnancy progresses and becomes less of an issue for imaging.[197] A previous study using MRI has demonstrated that, as pregnancy progresses, the vaginal end of the cervix increases in its surface area, and this change does not occur predominantly in one direction. The uniform increase in circular area means that the os is not strongly stretched in any one direction, which can skew orientation alignment.[198]

4.2 Materials and Methods

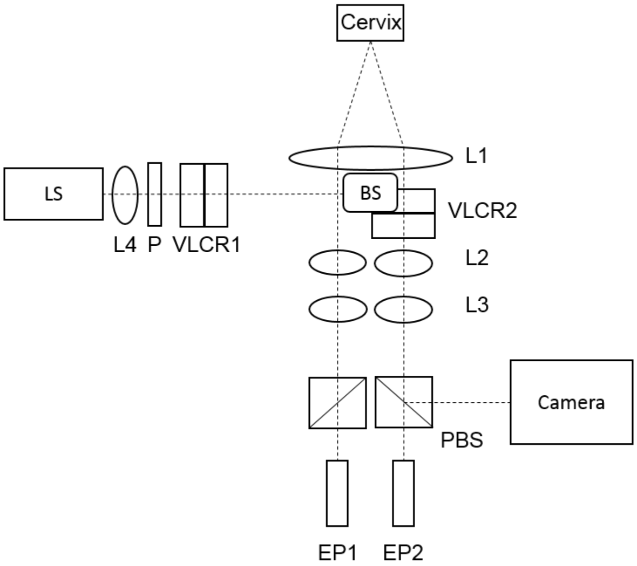

Figure 8.1 PReterm IMaging System (PRIM). Variable liquid crystal retarder (VLCR), polarizer (P), lens (L), polarizing beam splitter (PBS), eye piece (EP), light source (LS).

In reported elsewhere[199], the PRIM builds on a standard colposcope (Seiler Instruments) with the addition of polarization optics. Images are acquired with a sCMOS camera (pco.edge, pco., Kelheim, Germany), with lenses L1-L3 being standard to the colposcope for directing the reflected light from the sample on to the eyepieces and the camera port. A 565 nm LED (M565L3, Thorlabs, Newton, NJ) light source is mounted vertically in the illumination port, replacing the fiber optic cable connected to the original white light lamp source. A linear polarizer (Thorlabs, Newton, NJ) and two variable liquid crystal retarders (VLCR1) are mounted after the light source to form the polarization state generator (PSG).

Two liquid crystal retarders (VLCR2) (Meadowlark Optics, Frederick, CO) and a polarizing beam splitter (PBS) between the camera and L1 form the polarization state analyzer (PSA). In essence, this is the reverse configuration of the PSG. Other groups have used different approaches to polarimetry, such as Vitkin's use of four photoelastic modulators.[200-203]

In the present study, a total of 16 images were acquired to create a full Mueller Matrix following the dual LCVR (variable liquid crystal retarder) approach.[37, 91, 105, 153] To this end, the LCVR of the PSG were activated sequentially at four different voltage levels to create four different input polarization states—namely, 0°, 45° 90°, and elliptical polarization. For each PSG value, a set of four images was acquired by activating the PSA LCVR set at different voltage levels. Calibration of the MMP system was performed by a standard methodology previously used by our group[176, 187] and resulted in the condition number of 3.32. The Mueller matrix of air was constructed with the error below 1%.

4.2.1 Mueller Matrix Decomposition

Mueller matrix decomposition extracts constituent polarization properties from a Mueller matrix of any unknown complex system.[19, 56] As proposed by Lu-Chipman,[57] the decomposition of the Mueller matrix (M) yields three canonical matrices accounting for (1) material depolarization (M_Δ); (2) retardance due to linear birefringence, and (3) optical activity (M_R), and diattenuation (M_D) (see **Equation 4.1**).

$$M = M_\Delta M_R M_D \tag{4.1}$$

Following Ma *et al.*,[178] we identified two such parameters relevant to the present study: (1) abundance of birefringent collagen δ (retardance) and (2) slow axis orientation θ, related to the orientation of collagen bundles in the tissue. Information decomposed from a Mueller matrix was calculated for each pixel; therefore, we generated parameters of interest of an area after using a median filter on the image. Our MMP resolution was 12.5 μm/pixel with the CCD size of 2560 x 2160 pixels, allowing for the 2.7-cm field of view.

4.2.2 Image Processing

In order to improve the quality of the orientation images, nine post-processing steps were performed (see **Figure 4.2**). First, the movement artefact in an *in-vivo* experiment was considered using the PRIM (Step 1). During the 6-second acquisition time, large movements were not commonly observed, as the patient was still sitting down with her feet in stirrups from the prior gynecological exam. When a movement occurred, it was mostly in the lateral directions, as it would be caused by the patient's waist adjusting on the seat. In these cases, ImageJ (NIH, Bethesda, MD) was used to co-register the image stack without changing the intensity. After imaging with the PRIM, the orientation and depolarization data were calculated from the Mueller matrix constructed from the raw intensity images (Step 2). A 3 x 3 median filter was then applied to smooth out the noise from the orientation data and to create a more gradual transition of angles around the cervix by mitigating the effect of outlier pixels with a shift in the orientation value (Step 3). Thereafter, to ensure that the regions farther away from the cervix os were not cut off with the image rotation, the orientation and depolarization images were zero padded with 500 pixels at each boundary in preparation for rotation around the cervix os (Step 4). After manually setting the boundaries of the cervix os, subsections around the cervix were automatically selected by an algorithm. This algorithm creates a center point for the cervix from the weighted centroid of the os. From this center point, 50 x 50-pixel subsections were then generated in the vertical and horizontal directions (Step 5). Doing so allowed to automatically generate histograms of the distribution of collagen azimuth and other statistical analyses without bias in selecting the data, as well as facilitated differentiation of where data points were located relative to the landmarks in the cervixes, such as the os. During this process, the cervix os and the area surrounding the cervix were excluded from the actual cervix data. The images were rotated 10° each iteration until the complete 360° rotation was completed. Steps 6 and 7 were performed on the same set of orientation data. Therefore, the entirety of the cervix could be analyzed using different methods with the same subsections (datasets) (see Section 2.3 for further detail on circular statistics). The orientation images were analyzed at each iteration by first applying a mask over the data, so that pixels corresponding to a depolarization value less than 0.5 were not considered in the final analysis (Step 8). This removed the areas of saturation caused by specular reflectance from the calculations of the orientation lines that were later projected over the images and allowed no lines to be present in the areas of low depolarization. A retardance threshold mask was also applied in order to remove the areas of dense mucus (a white buildup in the pregnant cervix, see **Figure 4.4**) from the calculations.

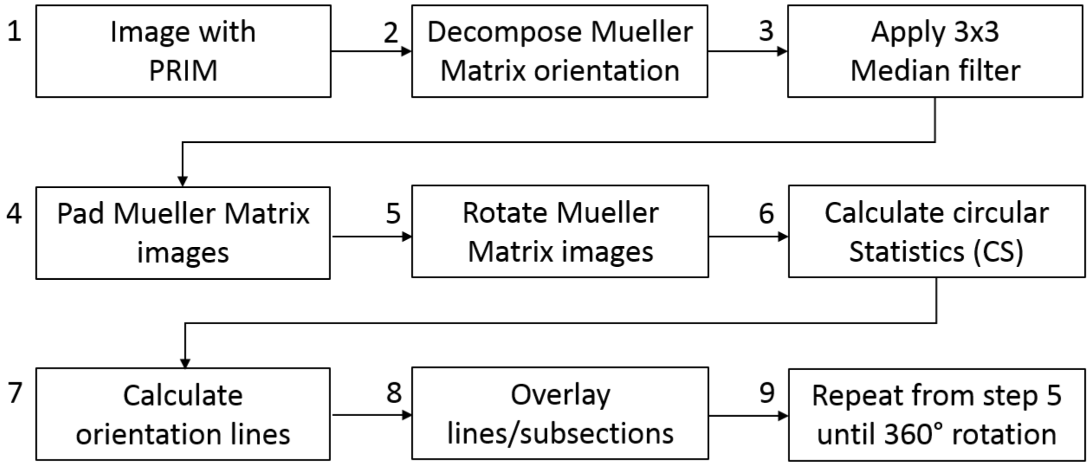

Figure 8.2 The MMP image processing pipeline

Thereafter, following Jan *et al*.,[204] a third mask was then applied to the orientation data. The parameter calculated was used to create what Jan et al.[204] referred to as a weighted polarization "energy" mask, for each pixel depending on its response to the changes in incident polarized light. Pixels with a high energy are generally those with strong birefringence (i.e. higher collagen content) due to their strong response to polarized light. By using this parameter as a gradient mask, it was possible to highlight the areas of strong birefringence while shading areas with progressively less response from the incident polarized light. The areas around spots of low depolarization (saturated pixels) were also shaded by this energy mask. After reducing the noise in the orientation data using the depolarization mask, the originally sized 2560 pixels x 2160 pixels orientation image was sectioned into 50 pixels x 50 pixels areas and then averaged to calculate the mean angle used to generate their representative lines and overlaid over a grayscale image of the sample. The orientation lines were calculated from the 50 x 50-pixel regions to give a summary graphic of the mean distribution of the collagen azimuth. The color representation of collagen azimuth in the orientation images already showcased the highest resolution possible for the PRIM system on the pixel-by-pixel basis. Finally, the kurtosis image was then calculated from the orientation data.

4.2.3 Circular Statistics

Circular statistics[189, 190] is a subset of statistics for the data that can be shown on a unit circle where the sign of values is determined by the direction of rotation, such as in the case of vector coordinates. In this kind of data, 10° is synonymous to 190°. Normal arithmetic statistics with these two values would yield a mean of 100° when they are in fact the same azimuth angle. Therefore, errors in calculation such as this can skew the interpretation of the angular data away from the real retardation axis present. The periodicity of such data requires a departure from the normal arithmetic statistics which would give a faulty representation of the mean of the dataset. In the present study, circular statistics was applied to the orientation data decomposed from the Mueller matrix to calculate the directional parameters of the cervical ultrastructure. This method requires that the data are first transformed into unit vectors with two-dimensional data (see **Equation 4.2**), where θ is the retardation orientation calculated per pixel from the Mueller matrix. **Equation 4.3** is the mean resultant vector $\bar{r}$ of the dataset. The mean angular direction $\bar{\theta}$ can be calculated using the four-quadrant inverse tangent of $\bar{r}$.

$$r_i = \begin{pmatrix} \cos\theta_i \\ \sin\theta_i \end{pmatrix} \tag{4.2}$$

$$\bar{r} = \frac{1}{N}\sum_i r_i \tag{4.3}$$

In the present study, we computed kurtosis and mean angle. Circular kurtosis is the measurement of outliers in a distribution, the distribution's propensity to produce outliers, and is associated with the weight of the tails in a dataset[191]. It is useful as a measurement of how unfluctuating a distribution of angles is in a dataset which can be confounded in mean calculations. A flat distribution of angles where all angles are equal in frequency indicates randomness of orientation and will give a kurtosis of 0, while a narrow distribution of angles with few outliers (a small tail) indicates a strongly aligned structure and the kurtosis value will move towards 1. Kurtosis images were generated similarly to how the orientation lines were, but from smaller moving windows of the 5 pixels x 5 pixel areas of the orientation images. In this way, a kurtosis image can be generated from the entire cervix with the same dimensions of the depolarization and orientation images calculated from the Mueller matrix. At the same time, kurtosis was also calculated in the 50 pixels x 50 pixels regions of the orientation data sectioned in the vertical and horizontal directions centered on the os. An example of these sections can be seen in **Figure 4.4a** where the blue sections have a kurtosis above 0.6. This calculation was performed at every 10° rotation of the image. The ratio of high to low kurtosis sections (KI) was calculated over 360°.

4.3 Results and Discussion

To test the ability of our system to ascertain collagen distribution in the live cervix, two different studies were conducted. Study 1 was conducted at the **S**imulation **T**eaching **a**nd **R**esearch Center (STAR Center) at FIU and focused on healthy non-pregnant women. In this study, the aim was to obtain normative data for further comparison. Approval for *in-vivo* imaging of human patients was granted by Florida International University's Internal Review Board (IRB-15-0466-CR01). Study 2 was conducted in the triage unit of Jackson Memorial Hospital, Miami. IRB approval (IRB-16-0244) was obtained both at FIU and Jackson. In Study 1, inclusion criteria were non-pregnant woman aged between 18 and 59 years old. Women who were menstruating were excluded because of the difficulty in analyzing the images due to menstruation discharge. Women with abnormal cervixes and women who reported themselves to be pregnant were also excluded. In Study 2, inclusion criteria o were pregnant patients past 24 weeks of gestation and who self-referred themselves to the hospital for the possibility of going into labor. Patients with any kind of pathology in the vagina, such as yeast infection, were excluded.

The imaging procedure followed a standard colposcopic examination. The colposcope was positioned at about 10 cm from the patient. The cervix was accessed through a speculum by a nurse, allowing the operator to focus the modified colposcope through the eye pieces. The field of view of the digital images and the eye pieces were co-registered. Up to five sets of images were taken per patient. Each acquisition lasted 6 seconds. If the patient started to feel discomfort for any reason at any time, the examination was canceled, and the imaging ended. Representative images are shown in **Figure 4.3**. Orientation of 0° is parallel to the horizontal axis and a positive $\Delta\theta$ is considered counterclockwise from horizontal. The circular color bar in the lower right corner of the orientation images corresponds to this change in the retardation axis angle. The white lines overlaid on the image are a summary graphic of these angles calculated per pixel.

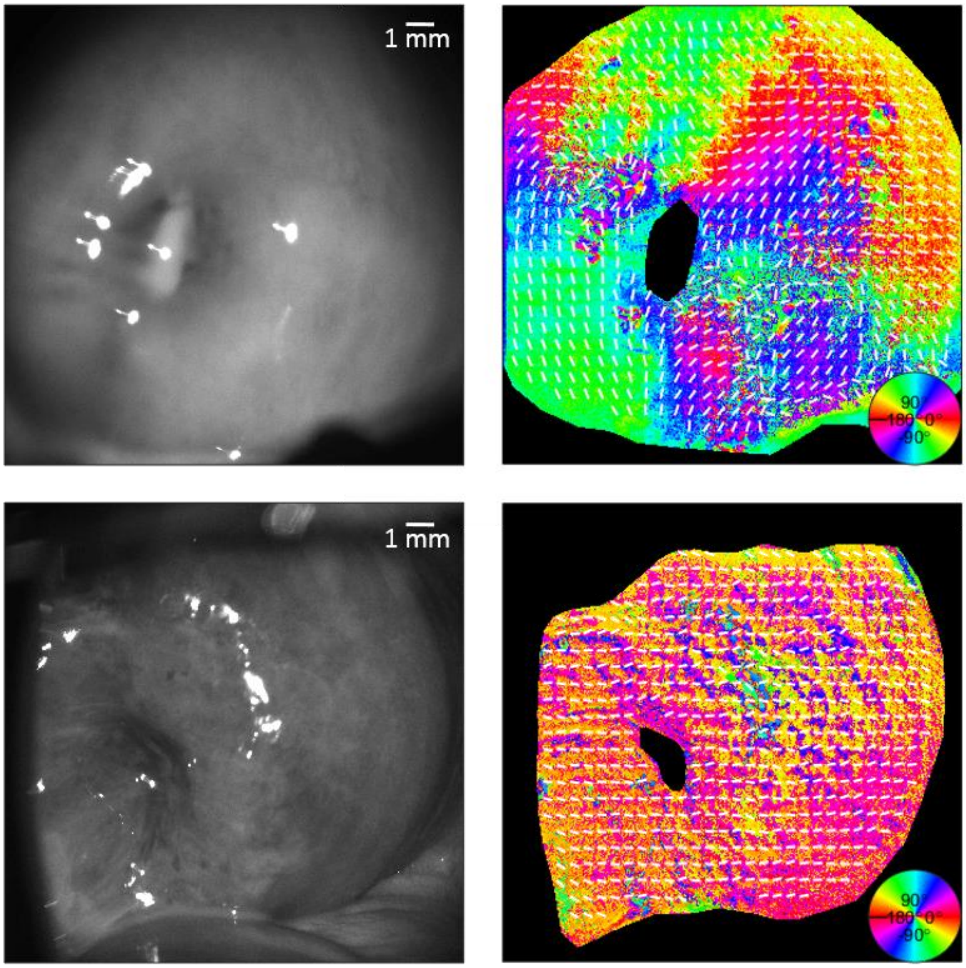

Figure 8.3 *In-vivo* non-pregnant human (top) and pregnant (bottom) cervixes raw image and MMP decomposed orientation. Circular color bar refers to the retarder orientation calculated from the Mueller matrix of the cervix.

An example of collagen orientation calculated from *in-vivo* images taken from a non-pregnant and pregnant human cervix is shown in **Figure 4.3**. An appropriate shift in orientation angle around the cervical os is designated by the color map. There is a greater resolution of orientation shown by the false color in the non-pregnant cervix compared to the pregnant cervix. This more gradual change in orientation will be shown as higher kurtosis. Mueller Matrix decomposition and kurtosis of more samples of human cervixes *in vivo* are shown in **Figures 4.4** and **4.6**.

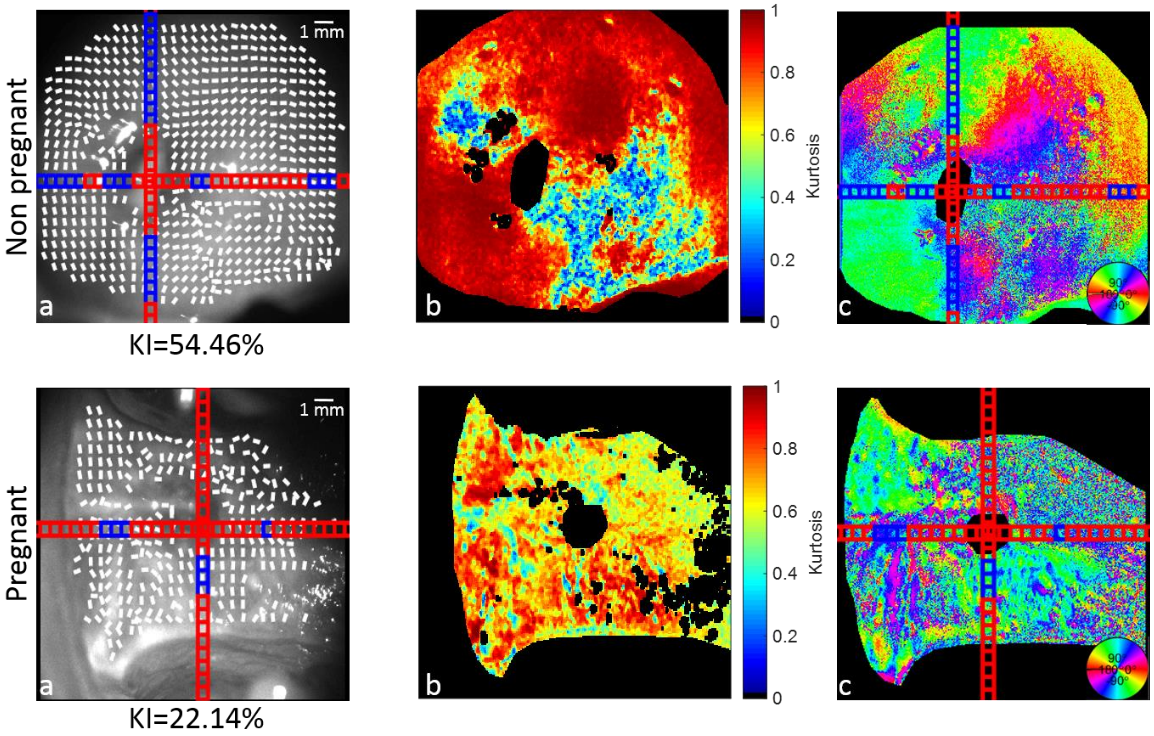

Figure 8.4 *In-vivo* non-pregnant and pregnant human cervixes: a) B/W CCD image with orientation lines: Blue subsections > kurtosis = 0.6 > red subsections, b) Kurtosis, c) Mueller matrix decomposed orientation. KI = % of kurtosis values > 0.6 across the entire sample. Circular color bar refers to the retarder orientation calculated from the Mueller matrix of the cervix.

A non-pregnant cervix can be seen in the first row of **Figure 4.4**. The areas of low depolarization correspond to specular reflectance and were disregarded from the calculation of orientation lines using the depolarization threshold mask described in Section 4.2.2. This can be seen when comparing the saturated pixels in the grayscale image with the kurtosis image of the sample. There are no lines present over the saturated pixels which correspond to the blacked-out areas in the kurtosis. The kurtosis values calculated for the non-pregnant cervixes mostly range from 0.80 and above as shown by their red color in **Figure 4.4b**. The areas of lower kurtosis can be found around specular reflectance; however, the kurtosis is generally higher in the non-pregnant sample as compared to the pregnant sample. This is reflected in the 30 percentile difference in the KI value between the two samples. KI was calculated as the ratio between the subsections with kurtosis above 0.6, indicating a strong alignment, and the total number of subsections of the cervix. The single frame shown at 0° itself shows a large discrepancy in the areas with a kurtosis over 0.6, which indicate a better alignment. This can be seen from the color of the subsections. The blue squares indicate the areas where kurtosis exceeds 0.6 as compared to the red squares which are the areas of a low collagen alignment. A comparison of the orientation data between these non-pregnant and pregnant *in-vivo* human cervixes is shown in **Figure 4.5**.

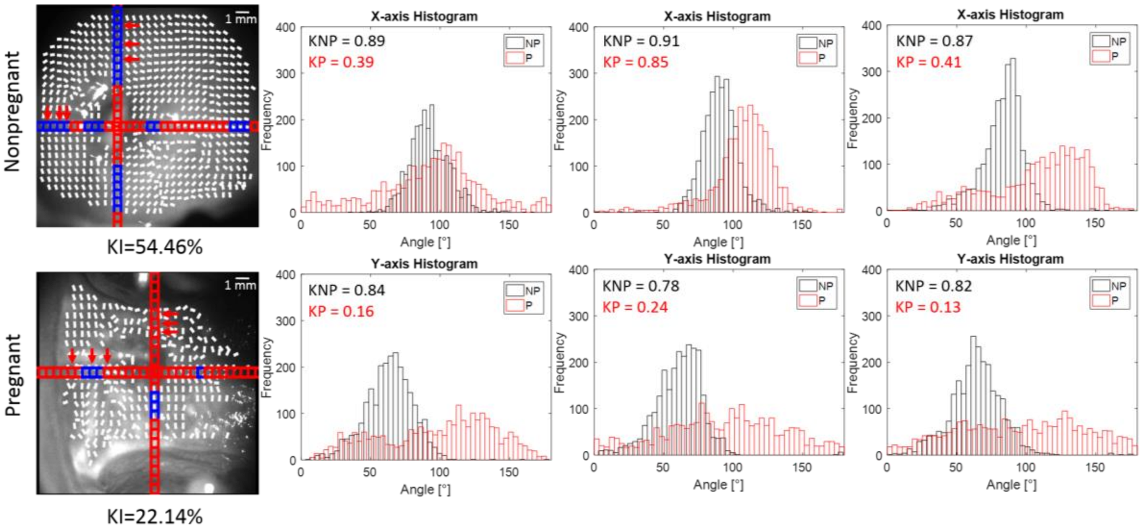

Figure 8.5 *In-vivo* non-pregnant and pregnant human cervixes. The arrows in the grayscale image indicate the subsections on the histogram. Blue subsections > kurtosis = 0.6 > red subsections. X-axis histograms use the subsections going from the left to the right. Y-axis histograms use the subsections going from the top to the bottom. Kurtosis of non-pregnant sample (KNP); kurtosis of pregnant sample (KP). KI = % of kurtosis values > 0.6 across the entire sample. There is a poorer collagen alignment in the pregnant cervix as compared to the non-pregnant cervix, as shown by a lower kurtosis and a broader distribution of angles.

The arrows in the grayscale image indicate the 50 pixels x 50 pixels sections where the histograms were calculated going from the left to the right and from the top to the bottom for the x and y axis directions, respectively. While the first row of histograms is in the x direction, the second row is in the y direction, as denoted by their titles. In order to visualize how the orientation distributions compare to each other, non-pregnant and pregnant cervix histograms were plotted together in the same regions from the os. The non-pregnant data are in the black color, and the pregnant data are in the red color. In general, the non-pregnant cervix collagen orientation shown in the black color is more aligned with a tighter distribution of angles and fewer outliers shown by the higher kurtosis and smaller tails in the orientation histogram. This difference in kurtosis is congruent with the expectation, as pregnant cervixes should have less collagen fiber alignment over gestation, as well as an increased vascularity, as changes in the cervix occur in preparation to delivery.

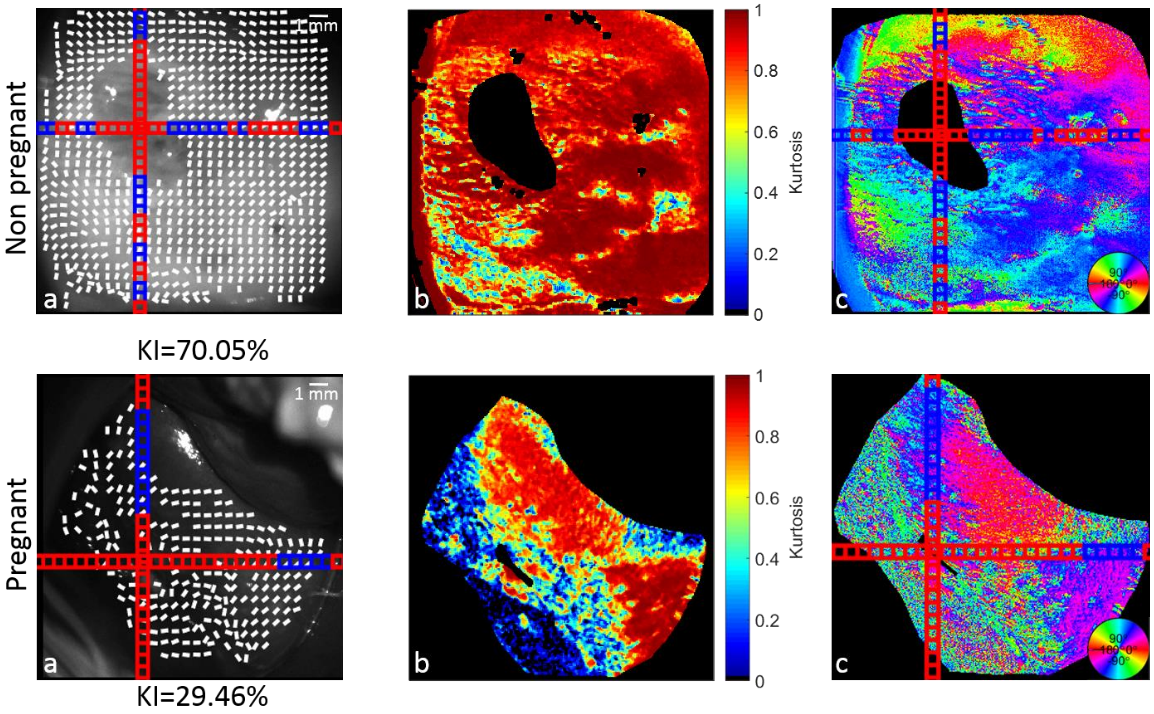

Figure 8.6 *In-vivo* non-pregnant and pregnant human cervixes: a) B/W CCD image w/ orientation lines: Blue subsections > kurtosis = 0.6 > red subsections, b) Kurtosis, c) Mueller matrix decomposed orientation. KI = % of kurtosis values > 0.6 across the entire sample. Circular color bar refers to the retarder orientation calculated from the Mueller matrix of the cervix.

A different set of non-pregnant and pregnant samples can be seen in **Figure 4.6**. Similarly to the set shown in **Figure 4.5**, the areas with specular reflectance were ignored in the calculation of orientation lines, as shown by the gaps in the overlaid lines and the darkened areas in the kurtosis image. Most non-pregnant cervix images show a much higher kurtosis as compared to those of the pregnant sample. This is represented by the 40-percentile difference in kurtosis values above 0.6 between the two samples. Histograms of selected subsections between the non-pregnant and pregnant cervixes shown in **Figure 4.7** provide further evidence in support of the trend of broader distributions of angles in the pregnant cervix that creates a low kurtosis value.

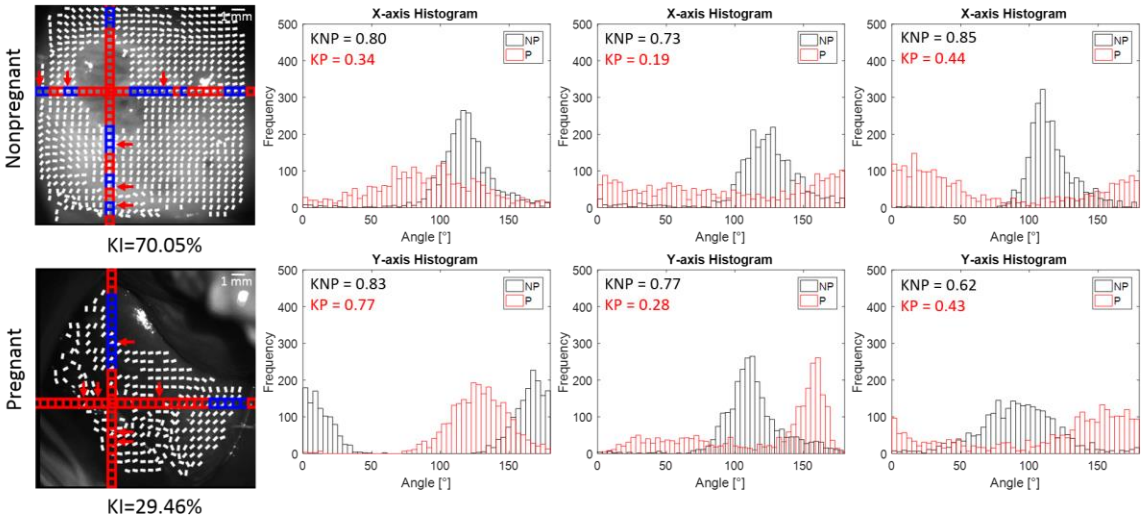

Figure 8.7 *In-vivo* non-pregnant and pregnant human cervixes: The arrows in the grayscale image indicate the subsections on the histogram. Blue subsections > kurtosis = 0.6 > red subsections. X-axis histograms use the subsections going from left to right. Y-axis histograms use the subsections going from top to bottom. Kurtosis of non-pregnant sample (KNP); kurtosis of pregnant sample (KP). KI = % of kurtosis values > 0.6 across the entire sample. There is a poorer collagen alignment in the pregnant cervix compared to the non-pregnant cervix, as shown by a lower kurtosis and a broader distribution of angles.

The results of a one-sided T-test on the kurtosis subsections between the non-pregnant and pregnant cervixes showed that the mean kurtosis of the non-pregnant subjects was significantly higher than that of the pregnant subjects at the significance level of 95%. After disregarding the subsections that were removed due to the applied masks, the sample size of non-pregnant kurtosis subsections was 918 and 918, while that of the pregnant subsections was 882 and 846.

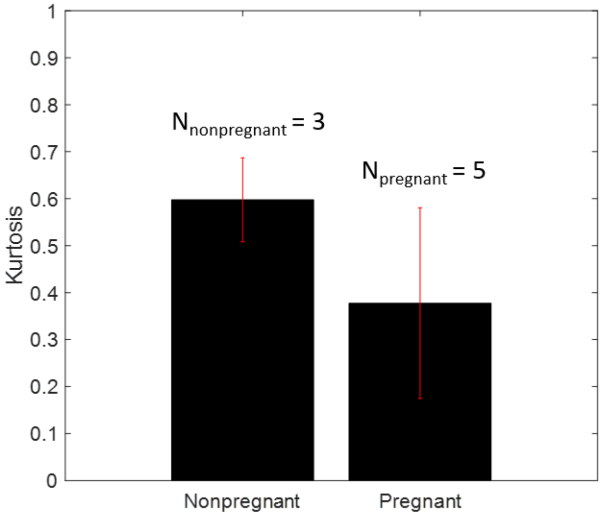

Figure 8.8 Kurtosis mean and standard deviation of non-pregnant (NP) and pregnant (P) cervixes. One sided T-test between both groups showed than mean kurtosis of non-pregnant cervixes was significantly higher than that of pregnant cervixes, with significance level.

The mean and standard deviation of the entire cervixes are presented in **Figure 4.8** and shows a 20-percentile difference in mean between the two categories. The kurtosis standard deviation is also shown to be greater in the pregnant cervixes, likely due to their more randomized arrangement of collagen.

4.4 Conclusion

Optical axis orientation of birefringent materials is essential for the diagnosis of abnormal conditions in tissues with large amounts of ECM. Depending on the application, tissues that rely on collagen for mechanical strength align the protein in various orientations. Unlike OCT that can yield in-depth image-specific cross-sections below the surface of the cervix, MMP thoroughly considers the summation effect of the birefringent material at the surface. Therefore, in the present study, we investigated the changes in collagen circumferentially aligned around the cervix os which makes up a large volume of the cervix and can be investigated non-invasively using MMP. In previous research, this circumferential alignment of collagen was found to begin at the surface and continue deeply into the cervix using MRI.[131] Collagen is important for load bearing in the endocervical canal and can be quickly measured within a set of 16 images needed to create a Mueller matrix. In the present study, on introducing an instrument capable of noninvasively imaging the cervix *in vivo*, we determined the collagen orientation within the cervix using Mueller Matrix decomposition and several filtering steps. The results of the kurtosis analysis showed an increase in collagen ultrastructure disorganization between non-pregnant and pregnant patient samples. One limiting factor when conducting the measurement was the presence of mucus discharge covering a portion of the cervix. An example of this effect is shown in **Figure 4.4**, where a white film can be seen along the bottom edge of the pregnant cervix. These pixels were excluded, as their retardance and orientation values differed considerably for the areas of the uncovered cervix. The use of different incident wavelengths may reduce this artifact and will be explored in future work; in the present study, the cervix was swabbed with a sterile gauze to eliminate the discharge. Further research on collagen orientation in cervixes at different time points during remodeling are needed to better understand if Mueller matrix polarimetry can effectively measure changes in cervical collagen orientation in pregnancy or disease.

4.5 Disclosures

The authors have no relevant financial interests in this article and no potential conflicts of interest to disclose.

4.6 Acknowledgements

We gratefully acknowledge the valuable assistance of all volunteers who participated in this study and the Herbert Wertheim College of Medicine, Florida International University.

CHAPTER 5

[4]Optimization of the incident wavelength for Mueller matrix imaging of cervical collagen

Joseph Chue-Sang[1], Jessica C. Ramella-Roman[1,2a)]

[1]Department of Biomedical Engineering, Florida International University, Miami, FL, USA, 33178
[2]Herbert Wertheim College of Medicine, Florida International University, Miami, FL, USA 33178
a) Author to whom correspondence should be addressed. Electronic mail: jramella@fiu.edu

Abstract:

Mueller matrix polarimetry (MMP) can be utilized to determine optical anisotropy in birefringent materials. Many factors must be optimized to improve the quality of information collected from MMP of biological samples. As part of a study on pre-term birth (PTB) that relied on measurement of the orientation and distribution of collagen in the cervix, an optimal wavelength for MMP to allow more accurate characterization of collagen in cervical tissue was sought. To this end, we developed a multispectral Mueller matrix polarimeter and conducted experiments on e*x-vivo* porcine cervix samples preserved in paraffin. The Mueller matrices obtained with this system were decomposed to generate orientation and retardation images. Initial findings indicate that wavelengths below 560 nm offer a more accurate characterization of collagen anisotropy in the porcine cervix.

Keywords: anisotropy, birefringence, collagen, polarized light imaging, Mueller matrix, cervix, colposcopy

---

[4] This chapter was published as a SPIE Photonics West 2018 proceeding. 10.1117/12.2290766

5.1 Introduction

Early identification of at-risk pregnancies is important for successful medical intervention. Recently cervical collagen orientation has been proposed as a discriminant for preterm labor [75, 76, 205]. We have developed a **PReterm IMaging (PRIM)** system based on a standard colposcope. This system offers high sensitivity to the collagenous cervical ultrastructure through a polarization-sensitive imaging modality known as Mueller matrix polarimetry. Due to its high birefringence, a wavelength-dependent property, collagen is the primary cervical constituent PRIM detects to calculate orientation. PRIM was tested on excised porcine cervixes before being used *in vivo* to examine the cervixes of non-pregnant and pregnant human participants using a 565-nm Light Emitting Diode (LED) source. In an effort to optimize the system, we developed a benchtop multispectral Mueller matrix polarimeter to evaluate the differences in orientation contrast due to illumination wavelength.

5.2 Materials and Methods

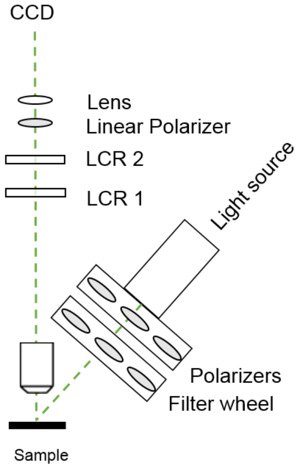

Figure 11.1 Schematic of the multispectral Mueller matrix polarimeter. Liquid crystal retarder (LCR), Illumination port (IP).

The multispectral Mueller matrix system, a modification of an MMP used in previous work [91], is shown in **Figure 5.1**. A CCD camera (DCC3260M, Thorlabs, Newton, NJ) with a Computar MLH-10X 1/2-inch 13-130mm f5.6 10X Macro Zoom lens attached, was secured above the sample objective to allow focusing on the adjustable stage. The MMP offers a field of view of 1.2 cm and a resolution of 10.9 μm/pixel using the sample objective. A linear polarizer (Prinz, Northbrook, IL) and two liquid crystal retarders (LCR) (Meadowlark Optics, Frederick, CO) between the lens and sample objective form the polarization state analyzer (PSA) of the polarimeter. A 150-watt white lamp (LRL-410K, Leeds, Minneapolis, MN) was used as the illumination source and was oriented to illuminate the sample at an incident angle of 45° with a metal-sheathed fiber optic cable. It was collimated with a 30-mm-diameter tube and a 25-mm-diameter plano-convex lens (Newport, Irvine, CA). The four different polarization states required for the Mueller matrix polarization state generator (PSG) were created using a motorized filter wheel (FW103, Thorlabs, Newton, NJ) with three linear polarizers mounted at 0°, 45°, and 90° with the PSA polarizer and a circular polarizer. These four different states were then used to calculate the Mueller matrix of the sample. A second filter wheel mounted after the PSG contained 500-nm, 550-nm, 600-nm, and 650-nm center wavelength bandpass filters, each with 10-nm bandwidth. This second filter wheel allowed easy transition between different spectra while imaging. MATLAB (Mathworks, Natick, MA) was used to control the devices and analyze the data.

The polarimeter was calibrated at each wavelength using a previously published method [53]. **Figure 5.2** shows the Stokes vector results of the calibrations for each wavelength; each plot's horizontal axis represents the orientation of a linear polarizer as it was rotated and imaged by the polarimeter. Each element of the Stokes vectors has a standard deviation of less than 1.0 between all wavelengths, showing that the MMP was properly calibrated and provided similar results at each wavelength.

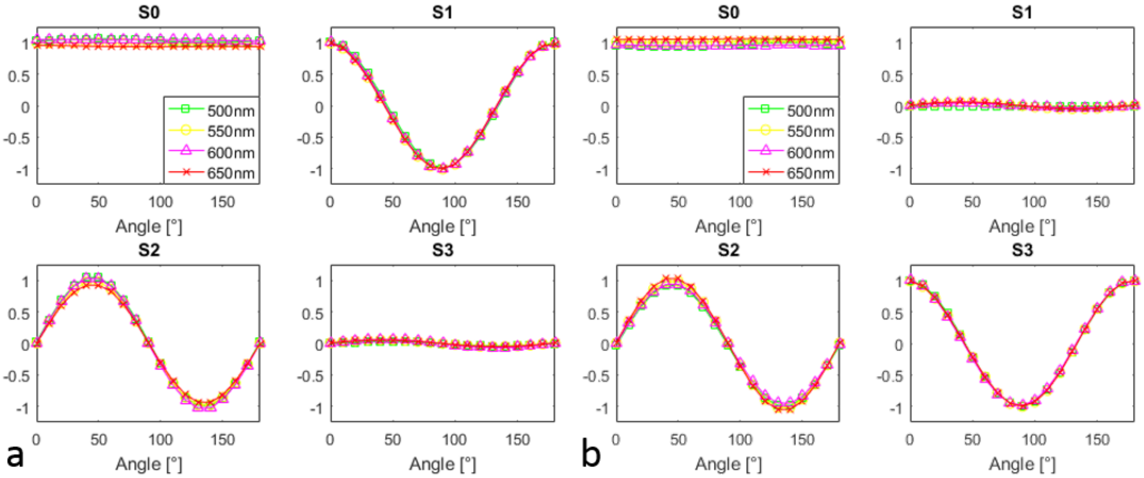

Figure 11.2 Stokes vectors calculated from polarimeter calibrations at four different wavelengths as a sample linear polarizer is rotated: a) linear polarizer alone, b) quarter wave plate in-line after linear polarizer.

5.2.1 Mueller matrix decomposition

Mueller matrix decomposition extracts constituent polarization properties from a Mueller matrix of any complex system [19,56]. The decomposition of the Mueller matrix (M) as proposed by Lu-Chipman [57] yields three canonical matrices accounting for material depolarization (M_Δ), retardance due to linear birefringence and optical activity (M_R), and diattenuation (M_D).

$$M = M_\Delta M_R M_D \tag{5.1}$$

The focus of this study was retarder fast axis orientation θ, as derived by Ma *et al.* [178], which corresponds to collagen bundle orientation in the tissue. We utilized circular statistics [189, 190] to represent data on a unit circle rather than using the arithmetic mean. Since certain angles are equivalent to each other, i.e. 10° is synonymous with 190° or -170° based on direction of rotation, the periodicity of orientation angles requires a departure from arithmetic statistics, which misrepresent the mean of a region. Directional parameters were calculated by applying circular statistical methods to the orientation data decomposed from the Mueller matrix. This method required that data first be transformed into unit vectors with two dimensions, as shown in **Equation 4.2**. **Equation 4.3** is the mean resultant vector $\bar{r}$ of the data set. The mean angular direction $\bar{\alpha}$ can be calculated using the four-quadrant inverse tangent of $\bar{r}$.

$$r_i = \begin{pmatrix} \cos\theta_i \\ \sin\theta_i \end{pmatrix} \tag{4.2}$$

$$\bar{r} = \frac{1}{N}\sum_i r_i \tag{4.3}$$

Circular kurtosis was used as a measure of alignment of collagen bundles detected by the MMP with different wavelengths of light. Kurtosis describes the number of outliers in a set of directional data [189, 191], and is associated with the weight of tails in a distribution. A narrow distribution of angles with small tails corresponds with high alignment and results in kurtosis approaching 1, while a distribution dominated by its tails shows more randomness and an unaligned distribution and will result in kurtosis approaching 0.

5.2.2 Anisotropic test samples

Two test samples were used to verify the efficacy of the multispectral MMP's orientation measurements. An extruded polymer phantom with low scattering and absorption was chosen to obtain a highly aligned measure of orientation as a benchmark; this benchmark served to check if the polarimeter could correctly identify changes in a sample with a known retarder axis. *Ex-vivo* porcine cervix samples—well-characterized and used in previous studies [91, 206, 207]—were imaged using the MMP to compare orientation data between the four wavelengths.

5.3 Results and Discussion

An orientation of 0° is parallel to the horizontal axis and a change in angle counterclockwise from horizontal is considered positive $\Delta\theta$. Grayscale images of the polymer phantom at two different orientations can be seen in **Figure 5.3**; the top row shows the sample at a 60° and the bottom row a 160° orientation; lines representing the average orientation within of sections of the image are overlaid on each. All orientation data displayed were obtained through a 5 x 5-pixel median filter.

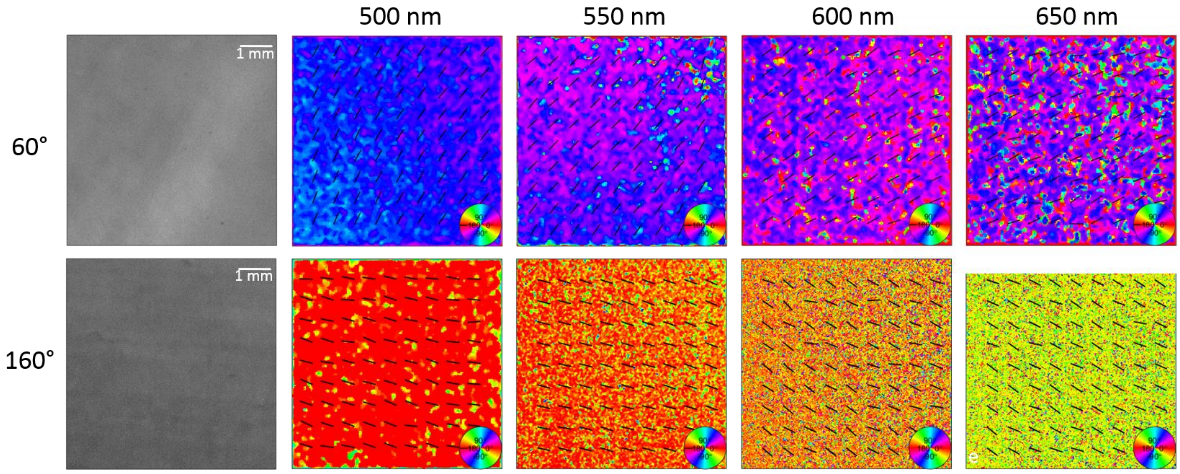

Figure 11.3 Mueller matrix retarder axis orientation for the polymer phantom. Top row: 60°-oriented phantom, Bottom row: 160°-oriented phantom.

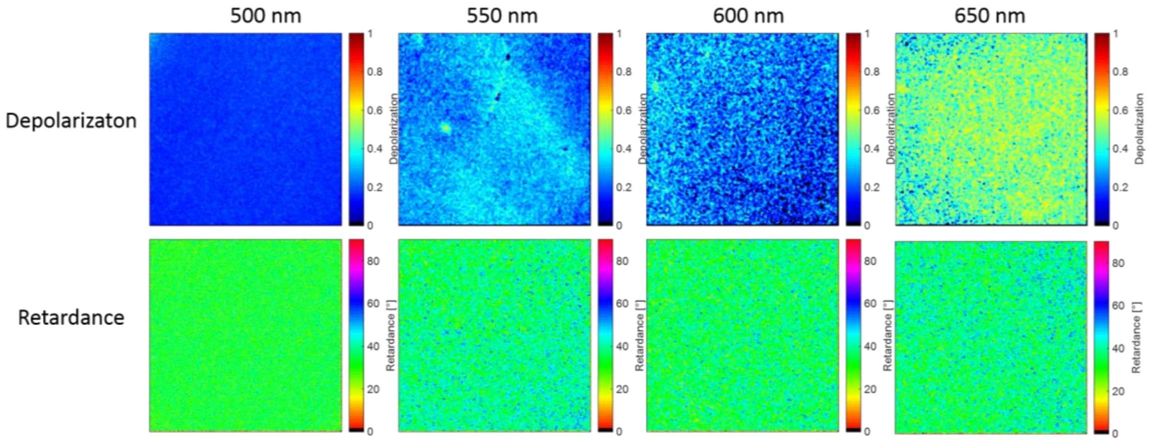

Figure 11.4 Mueller matrix depolarization (top) and retardance (bottom) for the polymer phantom.

The variance of the orientation calculated from the Mueller matrices of the phantom increased as longer wavelengths of incident light were used. This can be seen in the increase in the amount of colors displayed in **Figure 5.3** and the decrease in kurtosis in **Figure 5.5**.

Kurtosis was calculated using a traveling 5 x 5-pixel window across the orientation data. The kurtosis index (KI) shown is a ratio of the total number of pixels in the image to the number that have a kurtosis greater than 0.6. A high KI means there is little variance in the orientation, that the sample is highly aligned. As wavelength increased there was an increase in the variance in the distribution of orientation. A possible explanation for this may be illustrated in **Figure 5.4**; there is an increase in depolarization as incident wavelength increases. This is likely due to the increased optical length in the sample, which causes more scattering and thus greater depolarization.

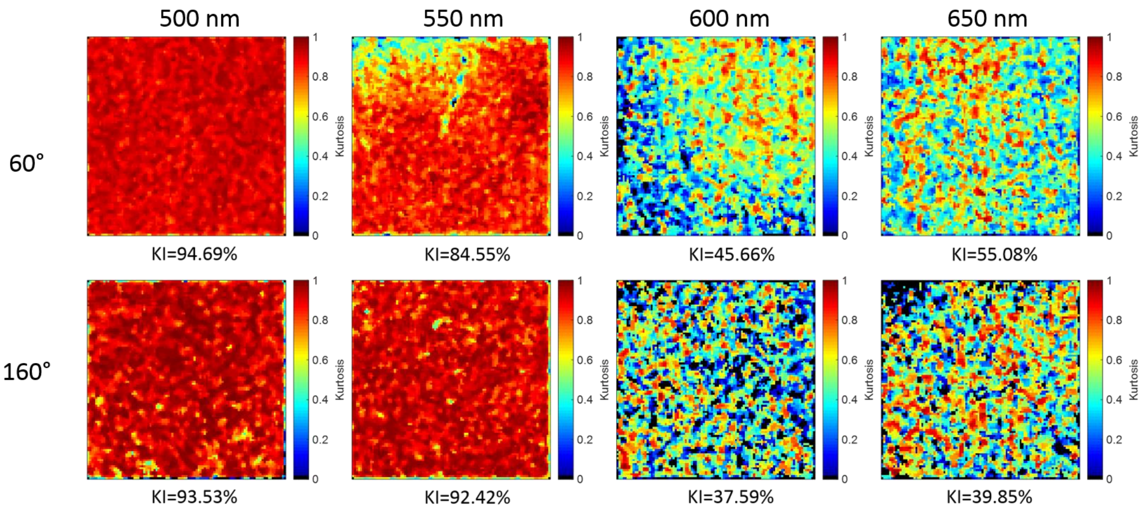

Figure 11.5 Images of kurtosis for the polymer phantom. Top row: (60°-oriented phantom), Bottom row (160°-oriented phantom). (KI = % of kurtosis values > 0.6).

These observations are corroborated by the mean and standard deviation of the orientation data (**Figure 5.6**). The longer wavelengths show an increase in standard deviation, and an increase in the difference between the orientation mean calculated compared to the polymer phantom's actual orientation.

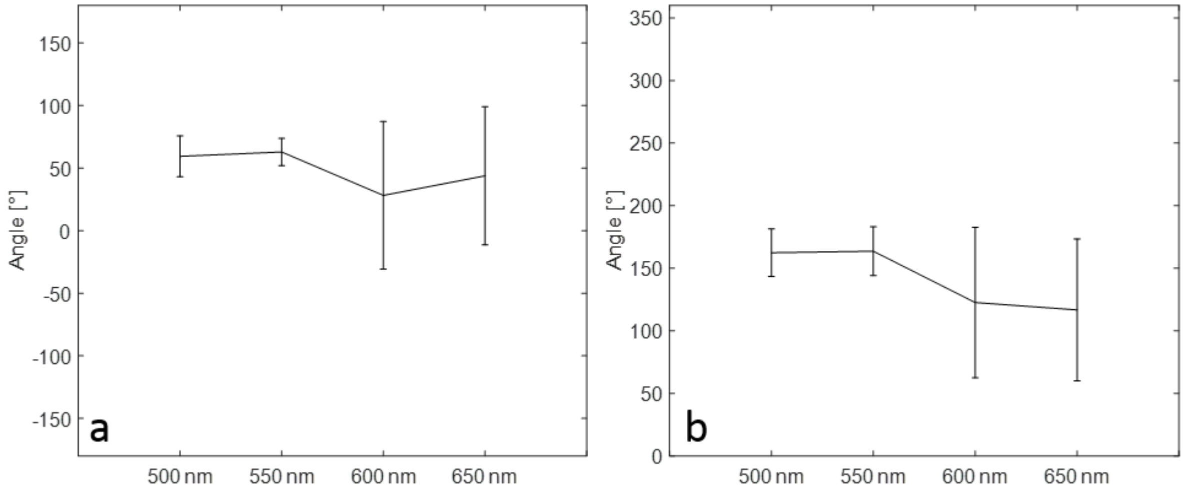

Figure 11.6 Polymer phantom mean angle and standard deviation: a) 60°-oriented phantom, b) 160°-oriented phantom. Data points represent the mean orientation angle, errors bars represent one standard deviation.

After imaging the weakly scattering polymer phantom, excised cervixes were imaged with the multispectral MMP. It was expected that a similar trend would appear, that longer wavelengths of incident light would result in orientation data with greater variance and thus less kurtosis. This can be seen in **Figure 5.7**, where, as expected, longer wavelengths lead to increased variability in orientation and less contrast in orientation as it rotated around the cervix. This is due to the increased noise in pixels averaging out to the same value, while the smaller variance in the lower wavelengths allowed for a much more gradual change in average angle, as would be expected in a structure like the cervix, in which collagen rotates circumferentially.

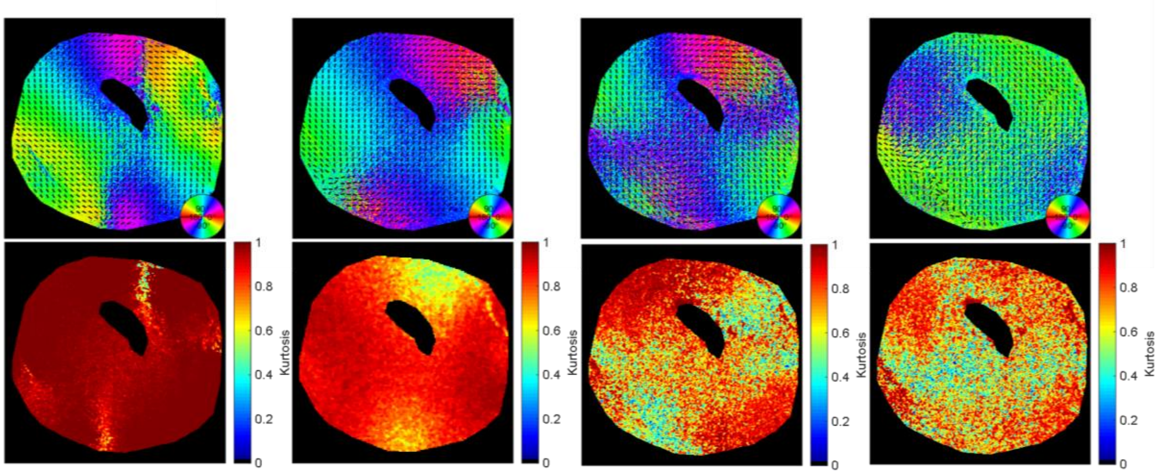

Figure 11.7 Mueller matrix retarder axis orientation and kurtosis in an *ex-vivo* cervix (KI = % of kurtosis values > 0.6).

The same trend in depolarization that occurred in the polymer phantom also occurred with the cervical tissue samples (**Figure 5.8**). Depolarization is inherently greater in this sample due to biological tissue being a highly scattering media.

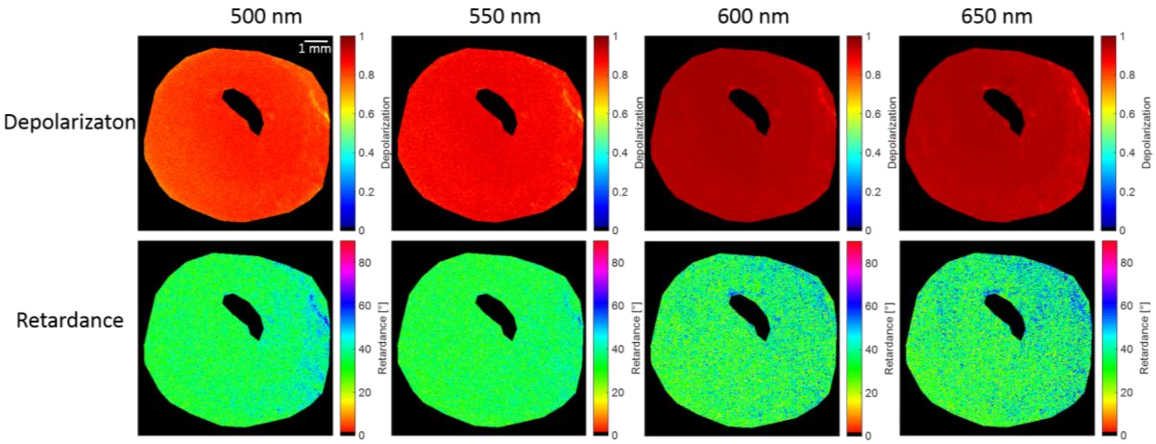

Figure 11.8 Mueller matrix depolarization (top) and retardance (bottom) in an *ex-vivo* cervix.

A second excised cervix exhibited the same trends in multispectral polarimetry (**Figures 5.9** and **5.10**). The mean and standard deviation of kurtosis for this sample is plotted in **Figure 5.11**. Kurtosis was plotted rather than orientation due to the circumferential arrangement of collagen in the cervix. Ideally all angles should be represented as the collagen rotates around the cervical opening (os), causing mean orientation to shift. As a measure of alignment, kurtosis can characterize the shift in orientation around the entire cervix.

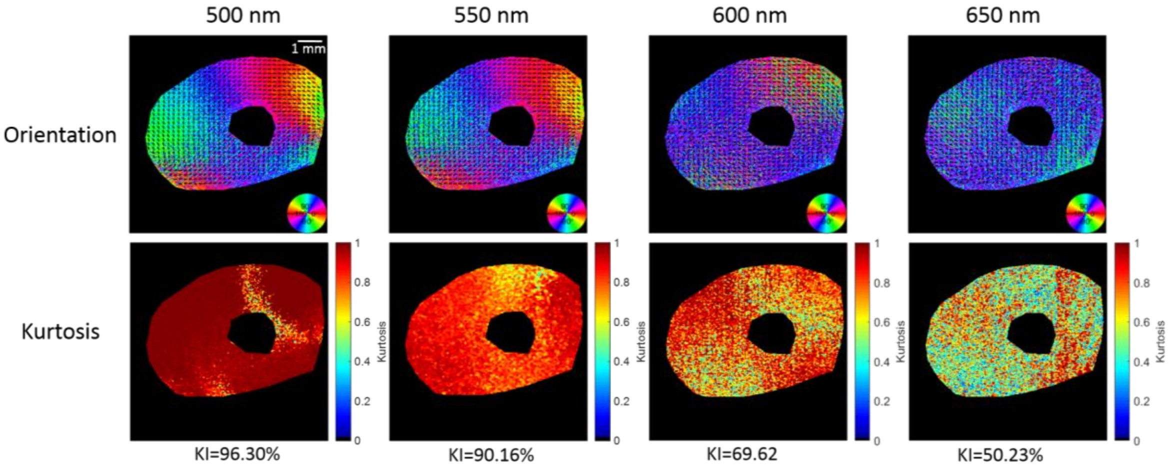

Figure 11.9 Mueller matrix retarder axis orientation and kurtosis in an *ex-vivo* cervix (KI = % of kurtosis values > 0.6).

High contrast in orientation shift will lead to high kurtosis, whereas a more abrupt shift in orientation will lead to low kurtosis in those areas. This result is shown by the lower mean and higher standard deviation of kurtosis at longer wavelengths shown in **Figure 11**.

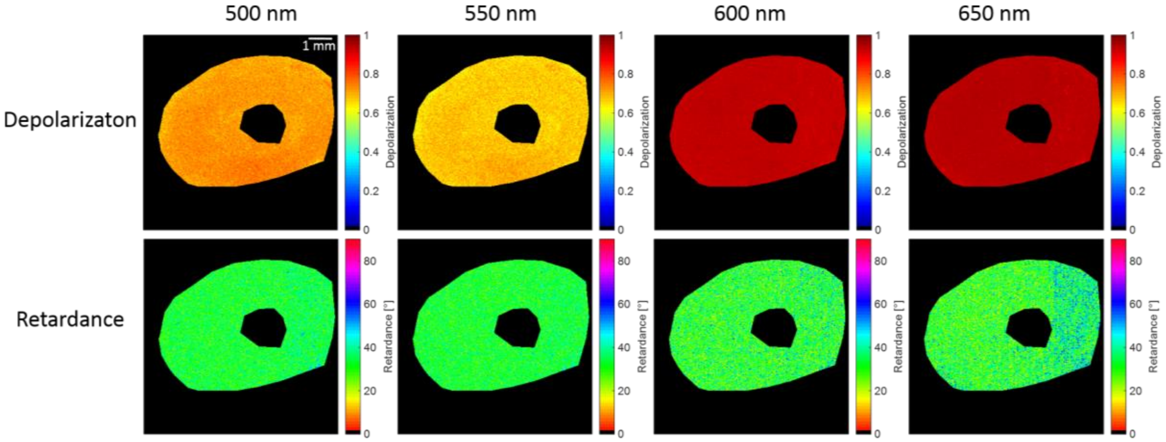

Figure 11.10 Mueller matrix depolarization and retardance in an *ex-vivo* cervix.

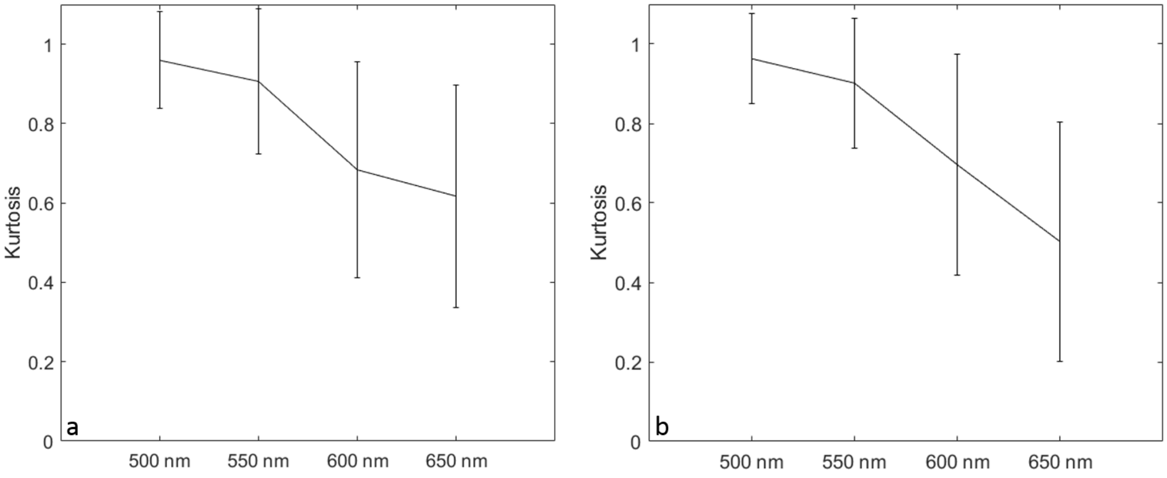

Figure 11.11 Mean kurtosis for *ex-vivo* cervixes; error bars represent one standard deviation. a) Sample shown in Fig. 5.7, b) Sample shown in Fig. 5.9.

5.4 Conclusion

Biological structures with strong retarder properties are highly birefringent, a property that varies with the wavelength of light. Initial findings suggested that wavelengths below 560 nm offered a more accurate characterization of collagen anisotropy in the cervix. To better understand the wavelength dependency of retarder axis orientation in the collagenous tissue of the cervix, a multispectral Mueller matrix polarimeter (MMP) was constructed. This represented part of an effort to improve an ongoing clinical study using an MMP-modified colposcope. It was observed that the variance in retarder axis orientation calculated using Mueller matrix polarimetry increased with an increase in the wavelength of incident light. These observations were obtained by imaging a weakly scattering polymer phantom and excised porcine cervixes. Kurtosis was used as another measure of variance in the orientation data due to its ability to measure the number of outliers in a distribution; low kurtosis denotes a random distribution. As orientation variance increased, kurtosis decreased, and as a result smaller mean orientation angles were calculated compared to the known retarder axis of the polymer phantom. There was also an increase in depolarization as incident wavelength increased. Based on these trends, wavelengths below 560-nm were most effective in characterizing collagen anisotropy in the cervix.

5.5 Acknowledgements

We gratefully acknowledge the Herbert Wertheim School of Medicine, Florida International University and all volunteers who participated in this study.

CHAPTER 6

[5]Optical Phantoms for Biomedical Polarimetry

Joseph Chue-Sang[a], Mariacarla Gonzalez[a], Angie Pierre[a], Megan Laughrey[b], Ilyas Saytashev[b], Tatiana Novikova[c], Jessica C. Ramella-Roman[a,b]

[a]Florida International University, Department of Biomedical Engineering, Miami, Florida, United States
[b]Florida International University, Herbert Wertheim College of Medicine, Miami, Florida, United States
[c]LPICM Laboratoire de Physique des Interfaces et Couches Minces, CNRS, Ecole Polytechnique, 91128 Palaiseau, France

Abstract:

Calibration, quantification, and standardization of the polarimetric instrumentation, as well as interpretation and understanding of the obtained data, require the development and use of well-calibrated phantoms and standards. We have reviewed the status of tissue phantoms for a variety of applications in polarimetry, more than 500 papers are considered. We have divided the phantoms into five groups according to their origin (biological/nonbiological) and fundamental polarimetric properties of retardation, depolarization, and diattenuation. We found that while biological media is generally depolarizing, retarding, and deattenuating, only one of all the phantoms reviewed incorporated all these properties, and few considered at least combined retardation and depolarization. Samples derived from biological tissue, such as tendon and muscle, remain extremely popular to quickly ascertain a polarimetric system but do not provide quantifiable results aside from relative direction of their principal optical axis. Microspheres suspensions are the most utilized phantoms for depolarization and combined with theoretical models can offer true quantification of

---

[5] This chapter was accepted for publication by the Journal of Biomedical Optics (March 2019). 10.1117/1.JBO.24.3.030901

depolarization or degree of polarization. There is a real paucity of birefringent phantoms despite the retardance being one of the most interesting parameters measurable with polarization techniques. Therefore, future work should be directed at generating truly reliable and repeatable phantoms for this metric determination. Diattenuating phantoms are rare and application-specific. Given that diattenuation is considered to be low in most biological tissues, the lack of such phantoms is seen as less problematic. The heterogeneity of the phantoms reviewed points to a critical need of this field for standardization. Ultimately, all research groups involved in polarimetric studies and instruments development would benefit from sharing a limited set of standardized polarimetric phantoms as is done earlier in the round robin investigations in ellipsometry.

Keywords: Polarization, scattering, anisotropy, tissue phantoms, retardation, depolarization, diattenuation

6.1 Introduction

The use of polarized light in clinical and preclinical applications is expanding and several recent reviews by Tuchin [208], Ghosh and Vitkin [2], Qi [209], de Boer [210] and Baumann [211] have illustrated the fast progress of this approach in the medical field.

As polarimetric techniques reach the clinical and commercial stage there is a need to validate them with replicative systems that could serve as biological proxies and mimic the characteristic trends of typical biological observations. Over the past several decades, a variety of such systems—commonly referred to as phantoms—have been implemented for the use of general optical imaging and sensing, Pogue *et al.* illustrated these tools in an exhaustive review[212]. Here we focus uniquely on phantoms used for polarimetry in biomedicine; these phantoms were not included in previous reviews and are relevant for scientists and engineers working on polarimetric applications.

Three dominant mechanisms influence polarized light as it travels through a biological media: depolarization, retardation, and diattenuation. Scattering is a primary contributor to the process of depolarization. Loss of polarization is mainly due to the disarrayed changes of amplitude and phases of the scattered electromagnetic field reaching a detector [213].

Scattering is generally very high in biological media due to the high density and large variety of sub- and extracellular components (such as organelles, nuclei, collagen fiber bundles, cell membrane, to name a few). Different polarization states of incident radiation—linear, circular or elliptical—depolarize at different rates. As for the mathematical representation of depolarization, its theoretical premise is generally supported by the Mueller matrix of an intrinsic (or diagonal) depolarizer (Eq.(1a)) satisfying the covariance conditions (Eq.1b). [214]

$$M_\Delta = d_0\begin{pmatrix}\mathbf{1} & \mathbf{0} & \mathbf{0} & \mathbf{0}\\ \mathbf{0} & \boldsymbol{a} & \mathbf{0} & \mathbf{0}\\ \mathbf{0} & \mathbf{0} & \boldsymbol{b} & \mathbf{0}\\ \mathbf{0} & \mathbf{0} & \mathbf{0} & \boldsymbol{c}\end{pmatrix}, \mathbf{0} < d_0 < 1, |\boldsymbol{a}|, |\boldsymbol{b}|, |\boldsymbol{c}| \le \mathbf{1} \quad (1a)$$

$$-\boldsymbol{a}-\boldsymbol{b}-\boldsymbol{c} \le \mathbf{1}, \qquad -\boldsymbol{a}+\boldsymbol{b}+\boldsymbol{c} \le \mathbf{1}, \quad \boldsymbol{a}-\boldsymbol{b}+\boldsymbol{c} \le \mathbf{1}, \quad \boldsymbol{a}+\boldsymbol{b}-\boldsymbol{c} \le \mathbf{1} \quad (1b)$$

It follows from Eq(1a), that $1-|a|\ and\ 1-|b|$ represent the linear depolarization power (horizontal-vertical and ±45° frameworks). Similarly, $1-|c|$ specifies the power of circular depolarization.

From this, the total depolarization power Δ can be calculated using Eq. (2).

$$\Delta = 1 - \frac{|a|+|b|+|c|}{3} = 1 - \frac{|tr(\boldsymbol{M}_\Delta)-1|}{3}, 0 \le \Delta \le 1 \qquad (2)$$

In birefringent media light experiences changes in propagation speeds for its different polarization components, which leads to phase differences (also called retardation) between those components. Linear retardation is the phase shift between two orthogonal linear polarization states (for example, 0° and 90°, or +45° and -45°). Circular retardation (also referred to as optical rotation) is the difference in phase between the right and the left circular polarized components of light, which happens due to circular birefringence (optical activity). The Mueller matrix of a linear retarder (see Eq. (3)) depends on its phase difference parameter δ and on the azimuth θ of its fast axis.

$$R = \begin{pmatrix} 1 & 0 & 0 & 0 \\ 0 & cos^2(2\theta) + sin^2(2\theta) cos\delta & sin2\theta cos2\theta(1 - cos\delta) & -sin2\theta sin\delta \\ 0 & sin2\theta cos2\theta(1 - cos\delta) & sin^2(2\theta) + cos^2(2\theta) cos\delta & cos2\theta sin\delta \\ 0 & sin2\theta \, sin\delta & -cos2\theta sin\delta & cos\delta \end{pmatrix} \tag{3}$$

The retardation (δ) property of a uniaxial medium is frequently expressed through its birefringence and can be written as shown in Eq. (4), where n_e and n_o are extraordinary and ordinary refractive indices of a birefringent material, d is the distance travelled by light (wavelength λ_0) through the birefringent medium, $\Delta n = n(\theta) - n_o$, where $n(\theta)$ is refractive index seen by the photon propagating in the direction $\boldsymbol{u}(u_x, u_y, u_z)$. Angle θ is the angle between the direction $\boldsymbol{u}$ and extraordinary axis of birefringent material defined as $\boldsymbol{e}(\cos\eta\,, \sin\eta\;, 0)$.

$$\delta = \frac{2\pi d \Delta n}{\lambda} \tag{4}$$

$$n(\theta) = \frac{n_o n_e}{(n_e^2 \cos^2\theta + n_o^2 \sin^2\theta)^{0.5}} \tag{5}$$

$$\theta = \cos^{-1}\left(\frac{u_x \cos\eta + u_y \sin\eta}{\left(u_x^2 + u_y^2 + u_z^2\right)^{0.5}}\right) \tag{6}$$

Birefringence itself can be divided into *intrinsic birefringence* and *form birefringence*.[208] Typically, biological tissues rich in extra cellular matrix (ECM) fibers, for example skin, cornea, sclera, tendon, uterine cervix, and cardiac tissue, exhibit retardation.

Mueller Matrix polarimetry[208, 2, 209] and Polarization Sensitive Optical Coherence tomography (PS-OCT) are techniques capable of quantifying many of the aforementioned parameters of interest. Calculation of the Mueller Matrix requires the modulation of both light source and detector into a minimum of four different polarization states for a total of sixteen measurements. Once the Mueller Matrix is determined it can be decomposed[57] as a sequence of elementary polarization components: a diattenuator, a retarder and a depolarizer. PS-OCT is an extension of OCT, a technique based on low-coherence interferometry that can provide high-resolution cross-sectional imaging of biological tissue and it too can be used to quantify birefringence, diattenuation and depolarization index, a parameter related to depolarization.

Diattenuation, also called dichroism, is generally considered to have the smallest impact on polarized light propagating in biological media. Diattenuation arises from polarization-selective attenuation of the electrical field. Related to diattenuation is the property of optical activity, also known as circular birefringence, which is characterized by the rotation of the polarization plane of linearly polarized light about the axis of propagation.[208] This property is prevalent for chiral molecules such as glucose, proteins, and nucleic acids. [2]

The use of polarimetry in monitoring biological tissue often focuses on quantification of the tissue preferential azimuth (i.e. the orientation of optical axis of uniaxial birefringent medium) related to the arrangement of a collagenous extracellular matrix or other cellular assembly. Skeletal muscle and cardiac tissue are both strongly depolarizing and birefringent due to cellular components and layered structure.

Collagen, animal cornea, retina, and optic nerves have all been shown to have large birefringence and preferential alignment through Polarization Sensitive Optical Coherence Tomography and polarized light microscopy.[204, 215, 216] Several studies using PS-OCT imaging on articular cartilage, which is rich in oriented collagen fibers, have shown changes in collagen retardation in depth.[217-220] Nerves have also been shown to yield retardation with polarization sensitive spectroscopy.[221] Since birefringence is the most common source of retardation and signal for this modality, in general most retardance phantoms can be used as PS-OCT phantoms.

Microtubules made from extracted elements of the porcine brain and axonemes prepared from sea urchin have been examined using polarized light microscopy, where fibers can be visualized.[222] The ECM of the cervix is composed of about 70% collagen and, therefore, has shown to have a significant retardation. Chue-Sang *et al.* used Mueller matrix polarimetry to calculate retardance, depolarization, and collagen fiber azimuth of *ex-vivo* porcine cervix samples (seen in Figure 1).[223] De Martino *et al*. used wide-field multi-wavelength Mueller matrix polarimeters to image cervical neoplasia and colon cancer.[18, 19, 33-39]

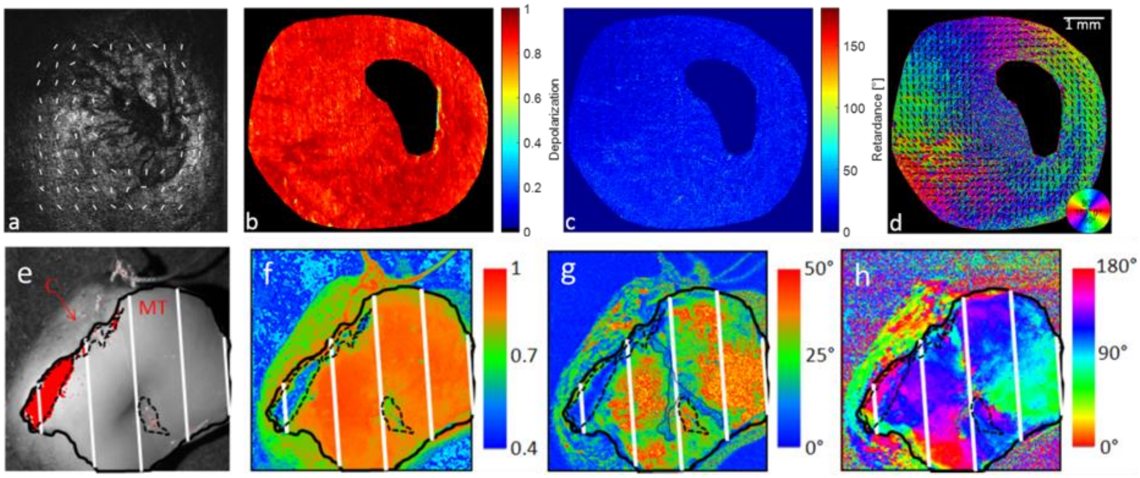

Figure 13.1 Mueller matrix derived parameters (Lu-Chipman decomposition[57]) of an *ex-vivo* porcine cervix: (a) CCD image, (b) depolarization power, (c) scalar retardation, and (d) azimuth of optical axis. Darkened area in the center of the image is the cervical os. Overlaid lines are calculated from the mean of subsections of the azimuth depicted by the false color. [223] Mueller matrix derived parameters (Lu-Chipman decomposition) of healthy human cervical specimen: (e) CCD image, (f) depolarization power, (g) scalar retardation, and (h) azimuth of optical axis.[105]

Vitkin *et al*, used Mueller polarimetry to determine the local structural disorders of the bladder [47] and myocardium[48]. Enhancement of superficial structure by eliminating deep penetrating scattered photons is also a common use of polarimetry in medicine. Groner *et al*. [25] used cross-polarization to highlight superficial vascular contrast in intravital microscopy, applying this technique, among others, to study brain perfusion and pancreatic and hepatic microcirculation [25-30].

Polarized light imaging has been used extensively to enhance surface contrast for dermatologic applications [21]. Demarcation of margins of skin cancers, not visible to the naked eye has been conducted by several researchers, starting with setups focusing on linear depolarization to other systems [22-24, 224] utilizing full Stokes vector polarimetry and out-of-plane approaches [32, 225, 226]. The skin stratum corneum has been shown to be highly scattering hence producing strong depolarization[227, 228]. Changes in retardation have been associated with the presence of collagen in the dermis. For this reason scars have a strong response to polarized light as collagen in wounds recombines in the direction of local forces. [226]

6.2 Optical Phantoms

We have categorized all phantoms by their dominant polarization property—namely, depolarization, retardation, diattenuation or optical activity. We have also introduced a separate table for biological tissues used as phantoms. Many phantoms exhibit more than one property, hence they may appear in more than one table, these repeated phantoms are identified by an asterisk (*). The retardation phantoms table includes an *Induced Retardation* column. This column is included to differentiate phantoms which are inherently birefringent due to their structure from phantoms that are mechanically stressed, strained or otherwise manipulated in order to change their birefringence. Many of the phantoms cited in this review have been used by the same investigators in multiple journals, for simplicity we have not cited all the articles using the same phantoms and limited the review to the ones that were substantially different to each other.

6.2.1 Biological phantoms

The construction of polarimetric phantoms is a complex process, hence, biological samples are commonly used in polarization sensitive optical modalities, Table 1. Collagen rich tissues, for example tendons or rat tails, are the most commonly used in polarimetry. As most biological tissues, collagen scatters (and, consequently, depolarizes); more importantly, collagen introduces a phase shift between orthogonal polarization states of incident polarized light[208] due to its strong birefringence. Since many healthy collagen-rich tissues behave as uniaxial birefringent media, the azimuth of optical axis of linear retardation related to collagen alignment can often be measured.[37, 38, 154, 199, 223, 229, 230]

Chicken or cow tendons have been used by many groups [50, 174, 177, 231-234] to validate polarization based optical instruments. Azimuth angle is calculated [16, 50, 165, 166, 174, 177, 185, 231-237] as well as an increase in scalar retardance due to birefringence. Similar to tendon, murine tails also contain collagen fibers which are strongly aligned. Since the azimuth of the collagen fibers preferential orientation can be directly observed, a typical validation test for polarimeters includes positioning a tendon or rat tail at predetermined angles and then measuring samples at different and well-known angular positions.[16, 153, 223]

While muscle tissue can be used for the same purposes as collagen-based phantoms, the interpretation of the results is less straightforward due to the increased cellularity of these tissues[15]. Studies of myocardium muscle[22, 48, 50, 175, 178, 193, 194, 238-240] have been conducted by several investigators showing loss of retardation and local order for infarcted tissue. For this reason, samples of myocardium have been used to validate different polarimetric systems. Ghosh *et al.* used Mueller Matrix decomposition to calculate depolarization, diattenuation, and retardance of fixed rat myocardial tissue.[188]

Heart valve leaflets are another highly collagenous and anisotropic tissue that have been used as a depolarization and retardation phantom.[233] As in previous example the azimuth of collagen fibers preferential orientation can be detected and used for instrument characterization. Changes in depolarization can also be observed by treating the sample with collagenase.[153, 237]

Artificial skin models grown from epidermal keratinocytes forming a multilayered epidermis on top of collagen I hydrogel with dermal fibroblasts have also been used to mimic the interaction of polarized light with the skin.[241] Unstained cuts of fixed skin equivalents of varying thickness (range: 5µm - 30µm) were measured in transmission with Mueller microscopy and the values of retardation and depolarization parameters were extracted using logarithmic decomposition[242] of the measured Mueller matrices. The measurements confirmed parabolic dependence of depolarization and linear dependence of retardation on thickness, as follows from differential Mueller matrix formalism.

Tissue type	**Preparation**	**Polarization property**	**Transmission /Reflectance**	**Ref.**
Axonemes (Sea urchin)	Extraction from sea urchin sperm and purification steps	Retardation	R	222
Bladder (Porcine)	Excised, fresh	Depolarization, Retardation, Diattenuation	R	243
Brain (Porcine)	Phosphate-buffered saline solution (0.02 M)	Depolarization	R	50
Cartilage (Animal)	Excised, fresh	Depolarization, Retardation	R	217-220
Cartilage (Porcine)	Excised, fresh	Retardation, Depolarization, Diattenuation	T	244
Cervix (Porcine)	Fixed in 4% paraformaldehyde and embedded in paraffin	Depolarization, Retardation	R	199
Eye (Cornea)	Excised, fresh	Retardation	R	215, 216
Eye (Optic nerve)	Cryosectioned	Retardation	R	204
Eye (Retina)	Excised, fresh	Retardation	R	216
Fibroblast (Rat)	Suspension	Depolarization	R	41, 245
Heart (myocardium)	Excised, fixed	Depolarization, Retardation	R	48, 178, 193, 238
Heart (Porcine myocardium)	Phosphate-buffered saline solution (0.02 M)	Depolarization	R	50
Heart (Rat myocardium)	10% formalin and cut into 1 mm slices	Retardation, Diattenuation, Depolarization	R	188

Heart (valve leaflet)	Excised, fresh	Depolarization, Retardation	R	153, 237
Heart (Porcine valve)	Excised, fresh	Retardation	R	233, 237
Heart (Porcine aorta)	Excised, fresh	Retardation	R	15
Heart (Bovine right ventricle)	Cut into 2 cm x 2 cm x 1 cm sections	Retardation, Diattenuation	R	169
Heart (Swine right ventricle)	Excised, fresh	Retardation	R	246
Heart (Rabbit right ventricular wall)	3.7% formaldehyde for one day and 20% sucrose solution for an additional two days	Retardation	R	240
Kidney Cortex	Phosphate-buffered saline solution (0.02 M)	Depolarization	R	50
Liver	Phosphate-buffered saline solution (0.02 M)	Depolarization	R	22, 50
Melanin granules	Suspension	Depolarization, Retardation	R	247
Microtubules	Extraction from porcine brain and purification steps	Retardation	R	222
Nerve (Lobster leg)	Excised, fresh	Depolarization, Retardation	R	221
Skeletal muscle	Excised, fresh	Depolarization, Retardation	R	22, 48, 50, 175, 178, 193, 194, 238-240
Skin	In-vivo	Depolarization, Retardation	R	227, 228, 248
Skin (Calf)	Excised, fresh	Retardation	T	249
Skin equivalent model	Fixed and cut into few µm slices	Depolarization, Retardation	T	241
Tail (Rat)	Frozen and thawed	Depolarization, Retardation	R	16
Tendon	Excised, fresh	Depolarization, Retardation	R	50 231 174 232 177, 233 234
Yeast cells	Suspension	Depolarization	R	245

Table 13.1 Biological tissues used as polarization phantoms

6.2.2 Depolarizing phantoms

Several authors have studied the effect of particle size, density, and index of refraction on the polarization of scattered light[250, 251]. As suggested by the results of these studies, the main scatterers in biological tissues are nuclei, organelles, and bulk tissue structures that limit the photon penetration depth and depolarize light travelling through these media[245]. The cell nuclei and organelles are frequently modeled as spherical scattering particles[60] of refractive index varying between 1.33 and 1.47. The components of extracellular matrix, such as collagen and elastin, have been represented by spherical[10] or cylindrical[35] structures.

Work by MacKintosh et al. showed that circular polarization was maintained for longer depths as compared to linearly polarized light in Mie scattering regime (scatterer size ≥ light wavelength in the medium).[252] In one of the relevant studies, Monte Carlo simulations supported this finding by showing that mean penetration depth was approximately 2 mean free paths (MFP) for linearly and 10 MFP for circularly polarized light in Mie scattering regime[251].

Suspensions of microspheres and other small particles are commonly used to create phantoms with scattering properties, Table 2. The amount of scattering can be adjusted depending on the size and concentration of the microspheres based on the Mie scattering theory. On a smaller scale, nanoparticles have also been widely used to create scattering phantoms in Rayleigh scattering regime. These particles can also be embedded in solid host media, such as gels or polymers, to ensure scattering properties of those materials. In addition, India ink, hemoglobin, and dyes are commonly added to influence the absorbing characteristics.

Several studies, such as Antonelli, Rakovic *et al.*, and Cote *et al.*, have used aqueous polystyrene microsphere suspensions as backscattering polarization phantoms.[44, 45, 232] In order to measure the change in scattering (i.e. depolarization power) calculated for different suspensions, microsphere diameter was varied.[22, 34, 44, 45, 245, 253] This class of phantoms has also been shown to depolarize linear polarization less with smaller-diameter microspheres as compared to circular polarization, while, with an increase of the microsphere diameter, circular polarization has been reported to be better preserved as compared to linear polarization.[253]

While purely aqueous mono-dispersed suspensions of microspheres are most commonly used in scattering experiments, intralipid has also been used to create depolarizing phantoms[208, 245]. Intralipid is commonly used as a nutrition supplement and is an emulsion of fatty micelles; therefore, scattering is due to multi-dispersed spherical structures. Aqueous intralipid suspensions with different dilution factors starting at 1:500 to 1:1 have been used to test depolarization with reflectance polarimetry.[9, 245, 248] An example of such experiment can be seen in Figure 2 where loss of elliptical polarization is measured as a function of depth in an intralipid suspension as reported by Sridhar *et al*. [248] While intralipid suspension exhibits monotonic dependence of depolarization on light wavelength, the use of gold nanoparticles suspended in intralipid creates more complicated depolarization behavior[254]

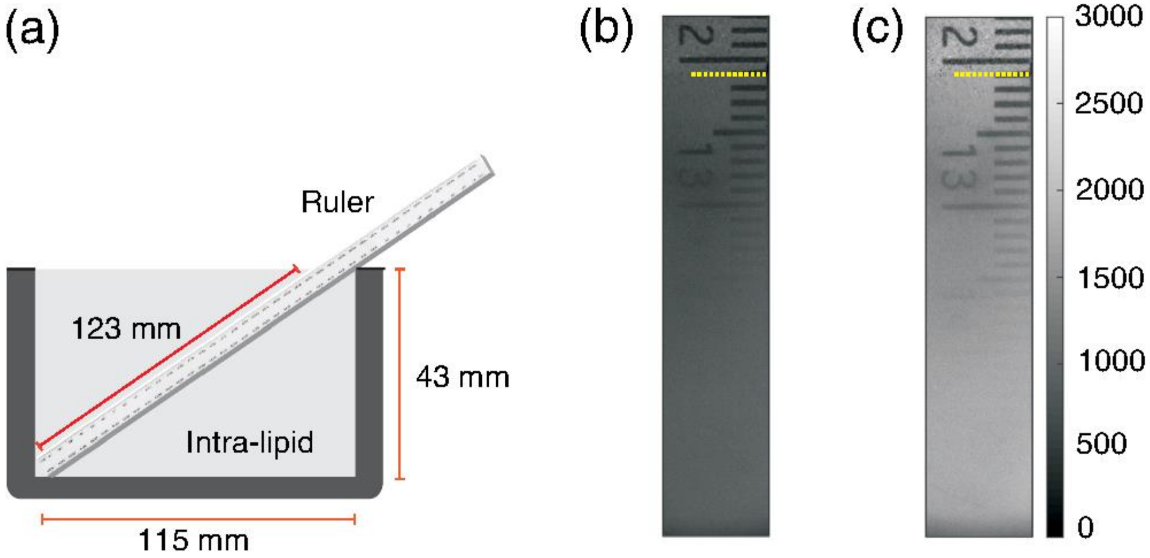

Figure 13.2 Image from reference [248]. (a) ruler placed obliquely in a tank containing Intralipid® solution, (b) elliptical channel image at 45 deg after subtraction method 1, (c) elliptical channel image at 45 deg after subtraction method 2. (b) and (c) have a common colorbar represented at the right edge of the figure. Yellow-dotted line represents the Intralipid®–air interface. Each graduation on the ruler (i.e., 1 mm) corresponds to 0.35 mm in actual depth. Wavelength: 633 nm. Text is from [248]

Titanium dioxide (TiO_2) is another material commonly used to produce scattering in optical phantoms. TiO_2 particles have been used in solid host media, such as polydimethylsiloxane (PDMS) or polyurethane, where, before the curing process, these particles are mixed into the polymer. Adjusting the concentration of TiO_2 makes it possible to change the amount of depolarization.[33,212] Zinc oxide (ZnO) is also commonly mixed into polymers.[255,256] Melanin suspensions of rising concentrations can be used to test depolarization with PS-OCT and model the same phenomenon in the retinal pigmented epithelium. As demonstrated by Baumann *et al*., the change in depolarization based on melanin concentration has a linear relationship with degree of polarization uniformity (DOPU). [247]

Depolarizing agent	**Embedding Material**	**Tissue Mimicking**	**Phantom Thickness**	**Transmission /Reflectance**	**Ref.**
Gold nanoparticles (50 nm)	Intralipid	Contrast agent	Semi-infinite	R	254

Intralipid*	Water, India ink	Bladder wall	Semi-infinite	R	243
Intralipid	Water	Turbid biological media	Semi-infinite	R	9, 245, 248
Intralipid or polystyrene microspheres	Water, Naphthol Green	Porcine liver	1 µm, 1.4 µm	R	49
Kapton tape (Stacked)*	Layered against a rigid base	Theoretical standard	Semi-infinite	R	257
Mylar (biaxially-oriented polyethylene terephthalate)*	Laid against a plexiglass base	Theoretical standard	Semi-infinite	R	257
Polystyrene microspheres	Water	Turbid biological media	Semi-infinite	R	22, 34, 44, 45, 245, 253, 258
Polystyrene microspheres	Intralipid	Turbid biological media	Semi-infinite	R	245 208
Polystyrene microspheres	Polyacrylamide, Sucrose	Turbid biological media	1 cm^3	T	2
Polystyrene microspheres (0.5 µm) and fiber glass*	Polyacrylamide	Anisotropic sample	1x2x4 cm^3	T	259
Polystyrene microspheres and silk fibers*	Water	Anisotropic sample	2.1 cm	R	10, 260
Quartz plate (Wedged)*	None	N/A	3 mm	T	261
Melanin granules*	Water	Retina/Retinal pigment epithelium	Semi-infinite	R	247
Silicon phantom (Extruded)	Air between layers	Anisotropic sample	2 mm	R	199
Silicon (Amorphous)*	None	Theoretical polarization standard	Semi-infinite	R	257
Silicon (Poly-)*	None	Theoretical standard	Semi-infinite	R	257
Silicon grating	Silicon wafer	Theoretical standard	Semi-infinite	R	262

TiO_2 nanoparticles (530 nm)	PVC-based transparent material	Biopsy samples	1 mm	T	33
TiO_2	Wax	Skin	2 mm, 5 mm	R	32
ZnO nanoparticles (340 nm)	PVCP stock solution	Human skin	0.2 mm - 2 mm	T	255 256

Table 13.2 Depolarizing phantoms. *Denotes phantoms that were also tested for other polarization properties in corresponding reference paper.

6.2.3 Retarding Phantoms

Polymer-based materials are a common source of retardation. Due to their molecular structure or preparation process, many polymers possess intrinsic birefringence (i.e. behave as uniaxial crystals).[263] Others can be induced to become birefringent by applying mechanical stress to the material.[2, 20] Many of these polymers are transparent, hence scattering particles such as microspheres can be added to better simulate biological media. Electrospun polymer fibers, fabricated by charging droplets of polymer at high voltages which creates an interconnected network of small fibers [264], were used by Goth *et al.* to determine the degree of anisotropy of the overall structure. [233] The anisotropic biological elements in the extracellular matrix (particularly collagen and elastin) have been simulated with several materials including silk[10, 260] and glass fibers[259, 265]. An example of fibrous phantom is shown in Figure 3. Here the phantom is composed of polystyrene microspheres and well-aligned glass fibers embedded in polyacrylamide (glass fibers have a 10-µm diameter and 1.547 refractive index).

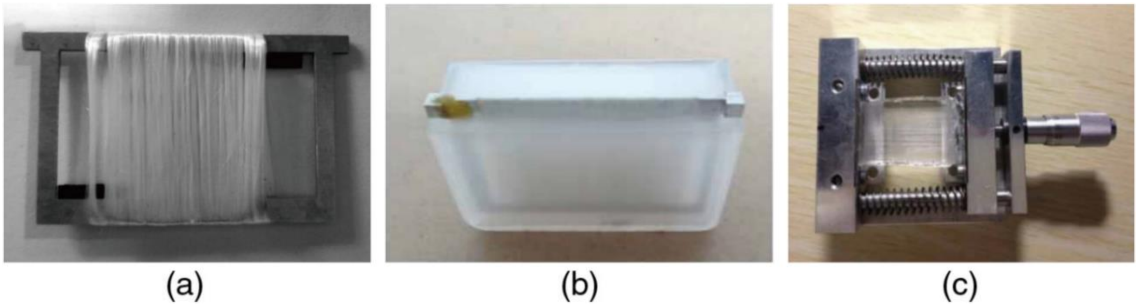

Figure 13.3 Image from reference [265] Figure (a) cylinder model; (b) sphere-cylinder model (SCM); and (c) spherecylinder birefringence model.

Phantoms for PS-OCT require a strong backscattering to generate a high image contrast and have ideally well-defined layers with homogeneous yet different values of birefringence, Table 3. Accordingly, Liu *et al.* have used a phantom consisting of a long birefringent polymer band laid over four smaller bands of differing birefringence. The optical axes of bottom four bands were oriented at 45° with the optical axis of top layer allowing for a depth dependent change in retardation.[266] An example of this retarding phantom is shown in Figure 4.

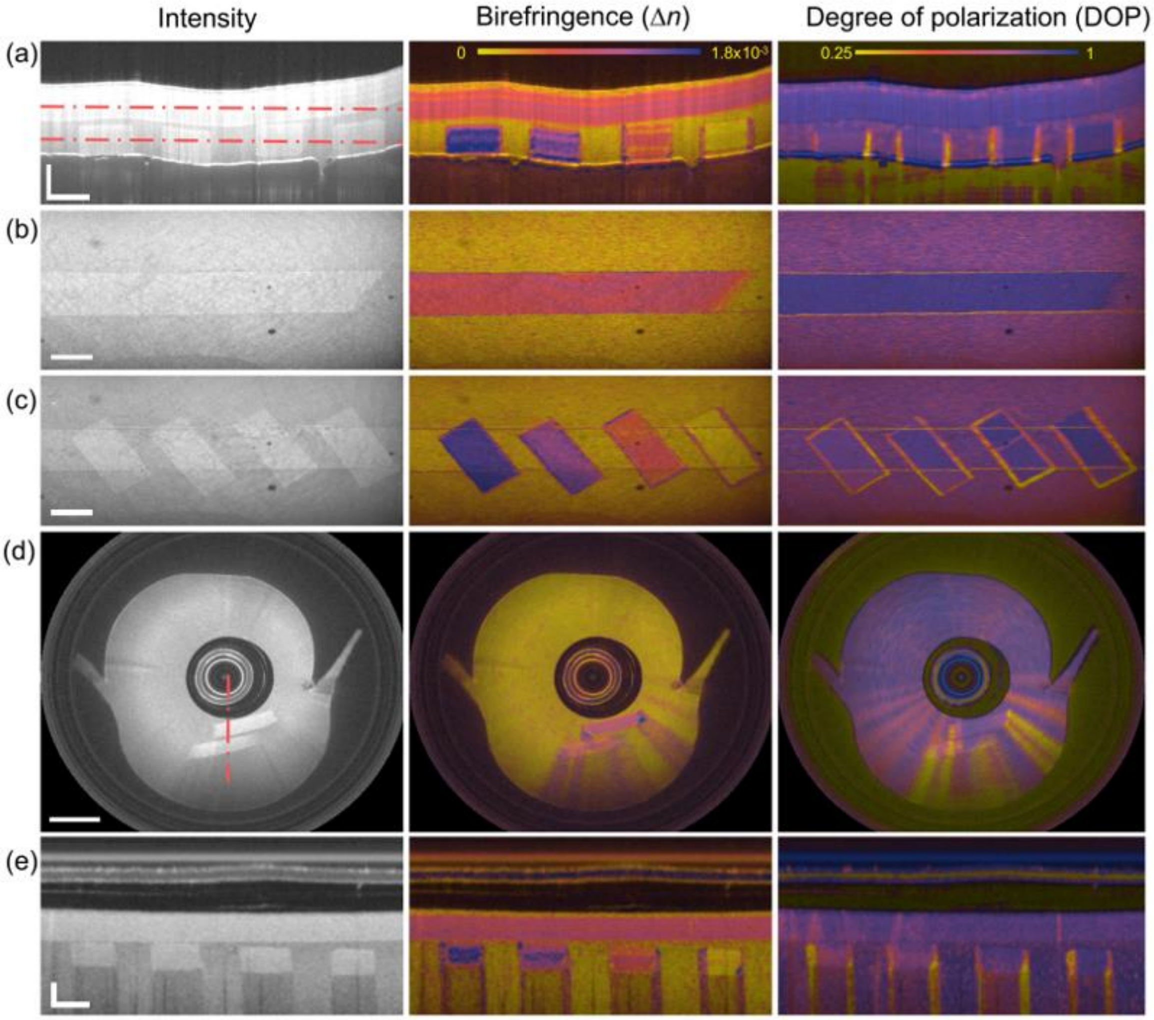

Figure 13.4 Image from reference [266]. Intensity, birefringence and DOP images of the slab (a-c) and cylindrical (d-e) phantoms. (a) Representative cross-sectional images of the birefringence phantom for galvanometer-scanning system. (b) & (c) En-face images at different depths as indicated by the dashed red lines in (a). Horizontal and vertical scale bars for (a-c): 2 mm and 250 μm, respectively. (d) Representative images obtained from one rotational scan with the catheter. Scale bar: 1 mm. (e) Longitudinal sections obtained from a pull-back data set, with its corresponding location indicated by the dashed red line in (d). Radial and horizontal scale bars: 250 μm and 1 mm, respectively. (Text from Liu *et al*. [266])

Ghosh *et al.* induced changes in retardation by stretching a polyacrylamide phantom. Moreover, changing birefringence, and mixing polystyrene microspheres and sucrose into the polymer, produced phantoms that could be used to characterize retardance, depolarization, and diattenuation.[2] [200, 259]. Extruded silicon, silicon wafers with gratings, and other types of silicon (poly and amorphous), as well as different tapes (e.g., Kapton and Mylar) normally used in solar panels, have been used to create phantoms containing different combinations of diattenuation, depolarization, and retardation properties. [199, 257, 262] Figure 5 shows an example of an experimental setup used to induce birefringence in a polymer through mechanical strain by Wood *et al.* [7]

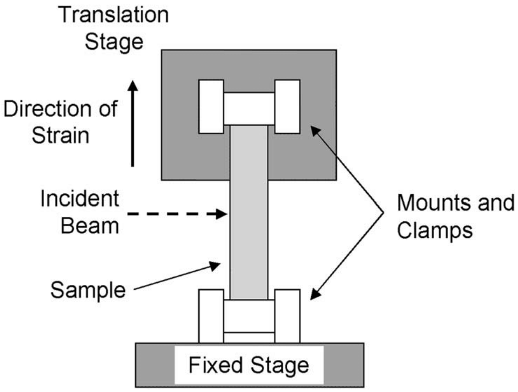

Figure 13.5 Image from reference [7]. Apparatus to create birefringent phantoms.

In order to account for different geometries and extract geometry-independent metrics of anisotropy, retardance measurements have been taken using a 8 mm diameter polystyrene sphere of known anisotropy axis azimuth.[267] Fan *et al.* imaged a plastic cap to determine its retardation with PS-OCT.[234]

Retardation material	**Embedded Material**	**Induced Retardation**	**Tissue Mimicking**	**Phantom Thickness**	**Transmission /Reflectance**	**Ref.**
Birefringent film	Intralipid, India ink	Structure	Extracellular matrix	Semi-infinite	R	243
Electrospun fibers (0.6-1.0 µm)	None	Structure	Heart valve leaflet	Semi-infinite	R	233
Human hair	None	Structure	Human hair	N/A	R	217
Kapton tape (Stacked)	Layered against a rigid base	Structure (layers)	Theoretical standard	Semi-infinite	R	257
Mylar (biaxially-	Laid against a	Structure	Theoretical standard	Semi-infinite	R	257

oriented polyethylene terephthalate)	plexiglass base					
Plastic cap*	None	Structure	Theoretical standard	Semi-infinite	R	[234]
Polycarbonate	None	Longitudinal stretch (heating and cooling)	Turbid biological tissue	250 µm	R	[266]
Polyacrylamide polymer (elastic)	None	4 mm stretch	Turbid biological tissue	4 mm	R	[200]
Polyacrylamide gels	Polystyrene microspheres, 1 M sucrose	Stretching	Turbid biological tissue	1x1x4 cm^3	T	[20]
Polyacrylamide*	Sucrose, polystyrene microspheres	Stretching	Turbid biological tissue	1x1x1 cm^3	T	[2]
Polyacrylamide*	Polystyrene microspheres and well-aligned fiber glass	Stretching (1-5 mm), Birefringence = 0 – 10^{-5}	Turbid biological tissue	1x2x4 cm^3	T	[259], [265]
Polyethylene (Low density)	None	Bending (up to 2.5 MPa)	Turbid biological tissue	1 mm	R	[268]
Polystyrene sphere	None	Structure	Infarcted myocardium	8 mm diameter	T	[267]
Polystyrene microspheres	Water	Structure	Turbid biological media	Semi-infinite	R	[258] [269] [232]
Polyurethane	Particle filled polypropylene	Longitudinal stretch	Theoretical standard	1 mm	R	[270]

Silicon (Extruded)	Air between layers	Structure	Theoretical standard	2 mm	R	199
Silicon (Amorphous)	None	Structure	Theoretical standard	Semi-infinite	R	257
Silicon (Poly-)	None	Structure	Theoretical standard	Semi-infinite	R	257
Silk fibers*	Water	Structure	Anisotropic sample	Semi-infinite	R	10, 260

Table 13.3 Retardation phantoms. The “Induced Retardation” column is for differentiating between phantoms which inherently exhibit their birefringence due to their structure and phantoms that are mechanically stressed, strained or otherwise manipulated in order to change their birefringence. *Denotes phantoms that were also tested for other polarization properties in corresponding reference paper.

6.2.4 Diattenuating Phantoms

The asymmetry of a molecule can result in selective transmission of an incident state of polarized light. Swami *et al.* measured diattenuation as a means to identify the general shape of gold nanoparticles (GNPs)[271], Table 4. Differently shaped GNPs displayed different spectroscopic diattenuation results. Chen *et al*. [272] and Lung *et al*. [273] used a quarter wave plate and a polarizer to test the performance of an analytical model for low diattenuating optical components as they were rotated from 0 to 150° with a step of 30°. Moreover, these authors also used a polymer polarizer baked at 150° C as a sample with both diattenuating and birefringent properties. Chenault and Chipman used a rotating sample polarimeter to find linear diattenuation and retardance of the sample calculated from intensity modulation.[274]

Diattenuation agent	**Solvent/Preparation**	**Tissue mimicking**	**Phantom Thickness**	**Transmission/ Reflectance**	**Ref.**
Gold Nanoparticles (non-spherical shapes)	CTAB-coated GNPs	Theoretical standard	Semi-infinite	T	271
Kapton tape (Stacked)*	Layered against a rigid base	Theoretical standard	Semi-infinite	R	257

Mylar (biaxially-oriented polyethylene terephthalate)*	Laid against a plexiglass base	Theoretical standard	Semi-infinite	R	[257]
Polarizer	None	Theoretical standard	21.59 mm	T	[272, 273]
Polarizer (Baked)	150°C for 80 minutes	Theoretical standard	N/A	T	[272, 273]
Polarizer (Rotating)	None	Theoretical standard	N/A	T	[274]
Quarter wave plate	None	Theoretical standard	N/A	T	[272, 273]
Silicon (Amorphous)*	None	Theoretical standard	Semi-infinite	R	[257]
Silicon (Poly-)*	None	Theoretical standard	Semi-infinite	R	[257]

Table 13.4 Diattenuation phantoms. *Denotes phantoms that were also tested for other polarization properties in corresponding reference paper.

6.2.5 Circular Retardation Phantoms

The measurement of circular birefringence is frequently associated with chiral molecules [275] such as glucose. The aggregation of chiral molecules in media causes the rotation of polarization plane of linearly polarized light as it travels through that volume. Manhas *et al.*, Ortega-Quijano *et al.*, and Ossikovski *et al.* added glucose to a polystyrene microsphere mixture in order to induce chirality and provide optical activity properties to the phantom[258,269,276], Table 5.

Cote et al. developed several ocular models to investigate the feasibility of measuring glucose in the eye aqueous humor with polarization-based techniques [277], Figure 6. The model shown also accounts for the cornea birefringence utilizing a PMMA based phantoms overlaying a chamber mimicking the aqueous humor. A similar approach was used by Rawer [278].

Other intralipid suspension liquid phantoms can be made with absorbers, such as dye, and optically active molecules such as glucose and L-lysine to test optical activity in samples.[46, 220] Antonelli used honey to calculate the optical activity of the sample.[232] Pham *et al.* and Cheng *et al.* studied the concentration of glucose by measuring the optical rotation angle of circular birefringence (optical activity) in human blood plasma and porcine cartilage samples [249].

Figure 13.6 Optical phantom from Malik *et al*. [277] The custom-built ocular model. Glucose concentration in the anterior section is varied through the two infusion tubes.

Optical Activity agent	**Solvent/Preparation**	**Tissue mimicking**	**Phantom Thickness**	**Transmission/ Reflectance**	**Ref.**
Glucose (L-lysine)	Distilled water, β-alanine, intralipid suspension, trypan blue dye	Turbid biological media	Semi-infinite	R	[46]
Glucose (D-)	Water, 2 µm polystyrene microspheres lipofundin blood plasma SiO2 nanoparticles	Turbid biological media	40 mm	R/T	[258] [269] [276] [279] [249] [280]

Glucose	Water	Eye acquous humor	Semi-infinite	R	[277], [278] [281]
Glucose	Water	Eye acquous humor	1x1 cm^2	T	[282]
Honey	None	Turbid biological media	Semi-infinite	R	[232]
Sucrose	Polyacrylamide, polystyrene microspheres	Turbid biological tissue	1x1x1 cm^3	T	[2]
L−(+) - arabinose M. Racemic	Water and polystyrene microspheres	Turbid biological tissue	1x1x1 cm^3	Side T	[275]

Table 13.5 Optical Activity phantoms

6.3 Conclusions

Optical phantoms that can be used for the calibration and benchmarking of polarimetric techniques and for mimicking the optical response of tissues have been used by several investigators.

It is to be noted that polarimetric optical phantoms are often unique to each research group and, aside from tests conducted on depolarization with microspheres suspensions, no standardization has been attempted. To our knowledge only one company offers birefringent phantoms for polarized microscopy (NBS 1963A Birefringent Resolution Target by Thorlabs). As the biomedical applications of polarimetric techniques moves towards quantification of directionality and retardation more standardized phantoms are necessary. The PS-OCT phantoms proposed by Liu et al. [266] are a good example of such approach. The measurements of PS-OCT's two core parameters, namely, retardation and azimuth of optical axis can be easily reproduced, and different instruments can be benchmarked using such standardized phantoms. These mixed properties phantoms, particularly ones that include both depolarization and retardation are needed for many applications. Phantoms that have birefringence of form rather than just intrinsic birefringence are also needed to simulate fibrous tissues such as the cervix, cardiac tissue, or muscle. Nevertheless, the task of creating general use phantoms is complicated by the heterogeneity of tissues, the complexity of polarized light tissue interaction and the strong wavelength dependence of polarization-based techniques.

For these reasons the use of biological tissue as measurement standards is very common in polarimetric applications, but unless these samples are well known or measured with an alternative modality (for example PS-OCT or Second Harmonic Generation) the scientific rigor of these experiments remains limited.

New fabrication modalities such as 3D printing and lithography are becoming available to researchers worldwide, we propose that a collaborative effort in the development of a standardized optical phantom for polarimetry could truly benefit the scientific community.

The future work on the development of standardized optical phantoms for polarimetry should be envisaged to make them available for circulation among the research groups involved in polarimetric research and instruments development for benchmarking their experimental results and calibrating the instruments, as was done earlier in the round robin investigations in ellipsometry.[283]

Disclosures

The authors have no relevant financial interests in this article and no potential conflicts of interest to disclose.

6.4 Acknowledgements

We gratefully acknowledge the support of the Herbert Wertheim Foundation and NSF ERC Grant PATHS-UP EEC-1648451 and STROBE: A National Science Foundation Science & Technology Center under Grant No. DMR 1548924

CHAPTER 7

Conclusions

Polarization-based imaging can be a powerful tool for investigating biological tissues with a high amount of extracellular matrix (ECM). The protein that constitutes the vast majority of the ECM, collagen, can be isolated from the surrounding media using techniques such as polarized light imaging and polarization sensitive optical coherence tomography (PSOCT). For this reason, pathologies characterized by changes in collagen architecture in a tissue are prime targets for study and diagnosis using polarization-based imaging methodologies. These structural changes can include collagen crosslinking and density tied to depolarization and retardation, as well as preferred orientation of collagen fiber alignment. Depolarization, retardation, and preferential orientation can be calculated using Mueller matrix polarimetry by means of a mathematical decomposition and were investigated in this thesis. Decreases in depolarization was measured in Chapter 2 to characterize loss of collagen crosslinking resulting from incubating heart valve leaflets in collagenase. A combined and co-registered PSOCT-MMP was introduced in Chapter 2 and used to image heart valve leaflets and tendon - collagen-rich tissues. Damage of heart valve leaflets with collagenase was corroborated between both modalities with decreases in attenuation coefficient and DOPU found with PSOCT, and decreases depolarization found MMP, which was reported in Figure 2.6. The behavior of these parameters before and after collagenase treatment appeared to relate to the change in attenuation coefficient caused by the decrease in scattering profile of the tissue caused by less collagen crosslinking that was calculated using PSOCT.

In addition, Mueller matrix decomposed depolarization and diattenuation showed changes as tendon was thermally damaged. The typical cyclical retardance pattern of tendon of PSOCT B-scans was disrupted where large changes in depolarization and diattenuation were seen in the more severely burned tendon. The combined approach could potentially be utilized to refine models of retardation, particularly due to many models relying on measuring of the surface retardation as a starting point for the model [168]. Ultimately, this study was important in designing and validate the Mueller Matrix polarimeter that would be used through the rest of this dissertation.

Chapters 3-4 dealt predominantly with investigating the preferred orientation of collagen alignment within the cervix between normal conditions and pregnancy.

Chapter 3 began the investigation into orientation of the optical axis of birefringent material as a possible diagnosis tool for abnormal conditions in collagenous tissues. Typically, load-bearing tissues align collagen and other ECM proteins in preferred orientations for increased strength depending on their purpose.[196] In the cervix, collagen is preferably aligned circumferentially to maintain a strong load-bearing structure as shown by Myers *et al*.[12, 114] The Mueller matrix polarimeter that was used in Chapter 2 was used for this study with the exception of a new camera. The OCT system was also repurposed to replicate a cervical collagen study published by Gan *et al.*[102] that would be used to validate polarimeter. Chapter 3 showed that this complex alignment can be measured with one set of images using Mueller matrix polarimetry. MMP offers advantages over using OCT and SHG to measure collagen alignment due to its ability to capture the entire cervix positioning instrumentation outside the vaginal canal whereas the other two modalities have much shallower working distance as well a limited field of view (~ 1cm for OCT and

1 mm for SHG). This aspect is particularly problematic because imaging of the entire cervix would require multiple acquisitions and the creation of a mosaic in post-processing. The co-registration process of images in three dimensions adds further complications that need to be accounted for. Finally, Mueller Matrix polarimetry can be readily integrated in a colposcope which is routinely used for cervical inspection in the clinical setting, the acceptance and familiarity of this device from the medical personnel is believed to improve the clinical translation of this technique.

Besides, birefringent axis orientation, depolarization and retardation were also decomposed from Mueller matrices. The silicon phantom used to validate the system showed low variation in these parameters due to the small amount of scattering in the sample corroborated by its transparency and low depolarization. The Mueller matrix decomposed orientation was found to be statistically similar to measurements made using optical coherence tomography using circular statistics to calculate kurtosis and mean orientation. Further studies of collagen orientation in cervixes under different conditions are needed to understand if Mueller matrix polarimetry can effectively measure the changes in collagen orientation that should occur when the normal ECM alignment is disrupted by pregnancy or disease. Towards this goal, a preliminary *in-vivo* study of pregnant human cervixes was conducted using a colposcope outfitted with a Mueller matrix polarimeter of the same design as reported here and was discussed in Chapter 4.

The ability to identify the optical axis orientation of birefringent materials is a powerful tool for the diagnosis of abnormal conditions in ECM rich tissues. Past studies using MRI have shown that the circumferential alignment of collagen begins at the surface and continues deeply towards the distal end of the cervix.[131] This suggests that changes in collagen structure at one end of the cervix may be indicative of the other side as the entire cervix ripens towards labor. The modified colposcope introduced in Chapter 4 is capable of noninvasively imaging the cervix *in vivo* and determining the collagen orientation within the cervix using Mueller Matrix decomposition. We have utilized a measurement of the peakedness of the collagen angular orientation distribution to quantify the degree of organization of the local collagen in small regions of interest as well as the entire cervix (kurtosis analysis). The results of the kurtosis analysis showed an increase in collagen ultrastructure disorganization between non-pregnant and pregnant patient samples.

A brief study was also conducted on excised cervix tissue to determine the optimal wavelength for kurtosis analysis in the cervix. To this end a multispectral MMP was constructed. This represented part of an effort to improve the ongoing clinical study using the MMP-modified colposcope reported in Chapter 4. The initial findings suggested that wavelengths between 500-560 nm offered higher signal to noise ratio when representing collagen anisotropy in the cervix. It was observed that the variance in retarder axis orientation calculated using Mueller matrix polarimetry increased as the wavelength of incident light increased in a polymer phantom as well as excised porcine cervixes. The increase in retarder orientation variability was shown in more detail by calculating kurtosis images of the cervixes. These images showed a decrease in kurtosis[alignment] as orientation variance increased and the distribution of orientation values became more random. Curiously, there was also an increase in depolarization as incident wavelength increased. This may be due to the increase in probing depth due to longer wavelengths causing more scattering events and further randomizing the probing polarized light. Based on this, it was decided to continue to use the 560 nm wavelength light source that was currently in use by the Mueller Matrix polarimetry capable colposcope.

Mueller Matrix polarimetry was shown to be capable of discerning fiber axis orientation and alignment *in-vivo*. This was done non-invasively and through one set of images at large (3 cm) field of view, avoiding the use of image mosaicking of other competing optical techniques.

The arrangement of collagen was observed by calculating kurtosis to be statistically different between nonpregnant and pregnant patients using a T-test at the end of the short preliminary colposcopy study using Mueller Matrix polarimetry to diagnosis PTB. Power analysis of the study was also performed to calculate whether the current sample size and standard deviation was satisfactory to return a significant probability that the two populations are different. This was done with alpha = 0.05, and a two-tailed calculation which resulted in an 84.72% probability that the difference in kurtosis observed between nonpregnant and pregnant patients was present. Ultimately, there was a significant loss of collagen alignment observed in pregnant patients. The lower end of the standard deviation marked a patient with multiple past pregnancies and who later had PTB, while the higher end of the standard deviation was a young woman with her first pregnancy. Similarly, the lower end of the collagen alignment for the nonpregnant patients was a middle-aged woman who has gave birth to children. Continuation of the study will be necessary to elucidate if a more definitive marker can be found in diagnosing PTB.

In order to draw more substantial conclusions regarding the changes in cervical collagen during pregnancy and its relationship with preterm birth a larger sample size is required compared to the preliminary study reported on in this dissertation. Further analysis of data is needed to find a parameter which may better correlate with onset of delivery. There is an ongoing effort to develop more Mueller matrix polarimetry capable colposcopes for use in new studies with access to larger patient populations. The designs of these new colposcopes may also be improved on to further decrease acquisition time or improve portability for possible studies in low-resource settings by using different polarimetry methodologies.

References

[1] G. Roy, N. Roy, Relation between circular and linear depolarization ratios under multiple-scattering conditions. *Appl. Opt.* **47**, 6563-6579 (2008).

[2] N. Ghosh, I. A. Vitkin, Tissue polarimetry: concepts, challenges, applications, and outlook. *J Biomed Opt* **16**, 110801 (2011).

[3] S. L. Jacques, J. C. Ramella-Roman, K. Lee, Imaging skin pathology with polarized light. *Journal of Biomedical Optics* **7**, 329-340 (2002).

[4] S. G. Demos, R. R. Alfano, Optical polarization imaging. *Appl Opt* **36**, 150-155 (1997).

[5] S. G. Demos, A. J. Papadopoulos, H. Savage, A. S. Heerdt, S. Schantz, R. R. Alfano, Polarization filter for biomedical tissue optical imaging. *Photochem Photobiol* **66**, 821-825 (1997).

[6] S. P. Morgan, I. M. Stockford, Surface-reflection elimination in polarization imaging of superficial tissue. *Optics Letters* **28**, 114-116 (2003).

[7] M. F. Wood, X. Guo, I. A. Vitkin, Polarized light propagation in multiply scattering media exhibiting both linear birefringence and optical activity: Monte Carlo model and experimental methodology. *J Biomed Opt* **12**, 014029 (2007).

[8] S. Demos, H. Radousky, R. Alfano, Deep subsurface imaging in tissues using spectral and polarization filtering. *Optics Express* **7**, 23-28 (2000).

[9] B. Kunnen, C. Macdonald, A. Doronin, S. Jacques, M. Eccles, I. Meglinski, Application of circularly polarized light for non-invasive diagnosis of cancerous tissues and turbid tissue-like scattering media. *Journal of Biophotonics* **8**, 317-323 (2015).

[10] T. Yun, N. Zeng, W. Li, D. Li, X. Jiang, H. Ma, Monte Carlo simulation of polarized photon scattering in anisotropic media. *Optics Express* **17**, 16590-16602 (2009).

[11] J. Ramella-Roman, S. Prahl, S. Jacques, Three Monte Carlo programs of polarized light transport into scattering media: part I. *Optics Express* **13**, 4420-4438 (2005).

[12] K. M. Myers, H. Feltovich, E. Mazza, J. Vink, M. Bajka, R. J. Wapner, T. J. Hall, M. House, The mechanical role of the cervix in pregnancy. *J Biomech* **48**, 1511-1523 (2015).

[13] H. C. Wells, K. H. Sizeland, N. Kirby, A. Hawley, S. Mudie, R. G. Haverkamp, Collagen Fibril Structure and Strength in Acellular Dermal Matrix Materials of Bovine, Porcine, and Human Origin. *ACS Biomaterials Science & Engineering* **1**, 1026-1038 (2015).

[14] J. C. Ramella-Roman, T. Ruiz, P. Ghassemi, T. E. Travis, J. W. Shupp, J. Chue-Sang, Y. Bai. (2015), vol. 9303, pp. 93030I-93030I-93035.

[15] S. Sugita, T. Matsumoto, Quantitative measurement of the distribution and alignment of collagen fibers in unfixed aortic tissues. *J Biomech* **46**, 1403-1407 (2013).

[16] P. J. Wu, J. T. Walsh, Stokes polarimetry imaging of rat-tail tissue in a turbid medium using incident circularly polarized light. *Lasers in Surgery and Medicine* **37**, 396-406 (2005).

[17] W. F. Cheong, S. A. Prahl, A. J. Welch, A review of the optical properties of biological tissues. *IEEE Journal of Quantum Electronics* **26**, 2166-2185 (1990).

[18] A. Pierangelo, S. Manhas, A. Benali, C. Fallet, M. R. Antonelli, T. Novikova, B. Gayet, P. Validire, A. De Martino, Ex vivo photometric and polarimetric multilayer characterization of human healthy colon by multispectral Mueller imaging. *J Biomed Opt* **17**, 066009 (2012).

[19] A. Pierangelo, S. Manhas, A. Benali, C. Fallet, J. L. Totobenazara, M. R. Antonelli, T. Novikova, B. Gayet, A. De Martino, P. Validire, Multispectral Mueller polarimetric imaging detecting residual cancer and cancer regression after neoadjuvant treatment for colorectal carcinomas. *J Biomed Opt* **18**, 046014 (2013).

[20] N. Ghosh, M. F. Wood, I. A. Vitkin, Mueller matrix decomposition for extraction of individual polarization parameters from complex turbid media exhibiting multiple scattering, optical activity, and linear birefringence. *J Biomed Opt* **13**, 044036 (2008).

[21] R. R. Anderson, Polarized light examination and photography of the skin. *Arch Dermatol* **127**, 1000-1005 (1991).

[22] S. L. Jacques, J. R. Roman, K. Lee, Imaging superficial tissues with polarized light. *Lasers Surg Med* **26**, 119-129 (2000).

[23] S. L. Jacques, J. C. Ramella-Roman, K. Lee, Imaging skin pathology with polarized light. *J Biomed Opt* **7**, 329-340 (2002).

[24] S. P. Morgan, Q. Zhu, I. M. Stockford, J. A. Crowe, Rotating orthogonal polarization imaging. *Opt Lett* **33**, 1503-1505 (2008).

[25] W. Groner, J. W. Winkelman, A. G. Harris, C. Ince, G. J. Bouma, K. Messmer, R. G. Nadeau, Orthogonal polarization spectral imaging: a new method for study of the microcirculation. *Nat Med* **5**, 1209-1212 (1999).

[26] O. Genzel-Boroviczeny, J. Strotgen, A. G. Harris, K. Messmer, F. Christ, Orthogonal polarization spectral imaging (OPS): a novel method to measure the microcirculation in term and preterm infants transcutaneously. *Pediatr Res* **51**, 386-391 (2002).

[27] S. Langer, F. Born, R. Hatz, P. Biberthaler, K. Messmer, Orthogonal polarization spectral imaging versus intravital fluorescent microscopy for microvascular studies in wounds. *Ann Plast Surg* **48**, 646-653 (2002).

[28] S. Langer, A. G. Harris, P. Biberthaler, E. von Dobschuetz, K. Messmer, Orthogonal polarization spectral imaging as a tool for the assessment of hepatic microcirculation: a validation study. *Transplantation* **71**, 1249-1256 (2001).

[29] E. Uhl, J. Lehmberg, H. J. Steiger, K. Messmer, Intraoperative detection of early microvasospasm in patients with subarachnoid hemorrhage by using orthogonal polarization spectral imaging. *Neurosurgery* **52**, 1307-1315; disacussion 1315-1307 (2003).

[30] E. von Dobschuetz, P. Biberthaler, T. Mussack, S. Langer, K. Messmer, T. Hoffmann, Noninvasive in vivo assessment of the pancreatic microcirculation: orthogonal polarization spectral imaging. *Pancreas* **26**, 139-143 (2003).

[31] E. DeHoog, H. Luo, K. Oka, E. Dereniak, J. Schwiegerling, Snapshot polarimeter fundus camera. *Appl Opt* **48**, 1663-1667 (2009).

[32] P. Ghassemi, P. Lemaillet, T. A. Germer, J. W. Shupp, S. S. Venna, M. E. Boisvert, K. E. Flanagan, M. H. Jordan, J. C. Ramella-Roman, Out-of-plane Stokes imaging polarimeter for early skin cancer diagnosis. *J Biomed Opt* **17**, 076014 (2012).

[33] N. Agarwal, J. Yoon, E. Garcia-Caurel, T. Novikova, J. C. Vanel, A. Pierangelo, A. Bykov, A. Popov, I. Meglinski, R. Ossikovski, Spatial evolution of depolarization in homogeneous turbid media within the differential Mueller matrix formalism. *Opt Lett* **40**, 5634-5637 (2015).

[34] M. R. Antonelli, A. Pierangelo, T. Novikova, P. Validire, A. Benali, B. Gayet, A. De Martino, Mueller matrix imaging of human colon tissue for cancer diagnostics: how Monte Carlo modeling can help in the interpretation of experimental data. *Opt Express* **18**, 10200-10208 (2010).

[35] M. R. Antonelli, A. Pierangelo, T. Novikova, P. Validire, A. Benali, B. Gayet, A. De Martino, Impact of model parameters on Monte Carlo simulations of

backscattering Mueller matrix images of colon tissue. *Biomed Opt Express* **2**, 1836-1851 (2011).

[36] T. Novikova, B. Drevillon, L. Schwartz, P. Validire, A. Nazac, R. Ossikovski, E. Garcia-Caurel, B. Laude-Boulesteix, M. Anastasiadou, M. Losurdo, K. Hinderl, B. H. Ibrahim, M. R. Antonelli, A. Pierangelo, S. Deby, S. Roussel, S. Manhas, J. Vizet, D. Pagnoux, S. Bancelin, M. C. Schanne-Klein, J. Rehbinder, H. Haddad, F. Moreau, J. C. Vanel, P. R. Cabarrocas, V. Tuchin, S. Jacques, Special Section Guest Editorial: Antonello De Martino (1954-2014): in memoriam. *J Biomed Opt* **21**, 71101 (2016).

[37] A. Pierangelo, A. Benali, M. R. Antonelli, T. Novikova, P. Validire, B. Gayet, A. De Martino, Ex-vivo characterization of human colon cancer by Mueller polarimetric imaging. *Opt Express* **19**, 1582-1593 (2011).

[38] A. Pierangelo, A. Nazac, A. Benali, P. Validire, H. Cohen, T. Novikova, B. H. Ibrahim, S. Manhas, C. Fallet, M. R. Antonelli, A. D. Martino, Polarimetric imaging of uterine cervix: a case study. *Opt Express* **21**, 14120-14130 (2013).

[39] J. Rehbinder, H. Haddad, S. Deby, B. Teig, A. Nazac, T. Novikova, A. Pierangelo, F. Moreau, Ex vivo Mueller polarimetric imaging of the uterine cervix: a first statistical evaluation. *J Biomed Opt* **21**, 71113 (2016).

[40] P. Yang, H. L. Wei, G. W. Kattawar, Y. X. Hu, D. M. Winker, C. A. Hostetler, B. A. Baum, Sensitivity of the backscattering Mueller matrix to particle shape and thermodynamic phase. *Applied Optics* **42**, 4389-4395 (2003).

[41] A. H. Hielscher, S. Bartel, Diffuse backscattering Mueller matrix analysis for tissue diagnostics with polarized light. *Proc Spie* **3917**, 43-53 (2000).

[42] B. D. Cameron, M. J. Rakovi, M. Mehrubeo Lu, G. W. Kattawar, S. Rastegar, L. V. Wang, G. L. Cote, Measurement and calculation of the two-dimensional backscattering Mueller matrix of a turbid medium: errata. *Opt Lett* **23**, 1630 (1998).

[43] B. D. Cameron, M. J. Rakovic, M. Mehrubeoglu, G. W. Kattawar, S. Rastegar, L. V. Wang, G. L. Cote, Measurement and calculation of the two-dimensional backscattering Mueller matrix of a turbid medium. *Opt Lett* **23**, 485-487 (1998).

[44] D. Cote, I. Vitkin, Robust concentration determination of optically active molecules in turbid media with validated three-dimensional polarization sensitive Monte Carlo calculations. *Opt Express* **13**, 148-163 (2005).

[45] M. J. Rakovic, G. W. Kattawar, M. B. Mehrubeoglu, B. D. Cameron, L. V. Wang, S. Rastegar, G. L. Cote, Light backscattering polarization patterns from turbid media: theory and experiment. *Appl Opt* **38**, 3399-3408 (1999).

[46] M. Mehrubeoglu, N. Kehtarnavaz, S. Rastegar, L. V. Wang, Effect of molecular concentrations in tissue-simulating phantoms on images obtained using diffuse reflectance polarimetry. *Optics Express* **3**, 286-298 (1998).

[47] S. Alali, K. J. Aitken, A. Schroder, A. Gribble, D. J. Bagli, I. A. Vitkin, Assessment of local structural disorders of the bladder wall in partial bladder outlet obstruction using polarized light imaging. *Biomed Opt Express* **5**, 621-629 (2014).

[48] M. F. Wood, N. Ghosh, M. A. Wallenburg, S. H. Li, R. D. Weisel, B. C. Wilson, R. K. Li, I. A. Vitkin, Polarization birefringence measurements for characterizing the myocardium, including healthy, infarcted, and stem-cell-regenerated tissues. *J Biomed Opt* **15**, 047009 (2010).

[49] M. Ahmad, S. Alali, A. Kim, M. F. Wood, M. Ikram, I. A. Vitkin, Do different turbid media with matched bulk optical properties also exhibit similar polarization properties? *Biomed Opt Express* **2**, 3248-3258 (2011).

[50] S. Alali, M. Ahmad, A. Kim, N. Vurgun, M. F. Wood, I. A. Vitkin, Quantitative correlation between light depolarization and transport albedo of various porcine tissues. *J Biomed Opt* **17**, 045004 (2012).

[51] M. F. Wood, D. Cote, I. A. Vitkin, Combined optical intensity and polarization methodology for analyte concentration determination in simulated optically clear and turbid biological media. *J Biomed Opt* **13**, 044037 (2008).

[52] M. F. Wood, N. Ghosh, E. H. Moriyama, B. C. Wilson, I. A. Vitkin, Proof-of-principle demonstration of a Mueller matrix decomposition method for polarized light tissue characterization in vivo. *J Biomed Opt* **14**, 014029 (2009).

[53] B. Boulbry, J. C. Ramella-Roman, T. A. Germer, Improved method for calibrating a Stokes polarimeter. *Applied Optics* **46**, 8533-8541 (2007).

[54] K. M. Twietmeyer, R. A. Chipman, Optimization of Mueller matrix polarimeters in the presence of error sources. *Opt Express* **16**, 11589-11603 (2008).

[55] J. Chue-Sang, J. C. Ramella-Roman, in *SPIE BiOS*. (SPIE, 2018), vol. 10478, pp. 8.

[56] J. Dillet, C. Baravian, F. Caton, A. Parker, Size determination by use of two-dimensional Mueller matrices backscattered by optically thick random media. *Applied Optics* **45**, 4669-4678 (2006).

[57] S. Y. Lu, R. A. Chipman, Interpretation of Mueller matrices based on polar decomposition. *Journal of the Optical Society of America a-Optics Image Science and Vision* **13**, 1106-1113 (1996).

[58] P. Shukla, A. Pradhan, Mueller decomposition images for cervical tissue: Potential for discriminating normal and dysplastic states. *Optics Express* **17**, 1600-1609 (2009).

[59] K. H. Kim, M. C. Pierce, G. Maguluri, B. H. Park, S. J. Yoon, M. Lydon, R. Sheridan, J. F. de Boer, In vivo imaging of human burn injuries with polarization-sensitive optical coherence tomography. *Journal of Biomedical Optics* **17**, 066012-066012 (2012).

[60] J. C. Ramella-Roman, S. A. Prahl, S. L. Jacques, Three Monte Carlo programs of polarized light transport into scattering media: part II. *Optics Express* **13**, 10392-10405 (2005).

[61] I. Meglinski, M. Kirillin, V. Kuzmin, R. Myllyla, Simulation of polarization-sensitive optical coherence tomography images by a Monte Carlo method. *Optics Letters* **33**, 1581-1583 (2008).

[62] J. M. Tielsch, Global Incidence of Preterm Birth. *Nestle Nutr Inst Workshop Ser* **81**, 9-15 (2015).

[63] F. Bloomfield, How is maternal nutrition related to preterm birth? *Annu Rev Nutr.* **31**, 235-261 (2011).

[64] R. E. Garfield, H. Maul, L. Shi, W. Maner, C. Fittkow, G. Olsen, G. R. Saade, Methods and devices for the management of term and preterm labor. *Ann N Y Acad Sci* **943**, 203-224 (2001).

[65] F. Soleimani, F. Zaheri, F. Abdi, Long-Term Neurodevelopmental Outcomes After Preterm Birth. *Iran Red Crescent Med J.* **16**, e17965 (2014).

[66] l. S. Saiga, L. Doyle, An overview of mortality and sequelae of preterm birth from infancy to adulthood. *Lancet* **371**, 261–269 (2008).

[67] M. Kemp, M. Saito, J. Newnham, I. Nitsos, K. Okamura, S. Kallapur, Preterm birth, infection, and inflammation advances from the study of Animal Models. *Reprod Sci* **17**, 619–628 (2010).

[68] R. L. Goldenberg, J. F. Culhane, J. D. Iams, R. Romero, Epidemiology and causes of preterm birth. *Lancet* **371**, 75-84 (January 5, 2008).

[69] N. Kozuki, A. Lee, M. Silveira, C. Victora, L. Adair, J. Humphrey, R. Ntozini, R. Black, J. Katz, The associations of birth intervals with small-for-gestational-age, preterm, and neonatal and infant mortality: a meta-analysis. *BMC Public Health* **13 Supp 3**, (2013).

[70] R. L. Goldenberg, J. F. Culhane, J. D. Iams, R. Romero, Epidemiology and causes of preterm birth. *Lancet* **371**, 75-84 (2008).

[71] M. S. Esplin, Preterm Birth: A Review of Genetic Factors and Future Directions for Genetic Study. *Obstetrical & Gynecological Survey* **61**, 800-806 (2006).

[72] J. D. Iams, R. L. Goldenberg, P. J. Meis, B. M. Mercer, A. Moawad, A. Das, E. Thom, D. McNellis, R. L. Copper, F. Johnson, J. M. Roberts, The length of the cervix and the risk of spontaneous premature delivery. National Institute of Child Health and Human Development Maternal Fetal Medicine Unit Network. *N Engl J Med* **334**, 567-572 (1996).

[73] E. F. Foxman, P. Jarolim, Use of the fetal fibronectin test in decisions to admit to hospital for preterm labor. *Clinical Chemistry* **50**, 663-665 (2004).

[74] J. D. Iams, V. Berghella, Care for Women With Prior Preterm Birth. *Am. J. Obstet. Gynecol.* **203**, 89-100 (2010).

[75] H. Feltovich, K. Nam, T. Hall, Quantitative Ultrasound Assessment of Cervical. *Ultrason Imaging.* **32**, 131-142. (2010).

[76] C. M. Nold, L. P. Anton, A. P. Brown, M. M. Elovitz, Inflammation promotes a cytokine response and disrupts the cervical epithelial barrier: a possible mechanism of premature cervical remodeling and preterm birth. *Am J Obstet Gynecol* **206**, 1-7 (2012).

[77] L. Shi, S. Q. Shi, G. R. Saade, K. Chwalisz, R. E. Garfield, Changes in cervical resistance and collagen fluorescence during gestation in rats. *Journal of perinatal medicine* **27**, 188-194 (1999).

[78] H. Maul, G. Olson, C. T. Fittkow, G. R. Saade, R. E. Garfield, Cervical light-induced fluorescence in humans decreases throughout gestation and before delivery: Preliminary observations. *American Journal of Obstetrics & Gynecology* **188**, 537-541.

[79] M. L. Akins, K. Luby-Phelps, R. A. Bank, M. Mahendroo, Cervical Softening During Pregnancy: Regulated Changes in Collagen Cross-Linking and Composition of Matricellular Proteins in the Mouse. *Biology of Reproduction* **84**, 1053-1062 (2011).

[80] S. Bancelin, A. Nazac, B. H. Ibrahim, P. Dokladal, E. Decenciere, B. Teig, H. Haddad, H. Fernandez, M. C. Schanne-Klein, A. De Martino, Determination of collagen fiber orientation in histological slides using Mueller microscopy and validation by second harmonic generation imaging. *Opt Express* **22**, 22561-22574 (2014).

[81] R. A. Word, X. H. Li, M. Hnat, K. Carrick, Dynamics of cervical remodeling during pregnancy and parturition: mechanisms and current concepts. *Semin Reprod Med* **25**, 69-79 (2007).

[82] R. Holt, B. C. Timmons, Y. Akgul, M. L. Akins, M. Mahendroo, The molecular mechanisms of cervical ripening differ between term and preterm birth. *Endocrinology* **152**, 1036-1046 (2011).

[83] L. M. Reusch, H. Feltovich, L. C. Carlson, G. Hall, P. J. Campagnola, K. W. Eliceiri, T. J. Hall, Nonlinear optical microscopy and ultrasound imaging of human cervical structure. *J Biomed Opt* **18**, 031110 (2013).

[84] K. M. Myers, S. Socrate, A. Paskaleva, M. House, A study of the anisotropy and tension/compression behavior of human cervical tissue. *J Biomech Eng* **132**, 021003 (2010).

[85] R. M. Aspden, Collagen organisation in the cervix and its relation to mechanical function. *Coll Relat Res* **8**, 103-112 (1988).

[86] M. Fernandez, M. House, S. Jambawalikar, N. Zork, J. Vink, R. Wapner, K. Myers, Investigating the mechanical function of the cervix during pregnancy using finite element models derived from high-resolution 3D MRI. *Computer Methods in Biomechanics and Biomedical Engineering* **19**, 404-417 (2016).

[87] K. Yoshida, H. Jiang, M. Kim, J. Vink, S. Cremers, D. Paik, R. Wapner, M. Mahendroo, K. Myers, Quantitative Evaluation of Collagen Crosslinks and Corresponding Tensile Mechanical Properties in Mouse Cervical Tissue during Normal Pregnancy. *PLoS ONE* **9**, e112391 (2014).

[88] R. A. Word , X.-H. Li , M. Hnat , K. Carrick, Dynamics of Cervical Remodeling during Pregnancy and Parturition: Mechanisms and Current Concepts. *Semin Reprod Med* **25**, 069-079 (2007).

[89] K. Myers, H. Feltovich, E. Mazza, J. Vink, M. Bajka, Wapner, RJ, Hall, TJ, M. House, The mechanical role of the cervix in pregnancy. *J Biomech.*, (2015).

[90] J. Vizet, J. Rehbinder, S. Deby, S. Roussel, A. Nazac, R. Soufan, C. Genestie, C. Haie-Meder, H. Fernandez, F. Moreau, A. Pierangelo, In vivo imaging of uterine cervix with a Mueller polarimetric colposcope. *Scientific Reports* **7**, 2471 (2017).

[91] J. Chue-Sang, Y. Bai, S. Stoff, M. Gonzalez, N. Holness, J. Gomes, R. Jung, A. Gandjbakhche, V. V. Chernomordik, J. C. Ramella-Roman, Use of Mueller matrix polarimetry and optical coherence tomography in the characterization of cervical collagen anisotropy. *J Biomed Opt* **22**, 1-9 (2017).

[92] O. Reich, H. Fritsch, The Developmental Origin of Cervical and Vaginal Epithelium and Their Clinical Consequences: A Systematic Review. *Journal of Lower Genital Tract Disease* **18**, 358-360 (2014).

[93] D. C. Walker, B. H. Brown, A. D. Blackett, J. Tidy, R. H. Smallwood, A study of the morphological parameters of cervical squamous epithelium. *Physiological measurement* **24**, 121-135 (2003).

[94] P. N. Vassilakos, R; Catarino, R, in *Cervical cancer in developing countries*, A. Compano, Ed. (Geneva, Switzerland, 2015).

[95] P. Mukonoweshuro, A. Oriowolo, M. Smith, Audit of the histological definition of cervical transformation zone. *Journal of Clinical Pathology* **58**, 671-671 (2005).

[96] C. Lau, J. Mirkovic, C.-C. Yu, G. P. O'Donoghue, L. Galindo, R. Dasari, A. de las Morenas, M. Feld, E. Stier, Early detection of high-grade squamous intraepithelial lesions in the cervix with quantitative spectroscopic imaging. *Journal of Biomedical Optics* **18**, 076013 (2013).

[97] J. P. Kusanovic, E. Soto, J. Espinoza, S. Stites, L. F. Gonçalves, J. Santolaya, J. K. Nien, O. Erez, Y. Sorokin, R. Romero, Cervical Varix as a Cause of Vaginal Bleeding During Pregnancy – Prenatal Diagnosis by Color Doppler Ultrasound. *Journal of ultrasound in medicine : official journal of the American Institute of Ultrasound in Medicine* **25**, 545-549 (2006).

[98] V. T.-C. Chang, S. M. Bean, P. S. Cartwright, N. Ramanujam, Visible light optical spectroscopy is sensitive to neovascularization in the dysplastic cervix. *BIOMEDO* **15**, 057006 (2010).

[99] S. M. Yellon, Contributions to the dynamics of cervix remodeling prior to term and preterm birth†. *Biology of Reproduction* **96**, 13-23 (2017).

[100] C. He, H. He, X. Li, J. Chang, Y. Wang, S. Liu, N. Zeng, Y. He, H. Ma, Quantitatively differentiating microstructures of tissues by frequency distributions of Mueller matrix images. *Journal of Biomedical Optics* **20**, 105009-105009 (2015).

[101] B. F. Narice, N. H. Green, S. MacNeil, D. Anumba, Second Harmonic Generation microscopy reveals collagen fibres are more organised in the cervix of postmenopausal women. *Reproductive Biology and Endocrinology* **14**, 70 (2016).

[102] Y. Gan, W. Yao, K. M. Myers, J. Y. Vink, R. J. Wapner, C. P. Hendon, Analyzing three-dimensional ultrastructure of human cervical tissue using optical coherence tomography. *Biomed Opt Express* **6**, 1090-1108 (2015).

[103] N. Thekkek, R. Richards-Kortum, Optical Imaging for Cervical Cancer Detection: Solutions for a Continuing Global Problem. *Nature reviews. Cancer* **8**, 725-731 (2008).

[104] I. M. Orfanoudaki, D. Kappou, S. Sifakis, Recent advances in optical imaging for cervical cancer detection. *Archives of Gynecology and Obstetrics* **284**, 1197 (2011).

[105] A. Pierangelo, A. Nazac, A. Benali, P. Validire, H. Cohen, T. Novikova, B. H. Ibrahim, S. Manhas, C. Fallet, M.-R. Antonelli, A.-D. Martino, Polarimetric imaging of uterine cervix: a case study. *Optics Express* **21**, 14120-14130 (2013).

[106] S. Bancelin, A. Nazac, B. H. Ibrahim, P. Dokládal, E. Decencière, B. Teig, H. Haddad, H. Fernandez, M.-C. Schanne-Klein, A. De Martino, Determination of collagen fiber orientation in histological slides using Mueller microscopy and validation by second harmonic generation imaging. *Optics Express* **22**, 22561-22574 (2014).

[107] T. Collier, M. Follen, A. Malpica, R. Richards-Kortum, Sources of scattering in cervical tissue: determination of the scattering coefficient by confocal microscopy. *Applied Optics* **44**, 2072-2081 (2005).

[108] K. Sokolov, J. Aaron, B. Hsu, D. Nida, A. Gillenwater, M. Follen, C. MacAulay, K. Adler-Storthz, B. Korgel, M. Descour, R. Pasqualini, W. Arap, W. Lam, R. Richards-Kortum, Optical Systems for in Vivo Molecular Imaging of Cancer. *Technology in Cancer Research & Treatment* **2**, 491-504 (2003).

[109] R. A. Drezek, R. Richards-Kortum, M. A. Brewer, M. S. Feld, C. Pitris, A. Ferenczy, M. L. Faupel, M. Follen, Optical imaging of the cervix. *Cancer* **98**, 2015-2027 (2003).

[110] C. K. Brookner, U. Utzinger, G. Staerkel, R. Richards-Kortum, M. F. Mitchell, Cervical fluorescence of normal women. *Lasers in Surgery and Medicine* **24**, 29-37 (1999).

[111] C. T. Lam, M. S. Krieger, J. E. Gallagher, B. Asma, L. C. Muasher, J. W. Schmitt, N. Ramanujam, Design of a Novel Low Cost Point of Care Tampon (POCkeT) Colposcope for Use in Resource Limited Settings. *PLOS ONE* **10**, e0135869 (2015).

[112] C. Millien, M. C. Jean-Baptiste, G. Manite, D. Levitz. (2015), vol. 9314, pp. 93140A-93140A-93145.

[113] W. Yao, Y. Gan, K. M. Myers, J. Y. Vink, R. J. Wapner, C. P. Hendon, Collagen Fiber Orientation and Dispersion in the Upper Cervix of Non-Pregnant and Pregnant Women. *PLOS ONE* **11**, e0166709 (2016).

[114] K. M. Myers, C. P. Hendon, Y. Gan, W. Yao, K. Yoshida, M. Fernandez, J. Vink, R. J. Wapner, A continuous fiber distribution material model for human cervical tissue. *Journal of Biomechanics* **48**, 1533-1540 (2015).

[115] Y. Gan, W. Yao, K. M. Myers, C. P. Hendon, in *2014 36th Annual International Conference of the IEEE Engineering in Medicine and Biology Society*. (2014), pp. 3873-3876.

[116] B. L. McFarlin, J. Balash, V. Kumar, T. A. Bigelow, X. Pombar, J. S. Abramowicz, W. D. O'Brien Jr, Development of an Ultrasonic Method to Detect Cervical Remodeling in Vivo in Full-Term Pregnant Women. *Ultrasound in Medicine & Biology* **41**, 2533-2539 (2015).

[117] T. Y. Lau, H. K. Sangha, E. K. Chien, B. L. McFarlin, A. J. Wagoner Johnson, K. C. Toussaint, Application of Fourier transform-second-harmonic generation imaging to the rat cervix. *Journal of Microscopy* **251**, 77-83 (2013).

[118] L. M. Reusch, H. Feltovich, L. C. Carlson, G. Hall, P. J. Campagnola, K. W. Eliceiri, T. J. Hall, Nonlinear optical microscopy and ultrasound imaging of human cervical structure. *BIOMEDO* **18**, 031110 (2013).

[119] Y. Zhang, M. L. Akins, K. Murari, A compact fiber-optic SHG endomiscroscope and its application to visualize cervical remodeling during pregnancy. *Proc Natl Acad Sci U S A* **109**, (2012).

[120] K. Myers, S. Socrate, D. Tzeranis, M. House, Changes in the biochemical constituents and morphologic appearance of the human cervical stroma during pregnancy. *European Journal of Obstetrics & Gynecology and Reproductive Biology* **144, Supplement 1**, S82-S89 (2009).

[121] D. E. Birk, P. Brückner, in *The Extracellular Matrix: an Overview,* R. P. Mecham, Ed. (Springer Berlin Heidelberg, Berlin, Heidelberg, 2011), pp. 77-115.

[122] D. E. Birk, E. I. Zycband, S. Woodruff, D. A. Winkelmann, R. L. Trelstad, Collagen fibrillogenesis in situ: Fibril segments become long fibrils as the developing tendon matures. *Developmental Dynamics* **208**, 291-298 (1998).

[123] A. Blaustein, K. J. Kurman, *Blaustein's pathology of the female genital tract*. Springer, Ed., (New York, NY, 2011).

[124] M. House, D. L. Kaplan, S. Socrate, Relationships between mechanical properties and extracellular matrix constituents of the cervical stroma during pregnancy. *Seminars in perinatology* **33**, 300-307 (2009).

[125] K. Myers, S. Socrate, D. Tzeranis, M. House, Changes in the biochemical constituents and morphologic appearance of the human cervical stroma during pregnancy. *European Journal of Obstetrics & Gynecology and Reproductive Biology* **144S**, S82-S89 (2009).

[126] P. C. Leppert, Anatomy and physiology of cervical ripening. *Clin Obstet Gynecol* **38**, 267-279 (1995).

[127] D. Schlembach, L. Mackay, L. Shi, W. L. Maner, R. E. Garfield, H. Maul, Cervical ripening and insufficiency: from biochemical and molecular studies to in vivo clinical examination. *Eur J Obstet Gynecol Reprod Biol* **144 Suppl 1**, S70-76 (2009).

[128] K. Ito A Fau - Kitamura, Y. Kitamura K Fau - Mori, S. Mori Y Fau - Hirakawa, S. Hirakawa, The change in solubility of type I collagen in human uterine cervix in pregnancy at term. *Biomechemical Med* **21**, 262-270 (1979).

[129] M. Kleissl Hp Fau - van der Rest, F. van der Rest M Fau - Naftolin, F. H. Naftolin F Fau - Glorieux, A. Glorieux Fh Fau - de Leon, A. de Leon, Collagen changes in the human uterine cervix at parturition.

[130] R. J. Kuon, S. Q. Shi, H. Maul, C. Sohn, J. Balducci, L. Shi, R. E. Garfield, A novel optical method to assess cervical changes during pregnancy and use to evaluate the effects of progestins on term and preterm labor. *Am J Obstet Gynecol* **205**, 82.e15-20 (2011).

[131] W. Stephan, J. Thomas, S. Peter, S. Philipp, B. Peter, N. Peter, C. Rosmarie, B. Michael, Three-dimensional fiber architecture of the nonpregnant human uterus determined ex vivo using magnetic resonance diffusion tensor imaging. *The Anatomical Record Part A: Discoveries in Molecular, Cellular, and Evolutionary Biology* **288A**, 84-90 (2006).

[132] N. M. Zork, K. M. Myers, K. Yoshida, S. Cremers, H. Jiang, C. V. Ananth, R. J. Wapner, J. Kitajewski, J. Vink, A systematic evaluation of collagen cross-links in the human cervix. *Am J Obstet Gynecol* **212**, 321 e321-328 (2015).

[133] M. Fernandez, M. House, S. Jambawalikar, N. Zork, J. Vink, R. Wapner, K. Myers, Investigating the mechanical function of the cervix during pregnancy using finite element models derived from high-resolution 3D MRI. *Comput Methods Biomech Biomed Engin*, 1-14 (2015).

[134] M. L. Akins, K. Luby-Phelps, M. Mahendroo, Second harmonic generation imaging as a potential tool for staging pregnancy and predicting preterm birth (vol 15, 026020, 2010). *Journal of Biomedical Optics* **15**, (2010).

[135] C. P. Read, R. A. Word, M. A. Ruscheinsky, B. C. Timmons, M. S. Mahendroo, Cervical remodeling during pregnancy and parturition: molecular characterization of the softening phase in mice. *Reproduction* **134**, 327-340 (2007).

[136] L. Granstrom, G. Ekman, U. Ulmsten, A. Malmstrom, Changes in the connective tissue of corpus and cervix uteri during ripening and labour in term pregnancy. *Br J Obstet Gynaecol* **96**, 1198-1202 (1989).

[137] M. B. Sennstrom, G. Ekman, G. Westergren-Thorsson, A. Malmstrom, B. Bystrom, U. Endresen, N. Mlambo, M. Norman, B. Stabi, A. Brauner, Human cervical ripening, an inflammatory process mediated by cytokines. *Mol Hum Reprod* **6**, 375-381 (2000).

[138] R. Osmers, W. Rath, M. A. Pflanz, W. Kuhn, H. W. Stuhlsatz, M. Szeverenyi, Glycosaminoglycans in cervical connective tissue during pregnancy and parturition. *Obstet Gynecol* **81**, 88-92 (1993).

[139] K. J. Straach, J. M. Shelton, J. A. Richardson, V. C. Hascall, M. S. Mahendroo, Regulation of hyaluronan expression during cervical ripening. *Glycobiology* **15**, 55-65 (2005).

[140] F. G. Cunningham, J. W. Williams, *Williams obstetrics*. (McGraw-Hill Medical, New York, ed. 23rd, 2010), pp. xv, 1385 p.

[141] R. Romero, J. Espinoza, J. P. Kusanovic, F. Gotsch, S. Hassan, O. Erez, T. Chaiworapongsa, M. Mazor, The preterm parturition syndrome. *BJOG* **113 Suppl 3**, 17-42 (2006).

[142] M. L. Akins, K. Luby-Phelps, M. Mahendroo, Second harmonic generation imaging as a potential tool for staging pregnancy and predicting preterm birth. *BIOMEDO* **15**, 026020-026020-026010 (2010).

[143] B. Timmons, M. Akins, M. Mahendroo, Cervical remodeling during pregnancy and parturition. *Trends in endocrinology and metabolism: TEM* **21**, 353-361 (2010).

[144] *Biology of the Uterus*. (Springer, New York, NY, 1977).

[145] E. El Maradny, N. Kanayama, H. Kobayashi, B. Hossain, S. Khatun, S. Liping, T. Kobayashi, T. Terao, The role of hyaluronic acid as a mediator and regulator of cervical ripening. *Hum Reprod* **12**, 1080-1088 (1997).

[146] M. Iwahashi, Y. Muragaki, A. Ooshima, N. Umesaki, Decreased Type I Collagen Expression in Human Uterine Cervix during Pregnancy. *The Journal of Clinical Endocrinology & Metabolism* **88**, 2231-2235 (2003).

[147] K. M. Myers, A. P. Paskaleva, M. House, S. Socrate, Mechanical and biochemical properties of human cervical tissue. *Acta biomaterialia* **4**, 104-116 (2008).

[148] C. T. Fittkow, H. Maul, G. Olson, E. Martin, L. B. MacKay, G. R. Saade, R. E. Garfield, Light-induced fluorescence of the human cervix decreases after prostaglandin application for induction of labor at term. *Eur J Obstet Gynecol Reprod Biol* **123**, 62-66 (2005).

[149] A. Ito, D. Hiro, K. Sakyo, Y. Mori, The role of leukocyte factors on uterine cervical ripening and dilation. *Biol Reprod* **37**, 511-517 (1987).

[150] J. Ludmir, H. M. Sehdev, Anatomy and physiology of the uterine cervix. *Clin Obstet Gynecol* **43**, 433-439 (2000).

[151] N. M. Zork, K. M. Myers, K. Yoshida, S. Cremers, H. Jiang, C. V. Ananth, R. J. Wapner, J. Kitajewski, J. Vink, A systematic evaluation of collagen cross-links in the human cervix. *Am J Obstet Gynecol* **212**, 321.e321-328 (2015).

[152] S. D. Giattina, B. K. Courtney, P. R. Herz, M. Harman, S. Shortkroff, D. L. Stamper, B. Liu, J. G. Fujimoto, M. E. Brezinski, Assessment of coronary plaque collagen with polarization sensitive optical coherence tomography (PS-OCT). *Int J Cardiol* **107**, 400-409 (2006).

[153] J. Chue-Sang, Y. Bai, S. Stoff, D. Straton, S. Ramaswamy, J. C. Ramella-Roman, Use of combined polarization-sensitive optical coherence tomography and Mueller matrix imaging for the polarimetric characterization of excised biological tissue. *Journal of Biomedical Optics* **21**, 071109-071109 (2016).

[154] J. Chue-Sang, N. Holness, M. Gonzalez, J. Greaves, I. Saytashev, S. Stoff, A. Gandjbakhche, V. V. Chernomordik, G. Burkett, J. C. Ramella-Roman, Use of Mueller matrix colposcopy in the characterization of cervical collagen anisotropy. *Journal of Biomedical Optics* **23**, 9 (2018).

[155] J. A. Izatt, M. D. Kulkarni, H. W. Wang, K. Kobayashi, M. V. Sivak, Optical coherence tomography and microscopy in gastrointestinal tissues. *Ieee Journal of Selected Topics in Quantum Electronics* **2**, 1017-1028 (1996).

[156] M. Wojtkowski, V. J. Srinivasan, T. H. Ko, J. G. Fujimoto, A. Kowalczyk, J. S. Duker, Ultrahigh-resolution, high-speed, Fourier domain optical coherence tomography and methods for dispersion compensation. *Optics Express* **12**, 2404-2422 (2004).

[157] A. M. Zysk, F. T. Nguyen, A. L. Oldenburg, D. L. Marks, S. A. Boppart, Optical coherence tomography: a review of clinical development from bench to bedside. *Journal of Biomedical Optics* **12**, 21 (2007).

[158] B. J. Vakoc, D. Fukumura, R. K. Jain, B. E. Bouma, Cancer imaging by optical coherence tomography: preclinical progress and clinical potential. *Nature Reviews Cancer* **12**, 363-368 (2012).

[159] P. F. Lee, Y. Bai, R. L. Smith, K. J. Bayless, A. T. Yeh, Angiogenic responses are enhanced in mechanically and microscopically characterized, microbial transglutaminase crosslinked collagen matrices with increased stiffness. *Acta Biomaterialia* **9**, 7178-7190 (2013).

[160] H. C. Gibbs, Y. Q. Bai, A. C. Lekven, A. T. Yeh, Imaging embryonic development with ultrashort pulse microscopy. *Optical Engineering* **53**, 12 (2014).

[161] H. C. Gibbs, C. R. Dodson, Y. Q. Bai, A. C. Lekven, A. T. Yeh, Combined lineage mapping and gene expression profiling of embryonic brain patterning using ultrashort pulse microscopy and image registration. *Journal of Biomedical Optics* **19**, 14 (2014).

[162] Y. Q. Bai, P. F. Lee, H. C. Gibbs, K. J. Bayless, A. T. Yeh, Dynamic multicomponent engineered tissue reorganization and matrix deposition measured with an integrated nonlinear optical microscopy-optical coherence microscopy system. *BIOMEDO* **19**, 10 (2014).

[163] Y. Q. Bai, P. F. Lee, J. D. Humphrey, A. T. Yeh, Sequential Multimodal Microscopic Imaging and Biaxial Mechanical Testing of Living Multicomponent Tissue Constructs. *Annals of Biomedical Engineering* **42**, 1791-1805 (2014).

[164] J. A. Burns, K. H. Kim, J. F. deBoer, R. R. Anderson, S. M. Zeitels, Polarization-sensitive optical coherence tomography imaging of benign and malignant laryngeal lesions: an in vivo study. *Otolaryngol Head Neck Surg* **145**, 91-99 (2011).

[165] S. Jiao, M. Todorovic, G. Stoica, L. V. Wang, Fiber-based polarization-sensitive Mueller matrix optical coherence tomography with continuous source polarization modulation. *Appl Opt* **44**, 5463-5467 (2005).

[166] S. Jiao, L. V. Wang, Two-dimensional depth-resolved Mueller matrix of biological tissue measured with double-beam polarization-sensitive optical coherence tomography. *Opt Lett* **27**, 101-103 (2002).

[167] S. Jiao, W. Yu, G. Stoica, L. V. Wang, Contrast mechanisms in polarization-sensitive Mueller-matrix optical coherence tomography and application in burn imaging. *Appl Opt* **42**, 5191-5197 (2003).

[168] C. Fan, G. Yao, Mapping local optical axis in birefringent samples using polarization-sensitive optical coherence tomography. *J Biomed Opt* **17**, 110501 (2012).

[169] C. Fan, G. Yao, Imaging myocardial fiber orientation using polarization sensitive optical coherence tomography. *Biomed Opt Express* **4**, 460-465 (2013).

[170] Y. Fukuma, Y. Okazaki, T. Shioiri, Y. Iida, H. Kikuta, M. Shirakashi, K. Yaoeda, H. Abe, K. Ohnuma, Retinal nerve fiber layer retardation measurements using a polarization-sensitive fundus camera. *J Biomed Opt* **16**, 076017 (2011).

[171] S. Makita, Y. J. Hong, M. Miura, Y. Yasuno, Degree of polarization uniformity with high noise immunity using polarization-sensitive optical coherence tomography. *Opt Lett* **39**, 6783-6786 (2014).

[172] S. W. Lee, J. H. Kang, J. Y. Yoo, M. S. Kang, J. T. Oh, B. M. Kim, Quantification of scattering changes using polarization-sensitive optical coherence tomography. *Journal of Biomedical Optics* **13**, (2008).

[173] K. L. Lurie, T. J. Moritz, A. K. Ellerbee, Design considerations for polarization-sensitive optical coherence tomography with a single input polarization state. *Biomed Opt Express* **3**, 2273-2287 (2012).

[174] L. X. Chin, X. J. Yang, R. A. McLaughlin, P. B. Noble, D. D. Sampson, En face parametric imaging of tissue birefringence using polarization-sensitive optical coherence tomography. *Journal of Biomedical Optics* **18**, (2013).

[175] M. Yamanari, S. Makita, Y. Yasuno, Polarization-sensitive swept-source optical coherence tomography with continuous source polarization modulation. *Opt Express* **16**, 5892-5906 (2008).

[176] B. Boulbry, J. C. Ramella-Roman, T. A. Germer, Improved method for calibrating a Stokes polarimeter. *Appl Opt* **46**, 8533-8541 (2007).

[177] P. Ghassemi, L. T. Moffatt, J. W. Shupp, J. C. Ramella-Roman, A new approach for optical assessment of directional anisotropy in turbid media. *Journal of Biophotonics* **9**, 100-108 (2016).

[178] M. Sun, H. He, N. Zeng, E. Du, Y. Guo, S. Liu, J. Wu, Y. He, H. Ma, Characterizing the microstructures of biological tissues using Mueller matrix and transformed polarization parameters. *Biomedical Optics Express* **5**, 4223-4234 (2014).

[179] M. F. G. Wood, N. Ghosh, E. H. Moriyama, B. C. Wilson, I. A. Vitkin, Proof-of-principle demonstration of a Mueller matrix decomposition method for polarized light tissue characterization in vivo. *Journal of Biomedical Optics* **14**, 014029-014029-014025 (2009).

[180] S. K. Nadkarni, M. C. Pierce, B. H. Park, J. F. de Boer, P. Whittaker, B. E. Bouma, J. E. Bressner, E. Halpern, S. L. Houser, G. J. Tearney, Measurement of Collagen

and Smooth Muscle Cell Content in Atherosclerotic Plaques Using Polarization-Sensitive Optical Coherence Tomography. *Journal of the American College of Cardiology* **49**, 1474-1481 (2007).

[181] M. E. Brezinski, in *Optical Coherence Tomography: Principles and Applications*. (Academic Press, Burlington, MA, 2006), chap. 16.1, pp. 462-472.

[182] E. Gotzinger, M. Pircher, W. Geitzenauer, C. Ahlers, B. Baumann, S. Michels, U. Schmidt-Erfurth, C. K. Hitzenberger, Retinal pigment epithelium segmentation by polarization sensitive optical coherence tomography. *Opt Express* **16**, 16410-16422 (2008).

[183] M. Sugita, M. Pircher, S. Zotter, B. Baumann, K. Saito, T. Makihira, N. Tomatsu, M. Sato, C. K. Hitzenberger, Analysis of optimum conditions of depolarization imaging by polarization-sensitive optical coherence tomography in the human retina. *J Biomed Opt* **20**, 016011 (2015).

[184] E. C. C. Cauberg, D. M. de Bruin, D. J. Faber, T. M. de Reijke, M. Visser, J. J. M. C. H. de la Rosette, T. G. van Leeuwen, Quantitative measurement of attenuation coefficients of bladder biopsies using optical coherence tomography for grading urothelial carcinoma of the bladder. *Journal of Biomedical Optics* **15**, 066013-066013-066016 (2010).

[185] Z. Lu, D. Kasaragod, S. J. Matcher, Conical scan polarization-sensitive optical coherence tomography. *Biomedical Optics Express* **5**, 752-762 (2014).

[186] L. A. Carrow, R. R. Greene, The epithelia of the pregnant cervix. *Am J Obstet Gynecol* **61**, 237-252 (1951).

[187] P. Ghassemi, L. T. Moffatt, J. W. Shupp, J. C. Ramella-Roman, A new approach for optical assessment of directional anisotropy in turbid media. *J Biophotonics* **9999**, (2015).

[188] N. Ghosh, M. F. Wood, S. H. Li, R. D. Weisel, B. C. Wilson, R. K. Li, I. A. Vitkin, Mueller matrix decomposition for polarized light assessment of biological tissues. *J Biophotonics* **2**, 145-156 (2009).

[189] A. Pewsey, The large-sample joint distribution of key circular statistics. *Metrika* **60**, 25-32 (2004).

[190] A. Pewsey, M. Newhauser, G. D. Ruxton, Circular Statistics in R. (2015).

[191] P. H. Westfall, Kurtosis as Peakedness, 1905 – 2014. R.I.P. *The American statistician* **68**, 191-195 (2014).

[192] D. D. Duncan, P. Lemaillet, M. Ibrahim, Q. D. Nguyen, M. Hiller, J. Ramella-Roman, Absolute blood velocity measured with a modified fundus camera. *Journal of Biomedical Optics* **15**, 056014 (2010).

[193] M. F. G. Wood, N. Vurgun, M. A. Wallenburg, I. A. Vitkin, Effects of formalin fixation on tissue optical polarization properties. *Physics in Medicine and Biology* **56**, N115 (2011).

[194] C. He, H. He, J. Chang, Y. Dong, S. Liu, N. Zeng, Y. He, H. Ma, Characterizing microstructures of cancerous tissues using multispectral transformed Mueller matrix polarization parameters. *Biomedical Optics Express* **6**, 2934-2945 (2015).

[195] M. F. G. Wood, N. Ghosh, S.-H. Li, R. D. Weisel, B. C. Wilson, R.-K. Li, A. Vitkin. (2009), vol. 7179, pp. 717908-717908-717909.

[196] D.-H. Kim, P. P. Provenzano, C. L. Smith, A. Levchenko, Matrix nanotopography as a regulator of cell function. *The Journal of Cell Biology* **197**, 351-360 (2012).

[197] J. P. Nott, E. A. Bonney, J. D. Pickering, N. A. B. Simpson, The structure and function of the cervix during pregnancy. *Translational Research in Anatomy* **2**, 1-7 (2016).

[198] M. House, M. O'Callaghan, S. Bahrami, D. Chelmow, J. Kini, D. Wu, S. Patz, R. A. Bhadelia, Magnetic resonance imaging of the cervix during pregnancy: Effect of gestational age and prior vaginal birth. *American Journal of Obstetrics and Gynecology* **193**, 1554-1560 (2005).

[199] K. A. Montejo, J. Chue-Sang, Y. Bai, S. Stoff, N. Holness, M. Gonzalez, J. Gomes, A. Gandjbakhche, V. V. Chernomordik, J. C. Ramella-Roman. (2017), vol. 10043, pp. 1004303-1004303-1004310.

[200] S. Alali, A. Gribble, I. A. Vitkin, Rapid wide-field Mueller matrix polarimetry imaging based on four photoelastic modulators with no moving parts. *Opt. Lett.* **41**, 1038-1041 (2016).

[201] S. Alali, I. A. Vitkin, Optimization of rapid Mueller matrix imaging of turbid media using four photoelastic modulators without mechanically moving parts. *Optical Engineering* **52**, (2013).

[202] S. Alali, I. A. Vitkin. (SPIE, 2015), vol. 20, pp. 9.

[203] S. Alali, T. Y. Yang, I. A. Vitkin, Rapid time-gated polarimetric Stokes imaging using photoelastic modulators. *Optics Letters* **38**, 2997-3000 (2013).

[204] N.-J. Jan, K. Lathrop, I. A. Sigal, Collagen Architecture of the Posterior Pole: High-Resolution Wide Field of View Visualization and Analysis Using Polarized Light Microscopy. *Investigative Ophthalmology & Visual Science* **58**, 735-744 (2017).

[205] H. Feltovich, T. Hall, V. Berghella, Beyond cervical length: emerging technologies for assessing the pregnant cervix. *Am J of Obstet and Gynecol* **07**, (2012).

[206] K. Montejo, J. Chue-Sang, B. Bai, S. Stoff, N. Holness, M. Gonzalez, J. Gomes, A. H. Gandjbakhche, V. Chernomordik, J. C. Ramella-Roman, *Use of Mueller matrix colposcopy in the characterization of cervical collagen anisotropy*. Proc. SPIE 10043, Diagnosis and Treatment of Diseases in the Breast and Reproductive System, (March 2, 2017); doi:10.1117/12.2250987 (2017), vol. 1004303.

[207] J. Chue-Sang, Y. Bai, S. Stoff, M. Gonzalez, J. Gomes, A. Gandjbakhche, V. V. Chernomordik, J. C. Ramella-Roman. (2017), vol. 10043, pp. 100430U-100430U-100411.

[208] V. V. Tuchin, Polarized light interaction with tissues. *Journal of Biomedical Optics* **21**, 071114-071114 (2016).

[209] J. Qi, D. S. Elson, Mueller polarimetric imaging for surgical and diagnostic applications: a review. *J Biophotonics* **10**, 950-982 (2017).

[210] J. F. de Boer, C. K. Hitzenberger, Y. Yasuno, Polarization sensitive optical coherence tomography - a review [Invited]. *Biomed Opt Express* **8**, 1838-1873 (2017).

[211] B. Baumann, Polarization Sensitive Optical Coherence Tomography: A Review of Technology and Applications. *Appl Sci-Basel* **7**, (2017).

[212] B. W. Pogue, M. S. Patterson, Review of tissue simulating phantoms for optical spectroscopy, imaging and dosimetry. *J Biomed Opt* **11**, 041102 (2006).

[213] N. Ghosh, M. F. G. Wood, I. A. Vitkin, Polarimetry in turbid, birefringent, optically active media: A Monte Carlo study of Mueller matrix decomposition in the backscattering geometry. *Journal of Applied Physics* **105**, 102023 (2009).

[214] J. J. Gil, R. Ossikovski, *Polarized Light and the Mueller Matrix Approach*. Series in Optics and Optoelectronics (CRC Press, 2016).

[215] Y. Lim, M. Yamanari, S. Fukuda, Y. Kaji, T. Kiuchi, M. Miura, T. Oshika, Y. Yasuno, Birefringence measurement of cornea and anterior segment by office-based polarization-sensitive optical coherence tomography. *Biomed Opt Express* **2**, 2392-2402 (2011).

[216] M. Wojtkowski, High-speed optical coherence tomography: basics and applications. *Appl Opt* **49**, D30-61 (2010).

[217] W. KAMINSKY, E. GUNN, R. SOURS, B. KAHR, Simultaneous false-colour imaging of birefringence, extinction and transmittance at camera speed. *Journal of Microscopy* **228**, 153-164 (2007).

[218] N. Ugryumova, J. Jacobs, M. Bonesi, S. J. Matcher, Novel optical imaging technique to determine the 3-D orientation of collagen fibers in cartilage: variable-incidence angle polarization-sensitive optical coherence tomography. *Osteoarthritis Cartilage* **17**, 33-42 (2009).

[219] D. K. Kasaragod, Z. Lu, J. Jacobs, S. J. Matcher, Experimental validation of an extended Jones matrix calculus model to study the 3D structural orientation of the collagen fibers in articular cartilage using polarization-sensitive optical coherence tomography. *Biomed. Opt. Express* **3**, 378-387 (2012).

[220] C.-M. Chang, Y.-L. Lo, N.-K. Tran, Y.-J. Chang, Optical characterization of porcine articular cartilage using a polarimetry technique with differential Mueller matrix formulism. *Appl. Opt.* **57**, 2121-2127 (2018).

[221] R. Lu, Q. Zhang, Y. Zhi, X. Yao, A polarization-sensitive light field imager for multi-channel angular spectroscopy of light scattering in biological tissues. *Quant Imaging Med Surg* **5**, 1-8 (2015).

[222] R. Oldenbourg, E. D. Salmon, P. T. Tran, Birefringence of single and bundled microtubules. *Biophysical Journal* **74**, 645-654 (1998).

[223] J. Chue-Sang, Y. Bai, S. Stoff, J. Gomez, R. Jung, J. C. Ramella-Roman, Use of Mueller matrix Polarimetry and Optical Coherence Tomography in the characterization of cervical collagen anisotropy (In print). *Journal of Biomedical Optics*, (2017).

[224] J. C. Ramella-Roman, K. Lee, S. A. Prahl, S. L. Jacques, Design, testing, and clinical studies of a handheld polarized light camera. *J Biomed Opt* **9**, 1305-1310 (2004).

[225] P. Ghassemi, L. T. Moffatt, J. W. Shupp, J. C. Ramella-Roman, A new approach for optical assessment of directional anisotropy in turbid media. *J Biophotonics* **9**, 100-108 (2016).

[226] P. Ghassemi, T. E. Travis, L. T. Moffatt, J. W. Shupp, J. C. Ramella-Roman, A polarized multispectral imaging system for quantitative assessment of hypertrophic scars. *Biomedical Optics Express* **5**, 3337-3354 (2014).

[227] M. Bonesi, H. Sattmann, T. Torzicky, S. Zotter, B. Baumann, M. Pircher, E. Götzinger, C. Eigenwillig, W. Wieser, R. Huber, C. K. Hitzenberger, High-speed polarization sensitive optical coherence tomography scan engine based on Fourier domain mode locked laser. *Biomedical Optics Express* **3**, 2987-3000 (2012).

[228] S. Sakai, M. Yamanari, Y. Lim, N. Nakagawa, Y. Yasuno, In vivo evaluation of human skin anisotropy by polarization-sensitive optical coherence tomography. *Biomed Opt Express* **2**, 2623-2631 (2011).

[229] S. Bancelin, A. Nazac, B. H. Ibrahim, P. Dokladal, E. Decenciere, B. Teig, H. Haddad, H. Fernandez, M. C. Schanne-Klein, A. De Martino, Determination of collagen fiber orientation in histological slides using Mueller microscopy and validation by second harmonic generation imaging. *Opt. Express* **22**, 22561-22574 (2014).

[230] J. Chue-Sang, Y. Bai, S. Stoff, D. Straton, S. Ramaswamy, J. C. Ramella-Roman, Use of combined polarization-sensitive optical coherence tomography and Mueller matrix imaging for the polarimetric characterization of excised biological tissue. *J Biomed Opt* **21**, 71109 (2016).

[231] M. Todorović, S. Jiao, L. V. Wang, G. Stoica, Determination of local polarization properties of biological samples in the presence of diattenuation by use of Mueller optical coherence tomography. *Optics Letters* **29**, 2402-2404 (2004).

[232] M. R. Antonelli, Ecole polytechnique, France, (2011).

[233] W. Goth, B. Yang, J. Lesicko, A. Allen, M. S. Sacks, J. W. Tunnell. (2016), vol. 9710, pp. 971019-971019-971018.

[234] C. Fan, G. Yao, Mapping local retardance in birefringent samples using polarization sensitive optical coherence tomography. *Optics Letters* **37**, 1415-1417 (2012).

[235] E. M. Spiesz, W. Kaminsky, P. K. Zysset, A quantitative collagen fibers orientation assessment using birefringence measurements: calibration and application to human osteons. *J Struct Biol* **176**, 302-306 (2011).

[236] Z. Lu, D. K. Kasaragod, S. J. Matcher, Optic axis determination by fibre-based polarization-sensitive swept-source optical coherence tomography. *Phys Med Biol* **56**, 1105-1122 (2011).

[237] B. Yang, J. Lesicko, M. Sharma, M. Hill, M. S. Sacks, J. W. Tunnell, Polarized light spatial frequency domain imaging for non-destructive quantification of soft tissue fibrous structures. *Biomed Opt Express* **6**, 1520-1533 (2015).

[238] M. A. Wallenburg, M. Pop, M. F. G. Wood, N. Ghosh, G. A. Wright, I. A. Vitkin, Comparison of Optical Polarimetry and Diffusion Tensor Mr Imaging for Assessing Myocardial Anisotropy. *Journal of Innovative Optical Health Sciences* **03**, 109-121 (2010).

[239] X. Li, J. C. Ranasinghesagara, G. Yao, Polarization-sensitive reflectance imaging in skeletal muscle. *Opt Express* **16**, 9927-9935 (2008).

[240] C. P. Fleming, C. M. Ripplinger, B. Webb, I. R. Efimov, A. M. Rollins, Quantification of cardiac fiber orientation using optical coherence tomography. *Journal of biomedical optics* **13**, 030505-030505 (2008).

[241] H. R. Lee, T. S. H. Yoo, P. Li, C. Lotz, F. K. Groeber-Becker, S. Dembski, E. Garcia-Caurel, R. Ossikovski, T. Novikova, in *SPIE Photonics Europe*. (SPIE, 2018), vol. 10677, pp. 8.

[242] R. Ossikovski, Differential matrix formalism for depolarizing anisotropic media. *Opt. Lett.* **36**, 2330-2332 (2011).

[243] J. Qi, D. S. Elson, A high definition Mueller polarimetric endoscope for tissue characterisation. *Scientific Reports* **6**, 25953 (2016).

[244] C. M. Chang, Y. L. Lo, N. K. Tran, Y. J. Chang, Optical characterization of porcine articular cartilage using a polarimetry technique with differential Mueller matrix formulism. *Appl. Opt.* **57**, 2121-2127 (2018).

[245] A. H. Hielscher, J. R. Mourant, I. J. Bigio, Influence of particle size and concentration on the diffuse backscattering of polarized light from tissue phantoms and biological cell suspensions. *Applied Optics* **36**, 125-135 (1997).

[246] Y. Gan, C. P. Fleming, Extracting three-dimensional orientation and tractography of myofibers using optical coherence tomography. *Biomedical Optics Express* **4**, 2150-2165 (2013).

[247] B. Baumann, S. O. Baumann, T. Konegger, M. Pircher, E. Gotzinger, F. Schlanitz, C. Schutze, H. Sattmann, M. Litschauer, U. Schmidt-Erfurth, C. K. Hitzenberger, Polarization sensitive optical coherence tomography of melanin provides intrinsic contrast based on depolarization. *Biomed Opt Express* **3**, 1670-1683 (2012).

[248] S. Sridhar, A. Da Silva, Enhanced contrast and depth resolution in polarization imaging using elliptically polarized light. *Journal of Biomedical Optics* **21**, 071107-071107 (2016).

[249] H. T. T. Pham, A. L. T. Nguyen, T. V. Vo, K. C. Huynh, Q. H. Phan, Optical parameters of human blood plasma, collagen, and calfskin based on the Stokes-Mueller technique. *Appl. Opt.* **57**, 4353-4359 (2018).

[250] J. M. Schmitt, A. H. Gandjbakhche, R. F. Bonner, Use of Polarized-Light to Discriminate Short-Path Photons in a Multiply Scattering Medium (Vol 31, Pg 6535, 1992). *Applied Optics* **32**, 2186-2186 (1993).

[251] S. Rehn, A. Planat-Chretien, M. Berger, J. M. Dinten, C. Deumie, A. da Silva, Depth probing of diffuse tissues controlled with elliptically polarized light. *J Biomed Opt* **18**, 16007 (2013).

[252] F. C. Mackintosh, J. X. Zhu, D. J. Pine, D. A. Weitz, Polarization Memory of Multiply Scattered-Light - Reply. *Phys Rev B* **45**, 8165-8165 (1992).

[253] N. Ghosh, P. K. Gupta, H. S. Patel, B. Jain, B. N. Singh, Depolarization of light in tissue phantoms – effect of collection geometry. *Optics Communications* **222**, 93-100 (2003).

[254] M. K. Swami, H. S. Patel, P. Geethu, A. Uppal, P. K. Kushwaha, P. K. Gupta, Effect of gold nanoparticles on depolarization characteristics of Intralipid tissue phantom. *Opt. Lett.* **38**, 2855-2857 (2013).

[255] M. S. Wróbel, A. P. Popov, A. V. Bykov, M. Kinnunen, M. Jędrzejewska-Szczerska, V. V. Tuchin. (SPIE, 2015), vol. 20, pp. 10.

[256] M. S. Wróbel, A. P. Popov, A. V. Bykov, M. Kinnunen, M. Jędrzejewska-Szczerska, V. V. Tuchin, Multi-layered tissue head phantoms for noninvasive optical diagnostics. *Journal of Innovative Optical Health Sciences* **08**, 1541005 (2015).

[257] J. C. Petermann, University of Akron, (2012).

[258] S. Manhas, M. K. Swami, P. Buddhiwant, N. Ghosh, P. K. Gupta, K. Singh, Mueller matrix approach for determination of optical rotation in chiral turbid media in backscattering geometry. *Opt. Express* **14**, 190-202 (2006).

[259] Y. Guo, N. Zeng, H. He, T. Yun, E. Du, R. Liao, Y. He, H. Ma, A study on forward scattering Mueller matrix decomposition in anisotropic medium. *Opt Express* **21**, 18361-18370 (2013).

[260] H. He, N. Zeng, W. Li, T. Yun, R. Liao, Y. He, H. Ma, Two-dimensional backscattering Mueller matrix of sphere-cylinder scattering medium. *Opt Lett* **35**, 2323-2325 (2010).

[261] B. Laude-Boulesteix, A. De Martino, B. Drevillon, L. Schwartz, Mueller polarimetric imaging system with liquid crystals. *Appl Opt* **43**, 2824-2832 (2004).

[262] E. Garcia-Caurel, A. De Martino, J. P. Gaston, L. Yan, Application of spectroscopic ellipsometry and Mueller ellipsometry to optical characterization. *Appl Spectrosc* **67**, 1-21 (2013).

[263] A. A. Hamza, T. Z. N. Sokkar, K. A. El-Farahaty, H. M. El-Dessouky, Determination of the intrinsic birefringence of polymeric fibres. *Polymer Testing* **23**, 203-208 (2004).

[264] G. P. W., S. G. H. L., R. D., Electrospun fiber mats: Transport properties. *AIChE Journal* **45**, 190-195 (1999).

[265] Y. Wang, Y. Guo, N. Zeng, D. Chen, H. He, H. Ma, Study on the validity of 3 x 3 Mueller matrix decomposition. *J Biomed Opt* **20**, 065003 (2015).

[266] X. Liu, K. Beaudette, X. Wang, L. Liu, B. E. Bouma, M. Villiger, Tissue-like phantoms for quantitative birefringence imaging. *Biomedical Optics Express* **8**, 4454-4465 (2017).

[267] Marika A. Wallenburg, Michael F. G. Wood, Nirmalya Ghosh, a. I. A. Vitkin, Polarimetry-based method to extract geometry-independent metrics of tissue anisotropy. *Optics Letters*, (2010).

[268] B. Heise, K. Wiesauer, E. Gotzinger, M. Pircher, C. K. Hitzenberger, R. Engelke, G. Ahrens, G. Grutzner, D. Stifter, Spatially Resolved Stress Measurements in Materials With Polarisation-Sensitive Optical Coherence Tomography: Image Acquisition and Processing Aspects. *Strain* **46**, 61-68 (2010).

[269] R. Ossikovski, Analysis of depolarizing Mueller matrices through a symmetric decomposition. *J. Opt. Soc. Am. A* **26**, 1109-1118 (2009).

[270] D. Stifter, E. Leiss-Holzinger, B. Heise, J.-L. Bouchot, Z. Major, M. Pircher, E. Götzinger, B. Baumann, C. K. Hitzenberger, in *SPIE BiOS*. (SPIE, 2011), vol. 7889, pp. 8.

[271] M. K. Swami, H. S. Patel, A. Uppal, P. K. Kushwaha, P. K. Gupta, Spectral Mueller matrix measurements for characterization of depolarization from non-spherical gold nanoparticles. *Optics Communications* **308**, 136-141 (2013).

[272] P.-C. Chen, Y.-L. Lo, T.-C. Yu, J.-F. Lin, T.-T. Yang, Measurement of linear birefringence and diattenuation properties of optical samples using polarimeter and Stokes parameters. *Opt. Express* **17**, 15860-15884 (2009).

[273] L. Yu Lung, C. Po-chun, Y. Tsung-chih, L. Jing Fung, Y. Tsung-tse, Using polarimeter and Stokes parameters for measuring linear birefringence and diattenuation properties of optical samples. *EPJ Web of Conferences* **6**, 32001 (2010).

[274] D. B. Chenault, R. A. Chipman, Measurements of linear diattenuation and linear retardance spectra with a rotating sample spectropolarimeter. *Appl. Opt.* **32**, 3513-3519 (1993).

[275] K. C. Hadley, I. A. Vitkin, Optical rotation and linear and circular depolarization rates in diffusively scattered light from chiral, racemic, and achiral turbid media. *J Biomed Opt* **7**, 291-299 (2002).

[276] N. Ortega-Quijano, F. Fanjul-Vélez, I. Salas-García, J. L. Arce-Diego, in *SPIE BiOS*. (SPIE, 2011), vol. 7906, pp. 6.

[277] B. H. Malik, C. W. Pirnstill, G. L. Cote, Dual-wavelength polarimetric glucose sensing in the presence of birefringence and motion artifact using anterior chamber of the eye phantoms. *J Biomed Opt* **18**, 17007 (2013).

[278] R. Rawer, W. Stork, C. F. Kreiner, Non-invasive polarimetric measurement of glucose concentration in the anterior chamber of the eye. *Graefes Arch Clin Exp Ophthalmol* **242**, 1017-1023 (2004).

[279] T. L. Chen, Y. L. Lo, C. C. Liao, Q. H. Phan, Noninvasive measurement of glucose concentration on human fingertip by optical coherence tomography. *BIOMEDO* **23**, (2018).

[280] Q. H. Phan, Y. L. Lo, Stokes-Mueller matrix polarimetry system for glucose sensing. *Opt Laser Eng* **92**, 120-128 (2017).

[281] R. R. Ansari, S. Bockle, L. Rovati, New optical scheme for a polarimetric-based glucose sensor. *J Biomed Opt* **9**, 103-115 (2004).

[282] Z. F. Yu, C. W. Pirnstill, G. L. Cote, Dual-modulation, dual-wavelength, optical polarimetry system for glucose monitoring. *J Biomed Opt* **21**, 87001 (2016).

[283] J. Vanhellemont, H. E. Maes, M. Schaekers, A. Armigliato, H. Cerva, A. Cullis, J. de Sande, H. Dinges, J. Hallais, V. Nayar, C. Pickering, J. L. Stehlé, J. Van Landuyt, C. Walker, H. Werner, P. Salieri, Round robin investigation of silicon oxide on silicon reference materials for ellipsometry. *Applied Surface Science* **63**, 45-51 (1993).

APPENDICES

Organization

Matlab codes are added as they were used in each chapter. If no significant changes were made to a code that was reused in a later chapter then the code is not relisted.

Chapter 2 Matlab code - Use of combined polarization-sensitive optical coherence tomography and Mueller matrix imaging for the polarimetric characterization of excised biological tissue

Mueller matrix polarimeter imaging

```
%camera
hardware_camera='PVCAM';
hardware_camera_name='Camera-1';
import mmcorej.*;
mmc = CMMCore;
mmc.loadSystemConfiguration       ('C:\Program       Files\Micro-Manager-
1.4\MMConfig_demo.cfg');
mmc.setExposure(200);
width = mmc.getImageWidth();
height = mmc.getImageHeight();
pixelType = 'double';

%r2 is liquidcrystal
r2 = serial('COM4');
r2.BaudRate = 38400;
r2.Parity   = 'none';
r2.DataBits = 8;
r2.StopBits = 1;
r2.Terminator ='CR';
fopen(r2)

%Main Program
clear ImgData;
for j = 1:4;
fprintf(r2, sprintf('ver:?'));
fscanf(r2);
fprintf(r2, sprintf('ld:2,?'));
fscanf(r2);
fprintf(r2, sprintf('ld:4,?'));
fscanf(r2);

fprintf(r2, sprintf('ld:2,%d',round(0*6553.6)));
fscanf(r2);
fprintf(r2, sprintf('ld:4,%d',round(0*6553.6)));
fscanf(r2);

% InputVol1 = [4.7987 4.7987 4.7987 0.9987];
% InputVol2 = [4.7987 2.0159 1.0059 2.0027];

InputVol1 = [9.7987 2.5987 9.7987 0.9987];
InputVol2 = [9.7987 2.0159 1.0059 2.2027];
```

```
        InputL1      = round(InputVol1(j)*6553.6);
        InputL2      = round(InputVol2(j)*6553.6);

        fprintf(r2, sprintf('ld:2,%d',InputL1));
        fscanf(r2);
        pause(0.5);
        fprintf(r2, sprintf('ld:4,%d',InputL2));
        fscanf(r2);
        pause(0.5);

fprintf(r2, sprintf('ver:?'));
fscanf(r2);
fprintf(r2, sprintf('ld:1,?'));
fscanf(r2);
fprintf(r2, sprintf('ld:3,?'));
fscanf(r2);

fprintf(r2, sprintf('ld:1,%d',round(0*6553.6)));
fscanf(r2);
fprintf(r2, sprintf('ld:3,%d',round(0*6553.6)));
fscanf(r2)
    cnt=0;
 Vol1=  [4.7987     4.7987      2.4758   2.4758    4.7987   4.7987];
 Vol2=  [2.6827     1.5908      2.6827   1.5908    5.0792   2.0159];

            cnt    = cnt+1;
for i=1:length(Vol1);
    pause (0.5);

        %Polarimeter LCR

        L1      = round(Vol1(i)*6553.6);
        L2      = round(Vol2(i)*6553.6);

        fprintf(r2, sprintf('ld:1,%d',L1));
        fscanf(r2);
        pause(0.5);
        fprintf(r2, sprintf('ld:3,%d',L2));
        fscanf(r2);
        pause(0.5);

%          'take a measurement'
        mmc.snapImage();
b = mmc.getImage();  % returned as a 1D array of signed integers in row-
major order
b = typecast(double(b), pixelType);      % pixels must be interpreted as
unsigned integers
b = reshape(b, [width, height]); % image should be interpreted as a 2D
array
%b = transpose(b);
        ImgData(i,:,:) = b(:,:,1);
```

```
end
    % Save the image file
    save(sprintf('OPP_imageS%d',j),'ImgData')
end
run StokeResults.m

%Preview
mmc.snapImage();
b = mmc.getImage();  % returned as a 1D array of signed integers in row-
major order
b = typecast(double(b), pixelType);      % pixels must be interpreted as
unsigned integers
b = reshape(b, [width, height]); % image should be interpreted as a 2D
array
% b = transpose(b);
imagesc(b);colorbar
%Save
save Preview b;imagesc((b));colormap(gray);axis('square')
```

Chapter 3 Matlab code - Use of Mueller matrix Polarimetry and Optical Coherence Tomography in the characterization of cervical collagen anisotropy

Mueller matrix polarimeter imaging

```
if 0
%camera
LucamConnect(1)
LucamSetGamma(1, 1)
LucamSetFrameRate(1,1);
LucamSetGain(1,1)
LucamSet16BitCapture(true,1);
LucamSetExposure(50,1);
LucamShowPreview(1);
pause(2)

%r2 is liquidcrystal
r2 = serial('COM8');
r2.BaudRate = 38400;
r2.Parity   = 'none';
r2.DataBits = 8;
r2.StopBits = 1;
r2.Terminator ='CR';
fopen(r2)
end

%Main Program
clear ImgData;
for j = 1:4;
    j
fprintf(r2, sprintf('ver:?'));
fscanf(r2);
fprintf(r2, sprintf('ld:3,?'));
fscanf(r2);
```

```
fprintf(r2, sprintf('ld:4,?'));
fscanf(r2);

fprintf(r2, sprintf('ld:3,%d',round(0*6553.6)));
fscanf(r2);
fprintf(r2, sprintf('ld:4,%d',round(0*6553.6)));
fscanf(r2);

%%%%JJ2
% InputVol1 = [4.6527 2.0206 2.7313 2.6313];
% InputVol2 = [5.0954 5.0954 2.6763 5.0954];

%%%%JJ2 Tweak
InputVol1 = [5.2527 2.2206 2.9313 2.8313];
InputVol2 = [5.0954 5.0954 2.8763 5.2954];

%%%%750nm2
% InputVol1 = [7.6527 4.6527 2.6313 4.0527];
% InputVol2 = [7.0954 3.6954 1.6954 5.0954];

%%%%735nm2
% InputVol1 = [5.6527 1.8527 2.6313 2.2527];
% InputVol2 = [5.0954 2.6954 1.8954 5.0954];

        InputL1      = round(InputVol1(j)*6553.6);
        InputL2      = round(InputVol2(j)*6553.6);

        fprintf(r2, sprintf('ld:3,%d',InputL1));
        fscanf(r2);
        pause(2);
        fprintf(r2, sprintf('ld:4,%d',InputL2));
        fscanf(r2);
        pause(2);

fprintf(r2, sprintf('ver:?'));
fscanf(r2);
fprintf(r2, sprintf('ld:1,?'));
fscanf(r2);
fprintf(r2, sprintf('ld:2,?'));
fscanf(r2);

fprintf(r2, sprintf('ld:1,%d',round(0*6553.6)));
fscanf(r2);
fprintf(r2, sprintf('ld:2,%d',round(0*6553.6)));
fscanf(r2)
    cnt=0;

%Boulbry Voltages
Vol1=  [5.079     5.079     2.871     2.871     5.079     5.079]; % this is LC1 (boulbry) at 0
Vol2=  [5.079     2.095     1.719     2.731     2.731     1.719]; % This is LC2 at -45
```

```
            cnt    = cnt+1;
for i=1:length(Vol1);
    pause (0.5);

        %Polarimeter LCR`

        L1      = round(Vol1(i)*6553.6);
        L2      = round(Vol2(i)*6553.6);

        fprintf(r2, sprintf('ld:1,%d',L1));
%         fscanf(r2);
        pause(1);
        fprintf(r2, sprintf('ld:2,%d',L2));
%         fscanf(r2);
        pause(1);

          a = double(LucamCaptureFrame(1));b=a(:,:,1);

        ImgData(i,:,:) = b(:,:,1);

end
    % Save the image file
    save(sprintf('OPP_imageS%d',j),'ImgData')
end
% run StokeResults.m

if 0
%Preview
a = double(LucamCaptureFrame(1));b=a(:,:,1);imagesc(b);colorbar;hold on;
%Save
save Preview b;imagesc((b));colormap(gray);axis('square')
end
```

Mueller matrix Image Post-processing

```
clear all;close all
load orient;load MR;load Mdepol;load Preview;load energy
% Mdepol(Mdepol<0.7)=0;
energy=1-(energy./5000);%max(max(energy)));
A(:,:) = energy;

dx=50;
MR=abs(MR-(pi/2));

bb = medfilt2((bb),[3 3])*pi/180;
for y = dx:dx:size(bb,1)-dx
for x = dx:dx:size(bb,2)-dx
    a=bb(y:y+dx,x:x+dx);
     if mean2(Mdepol(y:y+dx,x:x+dx))<=0.5; %mask lines less than given
depolarization
       min(min(Mdepol(y:y+dx,x:x+dx)));
       angle(y -((y/dx)*(dx-1)),x - ((x/dx)*(dx-1))) = NaN; %Creating
angle index between 1:50 rather than 10:10:500
%     elseif mean2(MR(y:y+dx,x:x+dx))*180/pi>45;
%        min(min(Mdepol(y:y+dx,x:x+dx)));
```

```
%        angle(y -((y/dx)*(dx-1)),x - ((x/dx)*(dx-1))) =  NaN;
    else
    [mu kappa] = circ_vmpar(a(:));
    angle(y -((y/dx)*(dx-1)),x - ((x/dx)*(dx-1))) =  (mu*180/pi);
    MMA(y:y+dx,x:x+dx)=(mu*180/pi);
end
end
end
[x,y]=meshgrid(dx:dx:size(bb,2)-dx,dx:dx:size(bb,1)-dx);

u=cosd(angle+0);
v=sind(angle+0);
figure(1);clf;
% load cut;load cutouter;bb = bb.*(cut-1).*-cutouter;MR = abs(MR.*(cut-
1).*-cutouter);Mdepol = abs(Mdepol.*(cut-1).*-cutouter);
load cutouter;load
cut;cutouter=double(cutouter);cutouter(cutouter==0)=NaN;cut=double(abs(
1-cut));cut(cut==0)=NaN;
h1=imagesc(medfilt2(-bb.*180/pi,[4
4])+0);colormap(hsv);axis('square');caxis([-180
180]);cmap=colormap;colormap(cmap);
mm=cmap;jet_wrap =
vertcat(flip(mm),flip(mm));colormap(jet_wrap);phasebarJRR('location','s
w','size',.1);
set(gca,'xtick',[]);set(gca,'ytick',[]);set(gcf,'color','white');%cb=co
lorbar;set(cb,'FontSize',15);ylabel(cb,'Orientation [°]');
hold on;set(h1,'alphadata',A.*cutouter.*cut);set(gca,'color','black');
hold on;p =
quiver(x,y,u,v,'k','ShowArrowHead','off');set(p,'color','black','Linewi
dth',1.5,'AutoScaleFactor',0.3);

% figure(2);clf
% imagesc(MMA,[-180 180]);cb=colorbar;colormap(hsv);axis('square');
%
set(gca,'xtick',[]);set(gca,'ytick',[]);set(gcf,'color','white');set(cb
,'FontSize',15);ylabel(cb,'Orientation [°]');
% hold on;p =
quiver(x,y,u,v,'k','ShowArrowHead','off');set(p,'color','black','Linewi
dth',2);

% figure(3);clf
% imagesc((b),[0
10000]);colormap(gray);axis('square');%cmap=colormap;cmap(32,:) =
0;colormap(cmap);
% % hold on;p =
quiver(x,y,u,v,'k','ShowArrowHead','off');colorbar;set(p,'color','black
','Linewidth',2);
% % set(gca,'xtick',[]);set(gca,'ytick',[]);set(gcf,'color','white');
%
% figure(4);%set(gca,'position',[0 0 1 1],'units','normalized');
%  imagesc(medfilt2(Mdepol,[8 8]));cp=colormap(jet);cp(1,:) = [0 0
0];colormap(cp);axis('square');
% cb=colorbar;caxis([0
1]);set(cb,'FontSize',15);set(gca,'xtick',[]);set(gca,'ytick',[]);ylabe
l(cb,'Depolarization')
```

```
%                %                hold                on;p                =
quiver(x,y,u,v,'k','ShowArrowHead','off');set(p,'color','black','Linewi
dth',2);
%
% figure(5)%;set(gca,'position',[0 0 1 1],'units','normalized')
%                                imagesc(((medfilt2(real(MR*180/pi)+0,[8
8])))));colormap('jet');axis('square');
%                                                  cb=colorbar;caxis([0
90]);set(cb,'FontSize',15);set(gca,'xtick',[]);set(gca,'ytick',[]);ylab
el(cb,'Retardance [°]');
% cmap=colormap;cmap(1,:) = 0;colormap(cmap);
%                %                hold                on;p                =
quiver(x,y,u,v,'k','ShowArrowHead','off');set(p,'color','black','Linewi
dth',2);
```

Mueller matrix Decomposed orientation histogram plotting

```
close all;clear;clc;load orient;%load Preview;%load cut;bb = bb.*cut;

bb = medfilt2((bb),[3 3]);
figure(2);imagesc((bb));colormap(jet);axis('square');[a      rect]      =
imcrop();[m n] = size(a);
%%%% rect = [xstart ystart width height] %%%%

figure(3);h                                                             =
rose((a(:)+90)*(pi/180),90);axis('square');set(gca,'FontSize',15);view(
0,90);
set(h,'linewidth',3,'color','k');th                                     =
findall(gcf,'Type','text');xlabel('Angle
(°)');set(gca,'xaxislocation','top');
for i = 1:length(th),
    set(th(i),'FontSize',20)
end
ab=(a+0)*pi/180;
[mu kappa]=circ_vmpar([ab]);
[b b0] = circ_skewness(ab(:));
[k k0] = circ_kurtosis(ab(:));
% b
k
mu*180/pi+90

% bb = medfilt2((bb),[3 3]);
%  figure(2);imagesc((bb));colormap(jet);axis('square');a  =  imcrop();[m
n] = size(a);
% aa = reshape(a,m*n,1);
%
%                              figure(3);h                              =
rose((aa+90)*(pi/180),50);axis('square');set(gca,'FontSize',15);view(90
,-90);
%                set(h,'linewidth',3,'color','k');th                    =
findall(gcf,'Type','text');ylabel('Angle
(°)');set(gca,'yaxislocation','right');
% for i = 1:length(th),
%     set(th(i),'FontSize',20)
% end
% ab=(a+0)*pi/180;
```

```
% [mu kappa]=circ_vmpar([ab]);
% [b b0] = circ_skewness(ab(:));
% [k k0] = circ_kurtosis(ab(:));
% b
% k
% mu*180/pi
```

Optical coherence tomography imaging

```
if 1
    % 2.2 Generate waveforms for Galvo
    %slow x scan waveforma
    pixelx=250;   % determine the steps of xscanning;1
    pixely=250;   % determine the steps of yscanning;
    xrange=1.0;     % determine the range of xscanning;
    yrange=1.0;     % determine the range of yscanning;
    xx                    =                    xrange*2*repmat([1:pixelx
fliplr(1:pixelx)],[1,pixely/2])/pixelx-xrange;
    iter = 1; % # of iterations for averaging

    % generate triangle wave for x scanning: min(xx)=-0.98 v, max(xx)=1
v if xrange=yrange=1, and pixelx=100=pixely
    % xrange determines the angle of the whole scanning.
    %slow y scan waveform
    a = (-(pixely-1):2:(pixely-1))*yrange/(pixely-1);  %-1 : 1/99 : 1
    b = repmat(a,pixelx,1);
    yy = reshape(b,[1,(pixely)*(pixelx)]);

    %rotated waveforms if you designed different scanning, or set theta
to be 0.
    theta=0;
    rotatedx=(xx*cos(theta)-yy*sin(theta))';%+xoffset;
    rotatedy=(xx*sin(theta)+yy*cos(theta))';%+yoffset;

    dataa=[rotatedx rotatedy];
%     plot(rotatedx,'ro')
    %pause
    % 2.4 %Initialization of NI Cards and closing shutters
    %set NI cards
    daq.getDevices
    %load data for single scan with default scan parameters;and start the
ao,
    %set the Glov in the zero position;
    s = daq.createSession('ni');
    d = daq.createSession('ni');
    s.Rate = 10000;
    addAnalogOutputChannel(s,'Dev2','ao2','Voltage');
    addAnalogOutputChannel(d,'Dev2','ao3','Voltage');

    %s.startForeground();
    % s.TerminalConfig = 'SingleEnded'
    % Construct a video input object associated
    %   imaqhwinfo
    % Acquire and display a single image frame:
```

```
    obj = imaq.VideoDevice('ni', 1);
    frame = step(obj);
    % TriggerConfiguration: 'external0/fallingEdge
end

tic
FFsum(pixelx,1:4096,pixely)=0;
for k = 1:iter
    k
    for z=1:pixely
        d.outputSingleScan(a(1,z));
        for i=1:pixelx
            frame=0;
            s.outputSingleScan(dataa(i,1));
            frame=step(obj);
            FFsum(i,:,z) = FFsum(i,:,z)+frame(1,:);
%FF(x,pixels,y,iterations)
        end
    end
end
toc
clearvars -except FFsum iter pixelx pixely
% FFavg = FFsum./iter;
save Cervix4 FFsum pixelx pixely iter
```

Optical coherence tomography interpolation

```
% clear all;
close all;
% clearvars -except FFsum pixelx pixely
% load DC
% load Xi
load Xi2048
C0=792.2709;
C1=.09642887484;
C2=1.5926911e-6;
C3= -1.72575e-10;
lambda= (1:2048); %Pixels
X=1000./(C0+C1*(lambda-1)+C2*(lambda-1).^2);

for z=1:pixely
    for i=1:pixelx
        interpA(i,:,z)=interp1(X,(FFsum(i,:,z)),Xi(1,:)); %interpolation
after DC subtract; -DC(i,:) -(FF(i,:,z))
        FFTY(i,:,z)=abs(fftshift(fft(interpA(i,:,z), 2^12)));
    end
end
clearvars -except FFTY FFsum iter pixelx pixely
 figure(1);
 imagesc(sqrt((FFTY(:,1:2048,125))'),[0 5]);colormap(gray)
for i=1400:2000
%
figure(2);imagesc(rot90(sqrt((squeeze(FFTY(:,i,:)+FFTY(:,i+1,:)+FFTY(:,
i+2,:)+FFTY(:,i+3,:)))),3));colormap(gray)
    figure(1);imagesc(log(squeeze(FFsum(:,i,:)))');colormap(gray)
   title(i)
```

```
    pause
end

k = 1400:2000;
for i=1:250
%
figure(2);imagesc(rot90(sqrt((squeeze(FFTY(:,k,i)+FFTY(:,k,i+1)+FFTY(:,
k,i+2)+FFTY(:,k,i+3)))),3));colormap(gray)
    figure(1);imagesc(sqrt(squeeze(FFTY(:,k,i)))');colormap(gray)
   title(i)
    pause
end

img = 0;
for k = 1706:1712
    img = img + FFTY(:,k,:);
end
imagesc(rot90(sqrt((squeeze(img))),3));colormap(gray);%caxis([0 10]);

save ParaffinCervix1-2-1890 img
```

Chapter 4 Matlab code - Use of Mueller matrix colposcopy in the characterization of cervical collagen anisotropy

Mueller matrix decomposed orientation kurtosis image calculation

```
clear all;close all;clc
load orient;load MR;load Preview;load Mdepol;
%load energy;energy=1-(energy./15000);

% for i=1:size(bb,1)
%     for j=1:size(bb,2)
%         if bb(i,j)<0
%             bb(i,j)=bb(i,j)+180;
%         else
%             bb(i,j)=bb(i,j);
%         end
%     end
% end

dx=5;
MR=abs(MR-(pi/2));
load cutouter;load cut;
cutouter=double(cutouter);cutouter(cutouter==0)=NaN;
cut=double(abs(1-cut));cut(cut==0)=NaN;
% A(:,:) = energy.*cutouter.*cut;
% A(:,:) = energy;

bb = medfilt2((bb).*cutouter.*cut,[3 3])*pi/180; %Median filter
% bb = medfilt2((bb),[5 5])*pi/180; %Median filter

for y = dx:dx:size(bb,1)-dx
for x = dx:dx:size(bb,2)-dx
    a=bb(y:y+dx,x:x+dx);
```

```
     if  mean2(Mdepol(y:y+dx,x:x+dx))<=0.1;  %mask  lines  less  than  give
depolarization
       kurt(y  -((y/dx)*(dx-1)),x  -  ((x/dx)*(dx-1)))  =   NaN;  %Creating
angle index between 1:50 rather than 10:10:500
%     elseif mean2(MR(y:y+dx,x:x+dx))*180/pi>45;
%        min(min(Mdepol(y:y+dx,x:x+dx)));
%        angle(y -((y/dx)*(dx-1)),x - ((x/dx)*(dx-1))) =  NaN;
    else
    [k k0] = circ_kurtosis(a(:));
    kurt(y -((y/dx)*(dx-1)),x - ((x/dx)*(dx-1))) = abs(k);
%%%%%standard deviation
%     k = std2(a(:));
%     kurt(y -((y/dx)*(dx-1)),x - ((x/dx)*(dx-1))) =  k;
end
end
end

[x,y]=meshgrid(dx:dx:size(kurt,2)-dx,dx:dx:size(kurt,1)-dx);

%
set(gca,'xtick',[]);set(gca,'ytick',[]);set(gcf,'color','white');set(cb
,'FontSize',15);ylabel(cb,'Orientation [°]');
%                    hold                    on;p                       =
quiver(x,y,u,v,'k','ShowArrowHead','off');set(p,'color','black','Linewi
dth',2);
figure(1);clf;
h1=imagesc(medfilt2(kurt,[3   3]));colormap(jet);axis('square');caxis([0
1]);cmap=colormap;cmap(1,:) = 0;colormap(cmap);
set(gca,'xtick',[]);set(gca,'ytick',[]);set(gcf,'color','white');cb=col
orbar;set(cb,'FontSize',15);ylabel(cb,'Kurtosis');

sum(kurt(:)>.6)/sum(sum(sum(abs(isnan(kurt)-1))))
nanmean(nanstd(kurt))
```

Image rotation and subsection generation around cervix os for statistical comparison

```
clear all;close all;clc
load orient;load MR;load Preview;load Mdepol;%load energy
% energy=1-(energy./15000);
current=pwd;
mkdir FramesBW;mkdir FramesColor;mkdir FramesKurtosis;
% mkdir FramesBW2;mkdir FramesColor2;mkdir FramesKurtosis2;

dx=50;
MR=abs(MR-(pi/2));
load cutouter;load cut;s=regionprops(cut);
cutouter=double(cutouter);cutouter(cutouter==0)=NaN;
cut=double(abs(1-cut));cut(cut==0)=NaN;
% A(:,:) = energy.*cutouter.*cut;
% A(:,:) = energy.*cutouter;
dy=dx;
% c=zeros(size(bb));
```

```
% c(:,round(s.Centroid(1))-dy/2:round(s.Centroid(1))+dy/2)=1;
% c(round(s.Centroid(2))-dy/2:round(s.Centroid(2))+dy/2,:)=1;
% A=A.*c;A(A==0)=NaN;
% A(:,:) = energy;

% load cut2;cut2=double(abs(1-cut2));cut2(cut2==0)=NaN;
bb = medfilt2((bb).*cutouter.*cut,[3 3])*pi/180; %Median filter
% bb = medfilt2((bb.*cut),[3 3])*pi/180;%Median filter
% load cutouter2;b =  b.*cutouter;

%%%% Bins for radii of concentric circule region %%%%
% cx = round(s.Centroid(1)/dy); %center bin in x direction
% cy = round(s.Centroid(2)/dy); %center bin in y direction

pad = 500; % # of pixels for padding
padbb = padarray(bb,[pad pad],'both');%imagesc(padbb);axis('square')
padb       =       padarray(b,[pad       pad],'both');%imagesc(padb,[0
10000]);axis('square')
padMdepol             =             padarray(Mdepol.*cutouter.*cut,[500
500],'both');%imagesc(padMdepol,[0 1]);axis('square')
padMR = padarray(MR.*cutouter.*cut,[500 500],'both');

c=zeros(size(padbb));
c(:,round(s.Centroid(1)+pad)-dy/2:round(s.Centroid(1)+500)+dy/2)=1;
c(round(s.Centroid(2)+pad)-dy/2:round(s.Centroid(2)+500)+dy/2,:)=1;

cx = round(s.Centroid(1)+pad); %center bin in x direction
cy = round(s.Centroid(2)+pad); %center bin in y direction

f=0;
% f=19;
for jj = 0:10:350
    f=f+1;
    bbrot                                                                    =
rotateAround(padbb,round(s.Centroid(2)+pad),round(s.Centroid(1)+pad),jj
,'bicubic');bbrot(bbrot==0)=NaN;
    brot                                                                     =
rotateAround(padb,round(s.Centroid(2)+pad),round(s.Centroid(1)+pad),jj,
'bicubic');brot(brot==0)=NaN;
%                                                       Arot           =
rotateAround(A,round(s.Centroid(2)),round(s.Centroid(1)),jj,'bicubic');
    Mdepolrot                                                                =
rotateAround(padMdepol,round(s.Centroid(2)+pad),round(s.Centroid(1)+pad
),jj,'bicubic');
    MRrot                                                                    =
rotateAround(padMR,round(s.Centroid(2)+pad),round(s.Centroid(1)+pad),jj
,'bicubic');
i = [1:dy:size(bbrot,2)-dy];
j = [1:dy:size(bbrot,1)-dy];

clear KK;
z=0;
for yy=j
    z=z+1;
```

```
    a=bbrot(yy:yy+dy,round(s.Centroid(1))-
dy/2+pad+1:round(s.Centroid(1))+dy/2+pad-1);
    [k k0]=circ_kurtosis(a(:));[mu kappa] = circ_vmpar(a(:));
    KK(z,1)= k;clear a;muu(z,1) = mu*180/pi;
end
z=0;
for xx=i
    z=z+1;
    a=bbrot(round(s.Centroid(2))-
dy/2+pad+1:round(s.Centroid(2))+dy/2+pad-1,xx:xx+dy);
    [k k0]=circ_kurtosis(a(:));[mu kappa] = circ_vmpar(a(:));
    KK(z,2)= k;clear a;muu(z,2) = mu*180/pi;
end

kurtyx(:,:,f) = KK;
muyx(:,:,f) = muu;

for y = dx:dx:size(bbrot,1)-dx
    for x = dx:dx:size(bbrot,2)-dx
        a=bbrot(y:y+dx,x:x+dx);
        if  mean2(Mdepolrot(y:y+dx,x:x+dx))<=0.5;  %mask  lines  less  than
give depolarization
            angle(y  -((y/dx)*(dx-1)),x  -  ((x/dx)*(dx-1)))  =   NaN;
%Creating angle index between 1:50 rather than 10:10:500
                elseif mean2(MRrot(y:y+dx,x:x+dx))*180/pi>60;
                   angle(y -((y/dx)*(dx-1)),x - ((x/dx)*(dx-1))) =  NaN;
        else
            [mu kappa] = circ_vmpar(a(:));
            angle(y -((y/dx)*(dx-1)),x - ((x/dx)*(dx-1))) =  (mu*180/pi);
        end
    end
end

[x,y]=meshgrid(dx:dx:size(bbrot,2)-dx,dx:dx:size(bbrot,1)-dx);

dk=5;
for y2 = dk:dk:size(bbrot,1)-dk
    for x2 = dk:dk:size(bbrot,2)-dk
        a=bbrot(y2:y2+dk,x2:x2+dk);
%          if mean2(Mdepolrot(y2:y2+dk,x2:x2+dk))<=0.5; %mask lines less
than give depolarization
% kurt(y2 -((y2/dk)*(dk-1)),x2 - ((x2/dk)*(dk-1))) =  NaN;
%         else
            [k k0] = circ_kurtosis(a(:));
            kurt(y2 -((y2/dk)*(dk-1)),x2 - ((x2/dk)*(dk-1))) =  k;
        end
    end
% end

[x2,y2]=meshgrid(dk:dk:size(kurt,2)-dk,dk:dk:size(kurt,1)-dk);

u=cosd(-angle+0);
v=sind(-angle+0);
% imagesc(u);axis('square');cutquiver=roipoly();save cutquiver cutquiver
```

```
% load cutquiver;cutquiver=abs(1-
cutquiver);u=u.*cutquiver;v=v.*cutquiver;
figure(1);clf;
h1=imagesc(medfilt2(-bbrot.*180/pi+0,[3
3]));colormap(hsv);axis('square');caxis([-180
180]);cmap=colormap;colormap(cmap);
mm=cmap;jet_wrap =
vertcat(flip(mm),flip(mm));colormap(jet_wrap);phasebarJRR('location','s
e','size',.2);
cmap=colormap;cmap(1,:) = 0;colormap(cmap);
set(gca,'xtick',[]);set(gca,'ytick',[]);set(gcf,'color','white');%cb=co
lorbar;set(cb,'FontSize',15);ylabel(cb,'Orientation [°]');
% hold on;viscircles([round(s.Centroid(1)) round(s.Centroid(2))],300);
% viscircles([round(s.Centroid(1)) round(s.Centroid(2))],700)
% hold on;set(h1,'alphadata',A); set(gca,'color','black')
% hold on;p =
quiver(x(1:1:end),y(1:1:end),u(1:1:end),v(1:1:end),'k','ShowArrowHead',
'off','AutoScaleFactor',0.5);set(p,'color','black','Linewidth',1.5);
z=0;
for yy=j
    z=z+1;
    if isnan(KK(z,1))
        hold on;rectangle('Position',[round(s.Centroid(1)+pad)-
dy/2,yy,dy,dy],'LineWidth',2,'LineStyle','-','EdgeColor','r');
    elseif KK(z,1)<.6
        hold on;rectangle('Position',[round(s.Centroid(1)+pad)-
dy/2,yy,dy,dy],'LineWidth',2,'LineStyle','-','EdgeColor','r');
    else
        hold on;rectangle('Position',[round(s.Centroid(1)+pad)-
dy/2,yy,dy,dy],'LineWidth',2,'LineStyle','-','EdgeColor','b');
    end
end
z=0;
for xx=i
    z=z+1;
    if isnan(KK(z,2))
        hold on;rectangle('Position',[xx,round(s.Centroid(2)+pad)-
dy/2,dy,dy],'LineWidth',2,'LineStyle','-','EdgeColor','r');
    elseif KK(z,2)<.6
        hold on;rectangle('Position',[xx,round(s.Centroid(2)+pad)-
dy/2,dy,dy],'LineWidth',2,'LineStyle','-','EdgeColor','r');
    else
        hold on;rectangle('Position',[xx,round(s.Centroid(2)+pad)-
dy/2,dy,dy],'LineWidth',2,'LineStyle','-','EdgeColor','b');
    end
end
figure(2);clf
h2=imagesc((brot),[0
10000]);colormap(gray);axis('square');%cmap=colormap;cmap(32,:) =
0;colormap(cmap);
set(gca,'xtick',[]);set(gca,'ytick',[]);set(gcf,'color','white');
hold on;p =
quiver(x(1:1:end),y(1:1:end),u(1:1:end),v(1:1:end),'ShowArrowHead','off
','AutoScaleFactor',0.5);set(p,'color','white','Linewidth',2);
% hold on;viscircles([round(s.Centroid(1)) round(s.Centroid(2))],300);
```

```
% viscircles([round(s.Centroid(1)) round(s.Centroid(2))],700)
% hold on;set(h2,'alphadata',A); set(gca,'color','black')
z=0;
for yy=j
    z=z+1;
    if isnan(KK(z,1))
        hold          on;rectangle('Position',[round(s.Centroid(1)+pad)-
dy/2,yy,dy,dy],'LineWidth',2,'LineStyle','-','EdgeColor','r');
    elseif KK(z,1)<.6
        hold          on;rectangle('Position',[round(s.Centroid(1)+pad)-
dy/2,yy,dy,dy],'LineWidth',2,'LineStyle','-','EdgeColor','r');
    else
        hold          on;rectangle('Position',[round(s.Centroid(1)+pad)-
dy/2,yy,dy,dy],'LineWidth',2,'LineStyle','-','EdgeColor','b');
    end
end
z=0;
for xx=i
    z=z+1;
    if isnan(KK(z,2))
        hold      on;rectangle('Position',[xx,round(s.Centroid(2)+pad)-
dy/2,dy,dy],'LineWidth',2,'LineStyle','-','EdgeColor','r');
    elseif KK(z,2)<.6
        hold      on;rectangle('Position',[xx,round(s.Centroid(2)+pad)-
dy/2,dy,dy],'LineWidth',2,'LineStyle','-','EdgeColor','r');
    else
        hold      on;rectangle('Position',[xx,round(s.Centroid(2)+pad)-
dy/2,dy,dy],'LineWidth',2,'LineStyle','-','EdgeColor','b');
    end
end

figure(3);clf;
h3=imagesc(medfilt2(kurt,[3   3]));colormap(jet);axis('square');caxis([0
1]);cmap=colormap;cmap(1,:) = 0;colormap(cmap);
set(gca,'xtick',[]);set(gca,'ytick',[]);set(gcf,'color','white');cb=col
orbar;set(cb,'FontSize',15);ylabel(cb,'Kurtosis');
% pause
jj
cd(current);cd FramesColor;saveas(h1,sprintf('color%d.tif',f));
cd(current);cd FramesBW;saveas(h2,sprintf('bw%d.tif',f));
cd(current);cd FramesKurtosis;saveas(h3,sprintf('kurt%d.tif',f));
close all
end
cd(current);
save kurtyx kurtyx
save muyx muyx
```

VITA

	JOSEPH JAMES CHUE-SANG
	Born, Miami, Florida
2013	B.S. Biomedical Engineering Florida International University Miami, Florida
2016	Newport SPIE Student Travel Award
2015-2019	Teaching/Graduate Assistant Florida International University Miami, Florida
2017-2019	Doctoral Candidate Florida International University Miami, Florida

PUBICATIONS

Joseph Chue-Sang, Mariacarla Gonzalez, Angie Pierre, Megan Laughrey, Ilyas Saytashev, Tatiana Novikova, and Jessica C. Ramella-Roman "Optical phantoms for biomedical polarimetry: a review," Journal of Biomedical Optics 24(3), 030901 (8 March 2019). https://doi.org/10.1117/1.JBO.24.3.030901

Joseph Chue-Sang, Nola Holness, Mariacarla Gonzalez, Joan Greaves, Ilyas Saytashev, Susan Stoff, Amir Gandjbakhche, Viktor V. Chernomordik, Gene Burkett, and Jessica C. Ramella-Roman "Use of Mueller matrix colposcopy in the characterization of cervical collagen anisotropy," Journal of Biomedical Optics 23(12), 121605 (7 August 2018). https://doi.org/10.1117/1.JBO.23.12.121605

Joseph Chue-Sang, Yuqiang Bai, Susan Stoff, Mariacarla Gonzalez, Nola A. Holness, Jefferson Gomes, Ranu Jung, Amir H. Gandjbakhche, Viktor V. Chernomordik, and Jessica C. Ramella-Roman "Use of Mueller matrix polarimetry and optical coherence tomography in the characterization of cervical collagen anisotrophy," Journal of Biomedical Optics 22(8), 086010 (29 August 2017). https://doi.org/10.1117/1.JBO.22.8.086010

Joseph Chue-Sang, Yuqiang Bai, Susan Stoff, David Straton, Sharan D. Ramaswamy, and Jessica C. Ramella-Roman "Use of combined polarization-sensitive optical coherence tomography and Mueller matrix imaging for the polarimetric characterization

of excised biological tissue," Journal of Biomedical Optics 21(7), 071109 (1 March 2016). https://doi.org/10.1117/1.JBO.21.7.071109